AN ABSTRACT OF THE THESIS OF

James Joseph Simpson for the degree of Doctor of Philosophy

in Oceanography presented on April 18, 1977

Title: SMALL SCALE TEMPERATURE STRUCTURE OF THE UPPER OCEAN

Abstract approved: Redacted for privacy

Clayton A. Paulson

Small scale temperature structure of the upper ocean is examined in terms of measurement and analysis of the heat balance at the sea surface, the distribution of downward irradiance with depth, the radiometrically determined sea surface temperature, and the temperature and salinity of the upper 300 meters. Results were obtained during OWAX (Ocean Wave Experiment) and POLE, a component of the North Pacific Experiment (NORPAX).

Sea surface albedo was estimated from simultaneous measurements of incident and reflected solar fluxes. Parametric representation of albedo in terms of solar altitude and atmospheric transmittance appears valid for solar altitudes greater than 25 degrees. For overcast conditions the sky radiance distribution becomes nearly isotropic and the albedo assumes the value 0.06. Good agreement exists between values presently reported and those obtained by Payne (1972).

Empirical relations for estimating both short- and long-wave radiative flux components are evaluated. A relation due to Lumb (1964) for determining incident solar flux yields values in good agreement (5%) with observations. Formulas for estimating net long-wave flux yield poor agreement with observations. If such empirical relations consistently overestimate net long-wave flux by factors in excess of 50%, as present results suggest, northward heat transports based on these formulas may be too small. This suggestion is in qualitative agreement with results of Vonder Haar and Oort (1973).

Observations of downward solar radiation as a function of depth

indicate that irradiance decreases much faster than exponential in the upper five meters, falling to one-third the incident value between two and three meters depth. Below 10 meters, the decrease was exponential at a rate characteristic of moderately clear water of Type IA (Jerlov, 1968). The observations are well represented by a sum of two exponentials.

Profiles of salinity and temperature taken during POLE indicate that there was usually a well-mixed layer near the surface, although during light winds, a diurnal thermocline was evident. The structure below the thermocline was often complex with temperature inversions as large as 0.5° C. These inversions were compensated by salinity so that the density profile was stable. The depth of the well-mixed layer was correlated with mechanical energy input by the wind but was also influenced by horizontal advection of water having differing characteristics.

With the above parameterization for absorption of solar flux, vertically integrated equations defining the behavior of the well-mixed layer, under the assumptions of Kraus and Turner (1967) were employed. The mixing energy coefficient, m, was determined by diagnostic methods yielding the value 0.0022.

Observations indicate that sea surface temperature fluctuations are asymetric with spikes of warm temperature, frequently as large as 0.5° C. Destruction of the thermal boundary layer below the interface by capillary waves, breaking waves, gusts of wind, and turbulence in the water column may produce spikes.

A statistically significant coherence, typically 0.4 to 0.5, between waves and sea surface temperature occurs at the same frequency as the peak in the wave spectrum, 0.1 Hz. Phase spectra indicate that warm temperature associated with the destruction of the thermal boundary layer occurs frequently on the upwind side of gravity waves and on the downwind side of steeply-sloping wave crests.

The magnitude of the temperature difference between the cool surface layer at the interface and the warmer bulk temperature is related to simultaneous measurements of heat flux through the interface and surface wind stress via Sander's (1967) method. The mean value of λ was 6 ± 2.

Small Scale Temperature Structure of the Upper Ocean

by

James Joseph Simpson

A THESIS

submitted to

Oregon State University

in partial fulfillment of
the requirements for the
degree of

Doctor of Philosophy

Completed April 18, 1977

Commencement June 1977

APPROVED:

Redacted for privacy

Associate Professor of Oceanography
in charge of major

Redacted for privacy

Acting Dean of School of Oceanography

Redacted for privacy

Dean of Graduate School

Date thesis is presented April 18, 1977

Typed by Opal Grossnicklaus for James Joseph Simpson

ACKNOWLEDGEMENTS

Many people assisted in the completion of this work. Special thanks is due Dr. C. A. Paulson, my thesis advisor, for the broad latitude he allowed me in pursuing my doctoral studies. Dr. D. Caldwell provided encouragement and support throughout my graduate studies. Dr. R. L. Smith's philosophical insights into life, education and the pursuit of happiness will long be remembered. My fellow students in the air-sea interaction group helped significantly along the way.

Computational facilities of Bonneville Power Administration and the National Center for Atmospheric Research were used extensively in the completion of this study.

My doctoral program was supported by the Office of Naval Research and the Link Foundation.

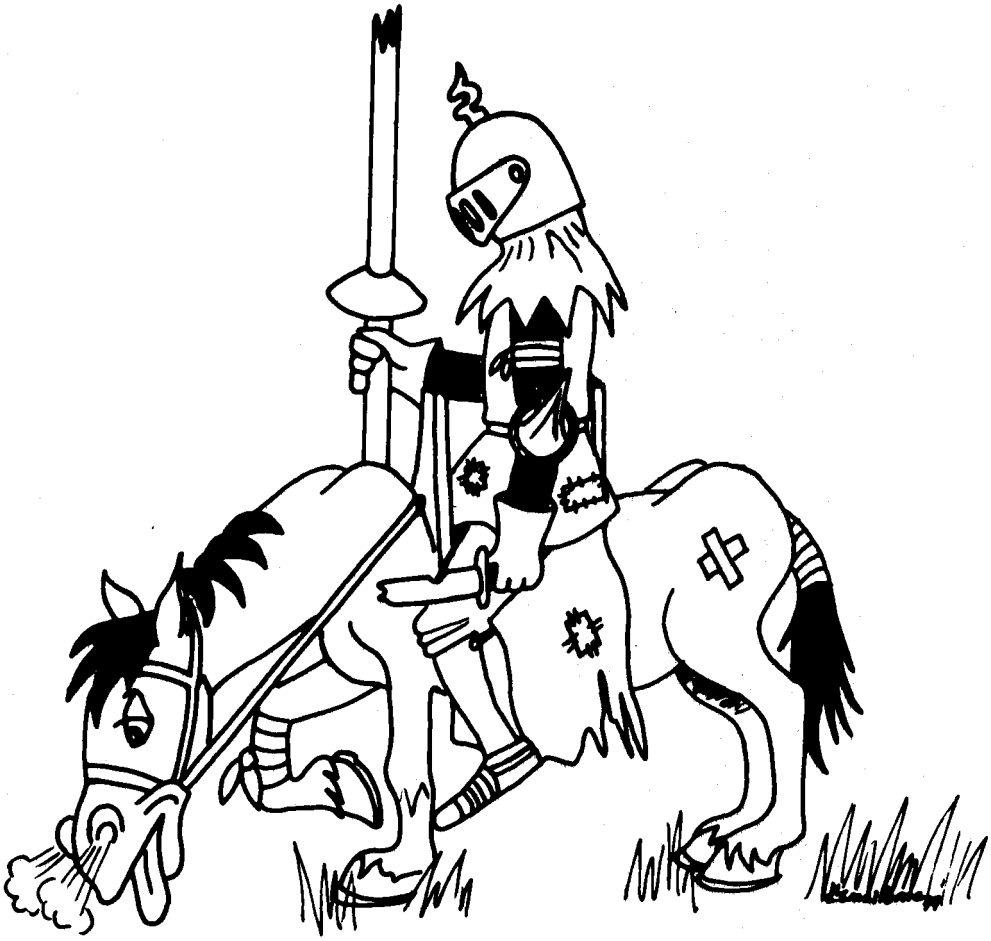

May everyone dream
the impossible dream
at least once in their life

TABLE OF CONTENTS

LIST OF TABLES

LIST OF FIGURES

SMALL SCALE TEMPERATURE STRUCTURE OF THE UPPER OCEAN

I. INTRODUCTION

This study examines the small scale temperature structure of the upper ocean in the context of the measurement and analysis of the heat balance at the sea surface, the radiometrically determined sea surface temperature, the distribution of downward irradiance with depth, and the temperature and salinity structure of the upper 300 m. The upper ocean is taken to include the oceanic thermal boundary layer adjacent to the air-sea interface, the well-mixed layer and the thermocline which often extends to a depth of 150 meters. Small scale structure refers to temporal variations in the temperature field associated with time scales of 1 second to a few days.

This study is modular. Each of Chapters II, III, IV, and V is a self-contained analysis of a particular phenomenon associated with upper ocean thermal structure. The radiative contributions to the processes determining the surface heat balance are presented in Chapter II. The distribution of solar radiation in the upper ocean is discussed in Chapter III. In Chapter IV, observations of the mixed layer are described and interpreted within the context of current theories. In Chapter V, temporal variations in the small scale structure of the radiometrically determined sea surface temperature are presented and interpreted within the framework of processes associated with the formation and destruction of the thermal boundary layer adjacent to the air-sea interface. Chapter VI summarizes the results from these analyses and their significance. The present chapter provides the motivation for this study and the background for the two observational programs germane to this analysis.

The measurements used in this study were made during two separate field programs, the Ocean Wave Experiment (OWAX) and

the NORPAX (North Pacific Experiment) process-oriented experiment POLE. Both programs utilized R/P FLIP as a research platform. For the Ocean Wave Experiment, FLIP occupied a station under free drift conditions approximately 60 miles off the coast of Baja California during the period 23 March 73 through 28 March 73. The direction of drift was southeast with positions ranging from 118° 17' W. Long, 31° 28' N. Lat. at the beginning of the experiment to 117° 35' W. Long, 30° 48' N. Lat. at the end of the experiment. During the POLE experiment FLIP occupied a station approximately 800 miles north of the Hawaiian Island Chain under free drift conditions from 28 January 74 through 14 February 74. The area of drift ranged from 35° 39' to 34° 36' N. Latitude and from 155° 05' to 155° 25' W. Longitude.

The experimental site for POLE is hydrodynamically complex. The Subtropical Front is known to meander between 32° -35° N. Lat. (Roden, 1973; Barnett, 1976). The region of the Trade Winds northeast of the Hawaiian Island Chain has evaporative flux rates in excess of 850 joules/cm^2 day^{-1} (Wyrtki, 1965). The Subtropical Water Mass formed in this region contrasts markedly with the less saline Eastern North Pacific Center Water characteristically encountered north of the Subtropical Front. The Horse Latitudes (region of low winds) are only 3° of latitude south of the observational area and the North Pacific Current is expected to affect the general hydrography of the region.

R/P FLIP has an overall length of 355 feet and is towed in the horizontal position to the area of scientific interest. Once on station, ballast tanks distributed through the aft 255 foot section of the vessel are flooded. When completely vertical the hull extends approximately 55 feet above the sea surface. Between depths of 300 to 150 feet the diameter of the hull is 20 feet and tapers to 12. 5 feet at the surface. FLIP has a natural period of 27 seconds for vertical motions

thus greatly reducing the FLIP's response to wave motions. For normal seas, vertical motions of FLIP are only about 10 cm amplitude and pitch and roll are less than 2° amplitude. These characteristics make FLIP an ideal platform from which to measure surface waves and the various contributions to the surface heat flux. The research platform is shown in Figure 1. 1.

During OWAX the sea surface temperature was measured radiometrically and wave height was observed with resistance wave gauges. The incident and reflected solar radiative fluxes and the net all-wave radiative fluxes were also measured. The temperature 25 cm above and below the interface was observed with a small sea surface follower float. Wind speed was determined with cup anemometers. The fluxes of latent and sensible heat were determined from standard meteorological observations and the thermal structure of the upper ocean monitored with XBTs. The instrumentation array as deployed from FLIP's port boom is shown in Figure 1. 2. Additional measurements during OWAX were made by Carl Friehe and Frank Champagne of the University of California, San Diego (UCSD).

During POLE the sea surface temperature was measured radiometrically and wave height was observed with resistance wave gauges. The incident and reflected solar radiative fluxes and the net all-wave radiative flux were also observed. A direct measurement of the net long-wave radiative flux was also made. The thermal structure of the upper 10 meters was observed continuously with fast response themistors suspended at fixed depths below the interface. Wind speed was measured with anemometers while the fluxes of latent and sensible heat were determined from standard meteorological observations. The temperature and salinity fields of the upper 300 meters were observed with an STD profiling device. The instrumentation array as deployed from FLIP's port boom is shown in Figure 1. 3. Carl Friehe and Kirt Schmidt (UCSD) made eddy

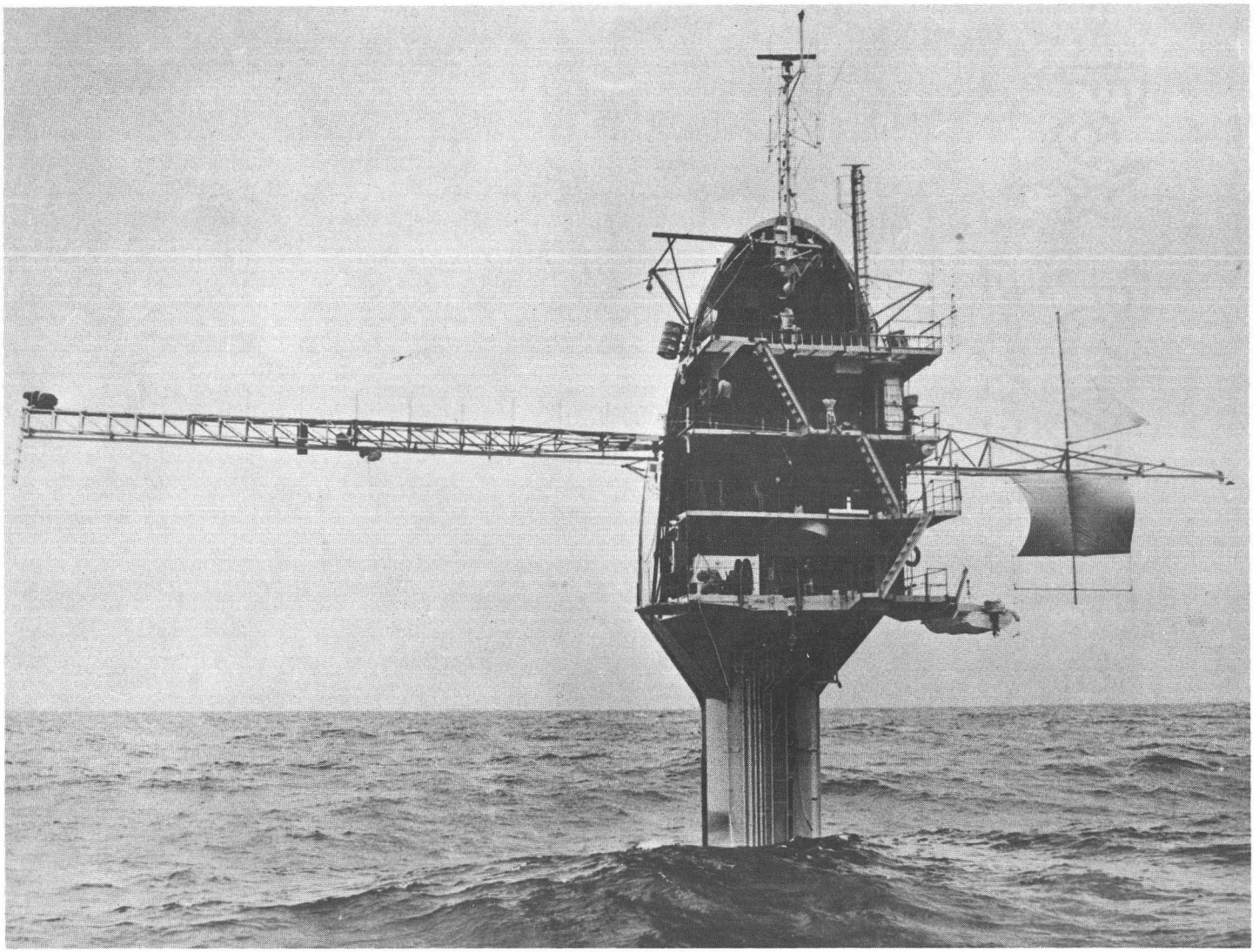

Figure 1.1 R/P FLIP in the vertical position with port boom deployed.

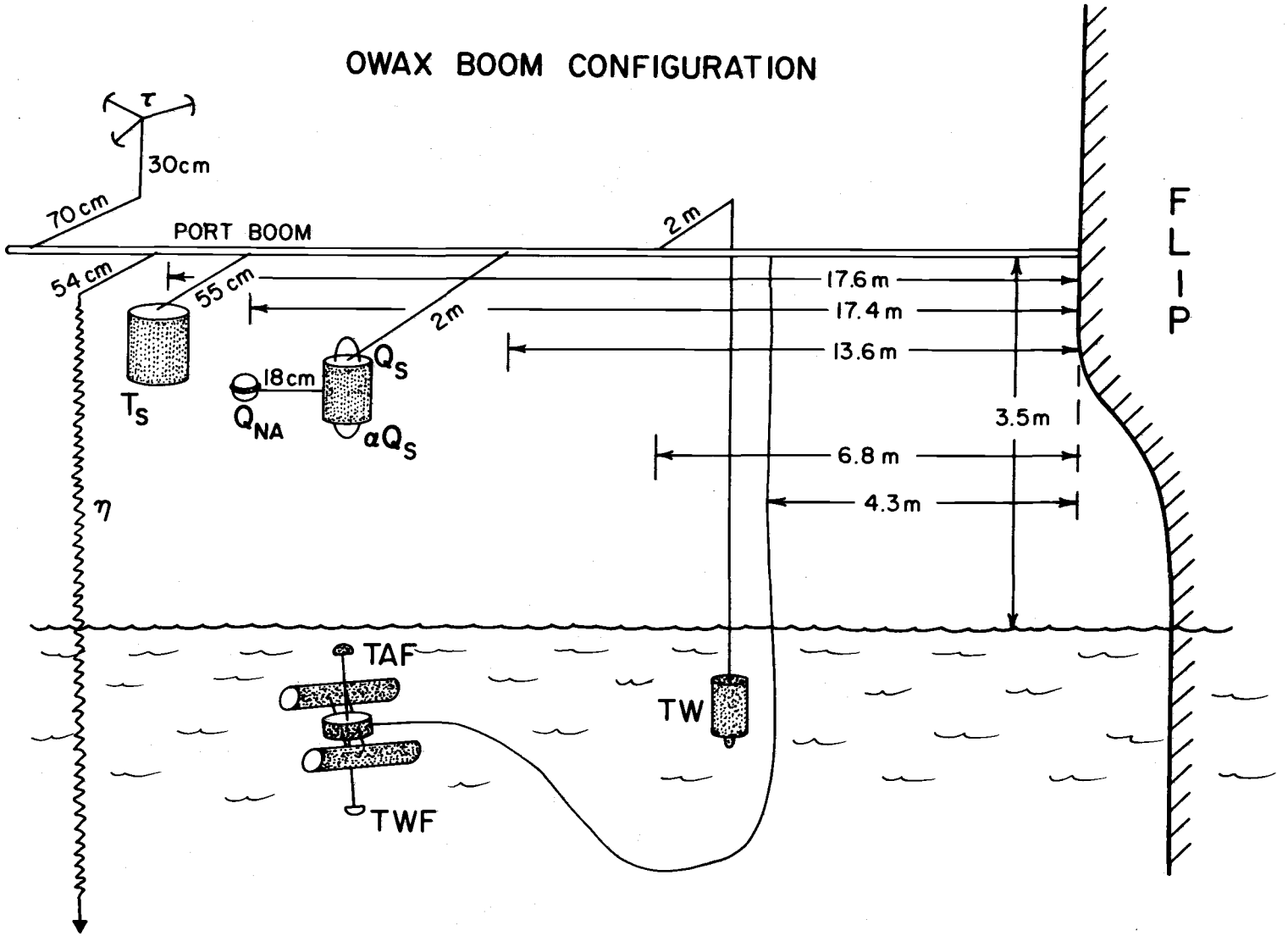

Figure 1. 2 The instrumentation array deployed during OWAX (Ocean Wave Experiment).

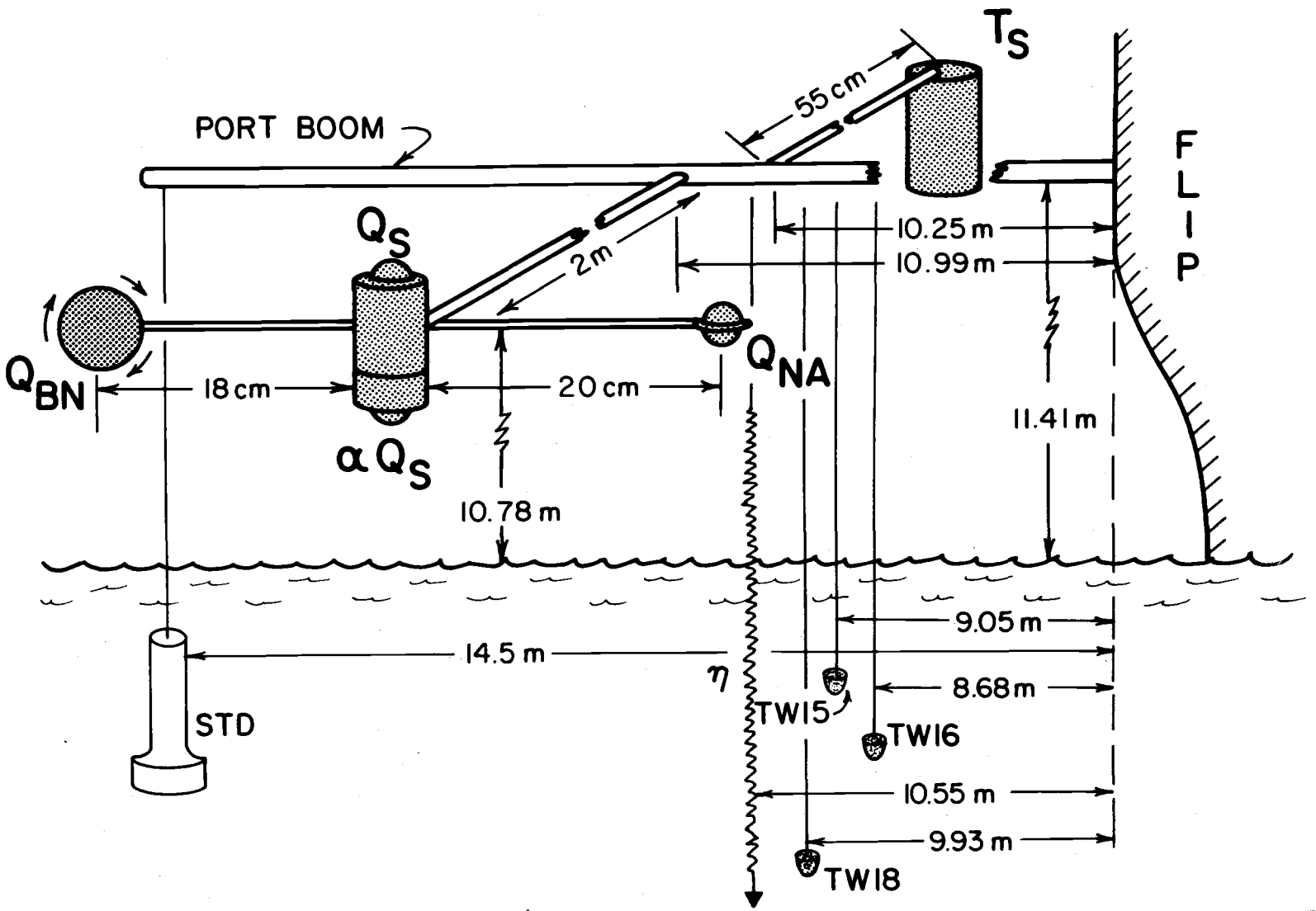

Figure 1.3 The instrumentation array deployed during POLE.

correlation measurements of the latent and sensible heat and momentum transfer and examined the drag coefficient as a function of increasing wind speed. Russ Davis (SIO) used a profiling current meter array to measure the velocity field.

One of the motivations for this study was to provide direct radiometric measurements of sea surface temperature, to compare these observations with bulk surface temperatures, and examine mechanisms affecting the radiation temperature. It is anticipated that infrared monitoring via satellites will prove an economical method for extending spatial and temporal observations of sea surface temperature. An improved understanding of mechanisms affecting sea surface temperature may aid in the development and interpretation of satellite measurements.

A second objective of this work is to present direct determinations of the incident and reflected solar radiative fluxes, the net all-wave radiative flux and the net long-wave radiative flux and to examine the accuracy of empirical laws relating these fluxes to routinely measured meteorological variables. Climatological models require the specification of these fluxes as components of the surface heat balance. It is unlikely that direct monitoring of these fluxes over extended regions for long periods of time will prove feasible. We must therefore improve our basic understanding of these empirical relations and their associated error limits.

A third objective is to examine the flux of solar radiation through the ocean surface. Modelling of physical, chemical and biological processes in the upper ocean is critically dependent upon a knowledge of the distribution of solar radiation with depth. The frequently assumed exponential decay of irradiance with depth is a poor approximation in the upper five meters of the ocean. Failure to properly parameterize the absorption of solar radiation with depth may lead to physically unreasonable predictions of the depth of the well-mixed layer.

Perhaps the most significant motivation of this thesis is the enhancement of our knowledge of the structure of small scale thermal processes. The heat capacity of the entire atmosphere is no more than that of a layer of water 2. 5 meters thick covering the globe. The excess heat content associated with a temperature anomaly of 1 degree C and 100 meters deep can, by itself, supply heat to the atmosphere at the normal rate for the entire season before it will be exhausted. (The NORPAX Program Plan, 1974). Our understanding of small-scale thermal processes must improve if analysis and prediction of the large scale variability associated with oceanic and atmospheric phenomenon is to be improved. An accurate heat balannce of the upper ocean is critical to the success of combined atmospheric-oceanic models of circulation, heat exchange and global climatology.

Most importantly, the results presently reported indicate the complex nature of upper ocean thermal structure. While it is felt that the conclusions presented are physically sound it is also recognized that no set of observations can yield generalizations applicable to the wide range of conditions found in the world's oceans. Men must still go down to the sea in ships. (With apologies to Melville.)

II. MID-OCEAN OBSERVATIONS OF ATMOSPHERIC RADIATION

Introduction

The heat flux budget at the air-sea interface can be expressed

$$Q_T = (1-\alpha) Q_S - Q_B + Q_{BC} - Q_L - Q_{SE} \qquad (2.1)$$

where Q_T is the total heat flux into the ocean, Q_S the incident solar flux, α the sea surface albedo, Q_B the long-wave flux emitted from the sea surface, Q_{BC} the long-wave flux emitted from the atmosphere, and Q_L and Q_{SE} the latent and sensible heat fluxes from the sea surface to the atmosphere. The second term in (2.1) represents the short-wave flux which penetrates the sea surface and dominates the heat budget of the upper ocean. The net long-wave flux, Q_{BN}, may be introduced in (2.1) to replace $Q_{BC} - Q_B$. The net long-wave flux, Q_{BN}, is highly variable and can be of the same order as the latent heat flux, Q_L. The net all-wave flux, $Q_{NA} = (1-\alpha) Q_S + Q_{BN}$ may be introduced to replace the first four terms on the right hand side of (2.1). Typically, the sensible heat flux, Q_{SE}, is an order of magnitude less than Q_L.

Few radiative flux measurements have been made at sea. Laevastu (1960) and Tabata (1964) report incident solar flux observations for regions of the Atlantic. Charnell (1967) and Schooley (1969) report net long-wave flux measurements for parts of the Pacific. Burt (1954) and Payne (1972) report values of albedo. Most recently Seckel and Beaudry (1973) investigate the radiation from sun and sky over the North Pacific Ocean. Reed and Halpern (1975) report both long and short-wave measurements off the Oregon coast.

The objectives of this Chapter are to describe observations of radiation over the mid-Pacific and to compare the observations with suggested parameterizations of radiative fluxes.

Instrumentation

A description of the instrumentation used to obtain the observations reported in this Chapter is given in Table 2. 1.

Estimates of the net long-wave flux are usually obtained by subtracting simultaneous measurements of the net radiation, Q_{NA}, and the net solar flux, $(1-\alpha)Q_S$. The accuracy of such estimates can be low during daytime because of the long-wave flux is frequently an order of magnitude less than the differenced quantities. In addition to this indirect method, flux values reported below were measured directly with a radiometer developed by Middleton Instruments and calibrated by C. S. I. R. O. (Paltridge, 1969). The instrument consists of a standard Funk net radiometer converted to a net long-wave radiometer by surrounding the radiometer with a black polythene sphere to optically filter short-wave radiation. To eliminate the effects of differential heating of sensor elements resulting from filter absorption of the solar radiation, the filter is rotated by an electric motor about the fixed Funk radiometer. Thus, heating of the filter is uniformly distributed resulting in a net null output to short-wave radiation. The instrument has zero response in the spectral range 0-2. 5 μ due to the absorptive properties of the polythene filter. Spectral response above 2. 5 μ increases rapdily; however, the two absorption bands of polythene centered at 6. 5 and 14 μ should be noted. Details of the filter characteristics are discussed in Paltridge (1969).

The signal from each instrument was transmitted by shielded cable to the platform laboratory and fed into an amplifier and voltage-offset device. Signals were recorded in strip chart form using an Esterline-Angus multipoint potentiometric recorder. A sampling rate of 5 or 10 samples per minute per channel was maintained throughout the experiment.

Table 2.1 Summary of instrumentation.

Device	Manufacturer	Physical parameter	Spectral response (microns)	Sensitivity	Accuracy	Time response (seconds)
Pyranometer	Eppley (8-48)	Incident flux, Q_S	0-2.5	$0.109 \frac{mV}{mWcm^2}$	±2-3%	15-20
Pyranometer	Eppley (8-48)	Reflectedf lux, αQ_S	0-2.5	$.112 \frac{mV}{mWcm^2}$	±2-3%	15-20
Net pyrgeometer with black polythene sphere	Middleton Co.	Net long wave flux, Q_{BN}	> 2.5	Short-wave $0.000 \frac{mV}{mWcm^2}$ Long-wave $0.045 \frac{mV}{mWcm^2}$	±7.5%	15-20
Net radiometer	Swissteco Pty. Ltd.	Net all wave flux, $Q_{NA} = (1-\alpha)Q_S + Q_{BN}$	0.3-60	Short wave $0.459 \frac{mV}{mWcm^2}$	±2.5%	15-20
Radiation thermometer	Barnes Engineering Co. PRT-5	Sea surface temperature	8-14	--	±0.2 deg.	0.3

Observations

Direct measurements of the incident solar, reflected solar, net all-wave and net long-wave fluxes were made from the R/P FLIP during the period 2 to 14 February 1974 as a part of the POLE experiment, a component of the North Pacific Experiment (NORPAX). The sea surface temperature was also observed using a radiation thermometer. Continuous 24 hour sampling of all variables was maintained. The FLIP occupied a station approximately 800 miles north of the Hawaiian Island chain under free drift conditions. The area of drift ranged from 35° 09' to 34° 56' N. latitude and 155° 05' to 155° 25' W. longitude. R/P FLIP provides an ideal platform from which to make measurements of radiative fluxes because of the stability induced by having about 300 ft. of her length submerged (as a large spar buoy). Hence errors due to variable sensor orientation as occur on conventional ships in response to surface waves and swell are largely eliminated. Vertical motions of FLIP were about 10 cm amplitude and pitch and roll amplitudes were about 2°.

The locations of the radiometers are shown schematically in Figure 2.1. Instrumentation was mounted from the port boom which was 11.4 meters above mean sea level. At a point 11.0 meters from the hull along the boom, a supporting arm for the radiometers was mounted perpendicular to the boom. This arrangement served to minimize possible shadowing of the radiometers by the hull and the boom.

Analysis

A digital representation of the data base was obtained through the use of a chart digitizer. The records were merged to obtain a continuous time series of the measured variables over the experimental period. Occasional errors caused by radio interference were removed from the records by interpolation. Less than 1% of

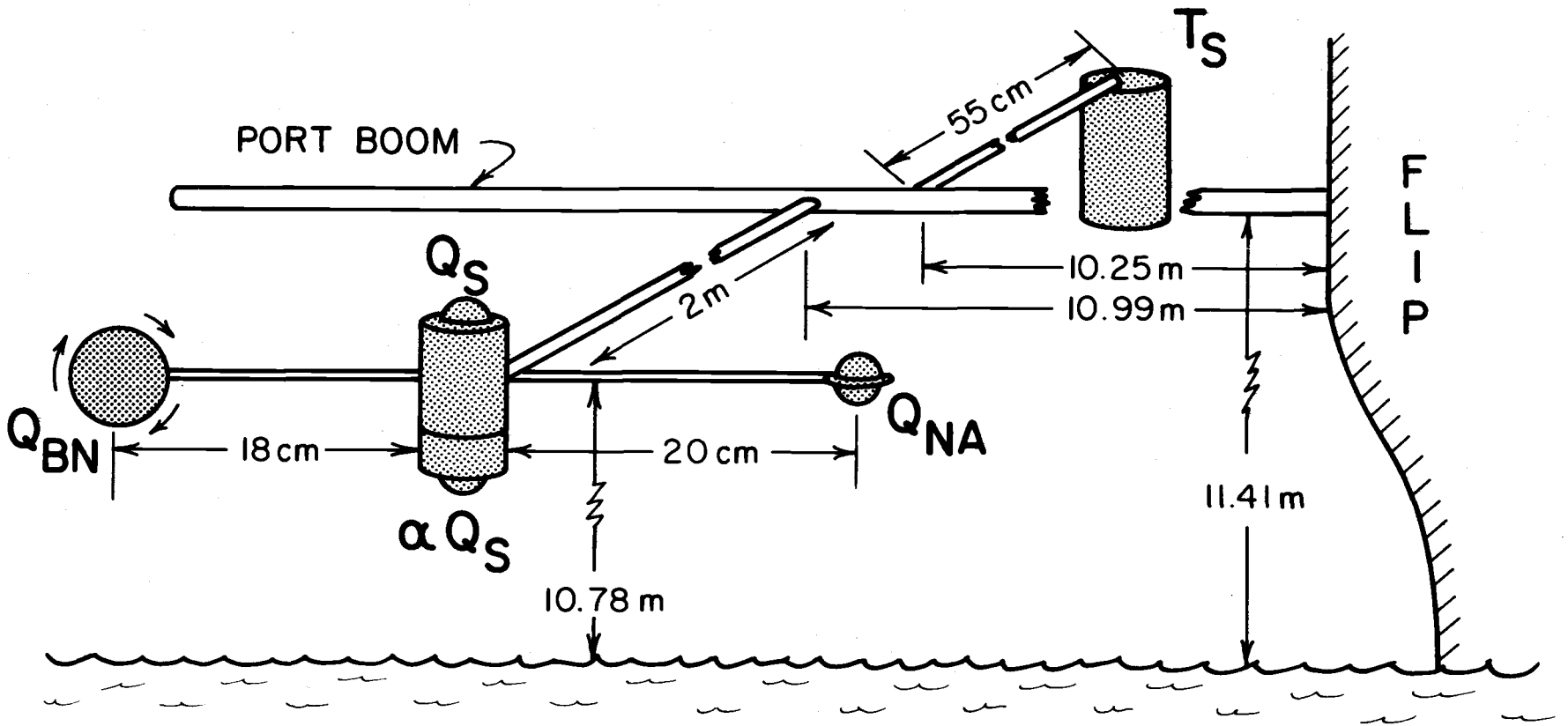

Figure 2. 1 Schematic diagram illustrating the instrumentation used to measure the incident solar flux, Q_S, the reflected solar flux, αQ_S, the net all-wave radiation, Q_{NA}, the net long-wave radiation, Q_{BN}, and the sea surface temperature, T_S.

the data was affected by such interference. From the resulting time series, sequential one and fifteen minute averages were constructed. The fifteen minute averaged time series for the experimental period are shown in Figure 2. 2.

A summary of the mean solar flux observations is provided in Table 2. 2. Routine visual estimates of cloud amount, C (tenths) and type were also made. The mean cloud cover estimates of Table 2. 2 represent a time-weighted average of the fraction of observed cloud cover. Stratus and cirrus formations were the dominant cloud types observed. No accurate estimate of cloud height during the observations is available.

Large daily variations in the short-wave component of the radiative flux are well correlated with mean daily cloud estimates. A maximum mean daily net solar flux of 34. 59 milliwatts cm^{-2} was observed during a period of nearly clear sky conditions (C=0. 2) while the minimum mean daily value of 14. 11 milliwatts cm^{-2} corresponded to completely overcast sky conditions (C=1. 0). Such variability in the net solar flux corresponds to a range of 1370 to 559 joules cm^{-2} day^{-1} transmitted into the upper ocean.

Albedo

The albedo of the sea surface is defined as the ratio of the upward to the downward solar flux immediately above the air-sea interface. Two sources contributed to the upward component; emergent irradiance due to back scattered light from below the sea surface and irradiance reflected from the sea surface. Payne (1971) suggests that the ratio of emergent to downward flux is about 0. 005.

Saunders (1967) suggested a relationship between albedo and solar altitude for clear skies. Payne (1972) analyzed observations utilizing Saunders' relationship to represent the albedo, α, as a function of the solar altitude, θ, and the atmospheric transmittance, T.

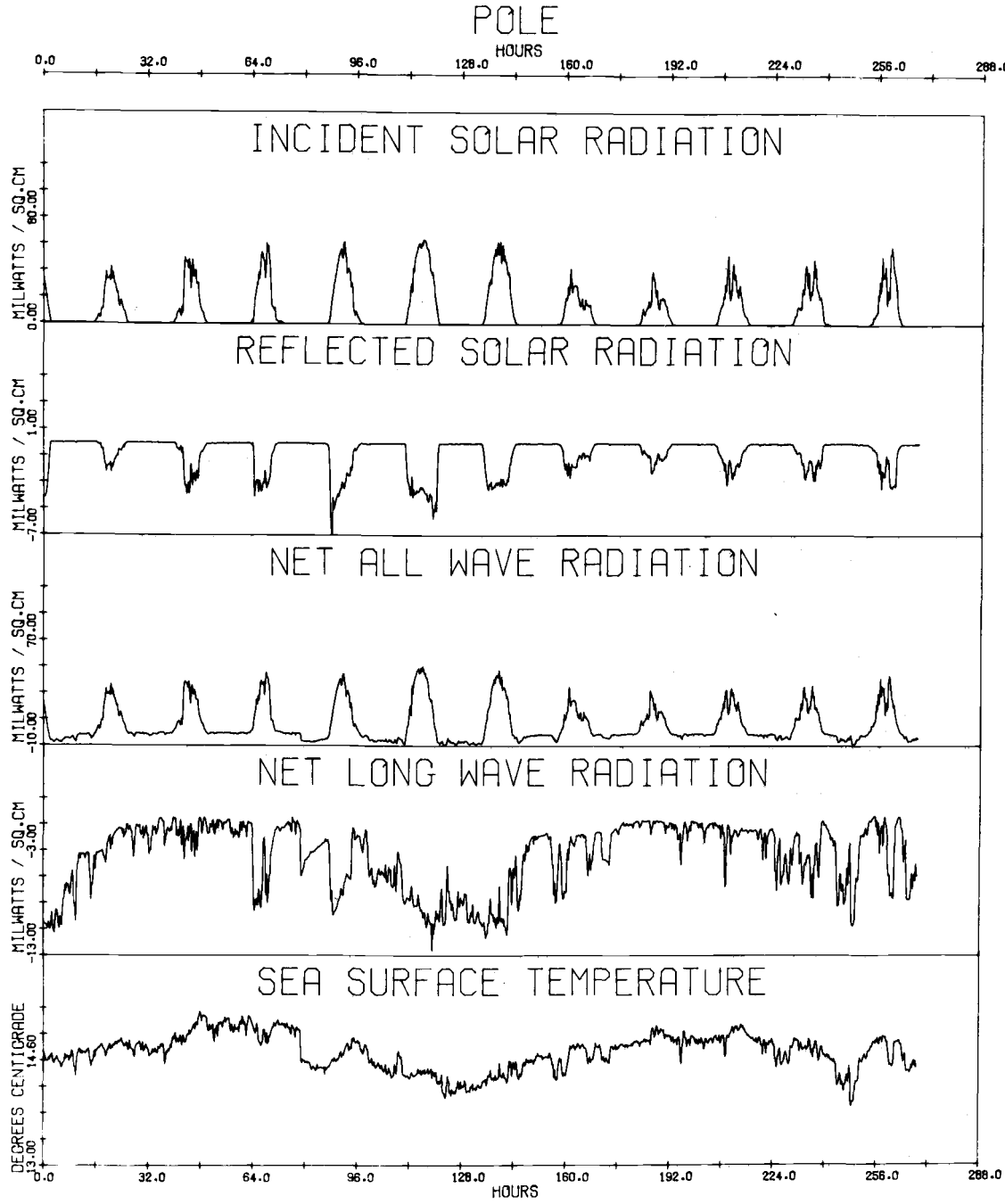

Figure 2.2. Time series of the incident solar flux, Q_S, the reflected solar flux, αQ_S, the net all-wave flux, Q_{NA}, the directly measured net long-wave flux, Q_{BN}, and the radiometrically measured sea surface temperature, T_S, averaged over 15 minute intervals. A negative flux implies oceanic heat loss.

Table 2.2 Mean daily values of the various components of the solar flux as well as the net-all wave flux, sea surface albedo and cloud cover. Flux values are reported in milliwatts cm^{-2} while cloud cover is designated in tenths.

Day	Incident flux	Reflected flux	Net solar flux	New allwave flux	Albedo	Clouds
03 Feb. 74	18.73	-1.03	17.69	15.76	.055	0.9
04 Feb. 74	21.44	-1.59	19.85	17.82	.074	1.0
05 Feb. 74	24.37	-1.73	22.64	17.79	.071	0.6
06 Feb. 74	29.02	-2.61	26.42	19.67	.090	0.2
07 Feb. 74	38.11	-3.51	34.60	26.14	.092	0.2
08 Feb. 74	34.15	-2.39	31.76	22.21	.070	0.4
09 Feb. 74	16.86	-1.15	15.71	12.08	.068	0.9
10 Feb. 74	15.02	- .91	14.11	11.94	.061	1.0
11 Feb. 74	19.77	-1.25	18.52	14.92	.063	1.0
12 Feb. 74	18.65	-1.15	17.50	13.50	.061	0.9
13 Feb. 74	23.27	-1.53	21.74	18.22	.066	0.9

The atmospheric transmittance was included to account for the dependence of α on the radiance distribution from the sky. The atmospheric transmittance is defined as the ratio of the downward irradiance with an atmosphere to that without an atmosphere, i. e.

$$T = \frac{Q_S r^2}{S \sin\theta} \qquad (2.2)$$

where S is the solar constant, taken as 135 milliwatts cm^{-2}, and r is the ratio of actual to mean earth-sun separation. For the case of no atmosphere (T=1. 0) the incident flux is directly dependent upon the altitude of the sun. Increased atmosphere and cloud cover result in enhanced absorption, reflection, and scattering of the incident solar flux. The overall effect is to produce a more nearly uniform radiance distribution, thus reducing the dependence of albedo on solar altitude. In the limit of severe overcast conditions ($0.0 \leq T \leq 0.1$) a nearly isotropic radiance distribution results. The use of transmittance to parameterize albedo may be questionable at low sun angles because T may increase without limit (finite sky radiation) as θ approaches zero.

Albedo values were calculated from 15 minute averages of the incident and reflected fluxes. Corresponding values for the solar altitude and atmospheric transmittance were also computed. The resulting data set was sorted into two-degree intervals of solar altitude and averaged over intervals of 0. 1 in transmission coefficient. The resultant values of albedo, as well as the number of original data values used to obtain a given estimate, are shown in Table 2. 3. This table may be compared to a similar table of smoothed observations in Payne (1972).

In Figure 2. 3 albedo values in particular ranges of atmospheric transmittance are shown as a function of solar altitude. The scatter of the data for low solar altitudes is likely because the cosine response of the radiometers is poor for solar altitudes less than five degrees

Table 2.3 Albedo values averaged over 2° intervals of solar altitude and 0.1 intervals of atmospheric transmittance. The numbers in parentheses indicate the number of raw albedo values used to compute the final value shown. An asterisk indicates that the difference between the value shown and smoothed values given by Payne (1972) is $\leq .01$.

TRANSMISSION COEFFICIENT	SOLAR ALTITUDE																				
	0°	2°	4°	6°	8°	10°	12°	14°	16°	18°	20°	22°	24°	26°	28°	30°	32°	34°	36°	38°	40°	42°
.05		.054* (2)	.394 (1)	.083 (2)	.069* (2)	.083 (1)	.052* (2)	.019 (1)		.020 (2)	.005 (1)	.009 (1)	.055* (2)	.071* (2)								
.15		.122 (8)	.090 (6)	.060 (11)	.051 (7)	.062* (9)	.056* (5)	.060 (1)	.060* (7)	.067* (3)	.057* (4)	.064* (4)	.065* (4)	.056* (2)	.058* (4)	.058* (2)	.058* (1)	.062* (2)	.064* (5)	.065* (2)	.061* (5)	.061* (2)
.25		.050 (5)	.072 (2)	.042 (1)	.064 (4)	.068 (2)	.074* (4)	.079 (6)	.056 (2)	.072* (5)	.057 (3)	.061* (7)	.065* (6)	.059* (7)	.060* (3)	.062* (5)	.061* (4)	.060* (3)	.063* (4)	.061* (4)	.061* (11)	.058* (3)
.35			.229* (3)		.206 (1)	.064 (1)		.078 (3)	.079 (5)	.069 (2)	.080* (3)	.078* (2)	.070* (3)	.060 (2)	.062* (5)	.061* (5)	.061* (6)	.060* (3)	.060* (7)	.060* (6)	.060* (7)	.058* (1)
.45		.157 (3)					.208 (1)			.102 (1)	.096 (1)	.108* (1)	.070 (1)	.085* (2)	.072* (2)	.070* (3)	.062* (4)	.064* (5)	.063* (6)	.061* (15)	.061* (8)	.060* (1)
.55			.361 (1)		.332* (4)	.267* (3)	.225 (3)	.138 (1)	.225 (3)	.120 (1)		.084 (1)	.100* (2)	.089* (4)	.082* (3)	.081* (3)	.066 (2)	.069* (4)	.068* (3)	.065* (12)	.057* (3)	.060* (1)
.65			.165 (1)	.197 (1)		.400 (1)	.363 (1)	.181 (1)	.150 (3)	.155* (4)	.136* (6)	.130 (2)	.107* (2)	.107* (1)	.088 (4)	.079* (4)	.072* (4)	.065* (5)	.062* (8)	.058* (10)	.055* (8)	
.75												.118* (1)		.090* (1)		.081* (1)	.077* (4)	.067* (3)	.063* (1)	.060* (5)	.054* (3)	
.85																						

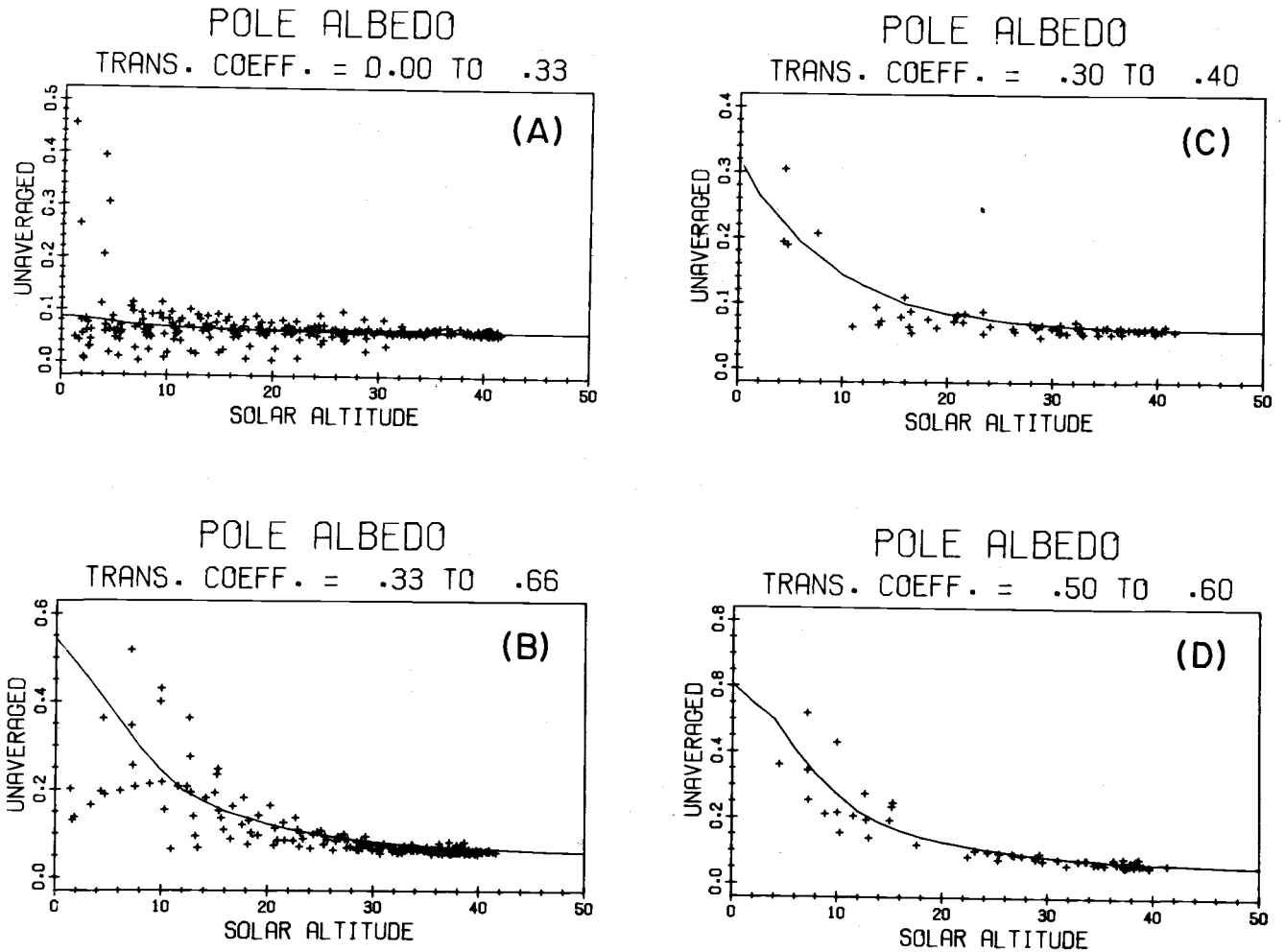

Figure 2. 3 Unsmoothed albedo values as a function of solar altitude for the various ranges of atmospheric transmittance shown. The curves are due to Payne (1972).

and because of generally increasing uncertainty in the measurements as the magnitude of the irradiance decreases. Very small variation with altitude is observed in Figure 2.3A suggesting as one might expect that the sea surface albedo for overcast conditions ($0.0 \leq T \leq 0.33$) has a negligible dependence on solar altitude. The mean albedo for this sample ($N = 232$) is $.066 \pm .04$ where the error limit is one standard deviation. The observations agree well with Payne's suggested curve; however, a constant albedo independent of solar altitude fits the observations better. For the range of atmospheric transmittance most nearly approaching an isotropic radiance distribution ($0.0 \leq T \leq 0.1$) the mean albedo is $.060 \pm .01$. In Figure 2.3B, albedo is shown as a function of solar altitude for intermediate transmittance ($0.33 \leq T \leq 0.66$). Figures 2.3C and 2.3D provide finer resolution with respect to atmospheric transmittance. These results generally support Payne's (1972) suggested curves and the theoretical estimates of reflectivity (Saunders, 1967) used by Payne in the extrapolation of smooth albedo curves to low solar altitude, a region in which Payne had few observations. The only systematic departure of the observations from Payne's curves are for low solar altitudes and low transmittance where a constant value of albedo is suggested by our observations.

Representative plots of albedo as a function of atmospheric transmission for a given range of solar altitude are shown in Figure 2.4. The scatter in the data is seen to be largest for the range of low sun angles ($0° < \theta < 15°$) as previously explained. Some of the scatter in the plots may be due to real variations caused by variations in solar altitude within each range of sun angles. The distribution of points in Figure 2.4A corresponding to overcast conditions ($T \leq 0.3$), suggests Payne's smoothed curve may yield albedo values somewhat larger than our observations justify. For the high altitude range, $30° \leq \theta \leq 45°$, the scatter in the data is significantly reduced and the

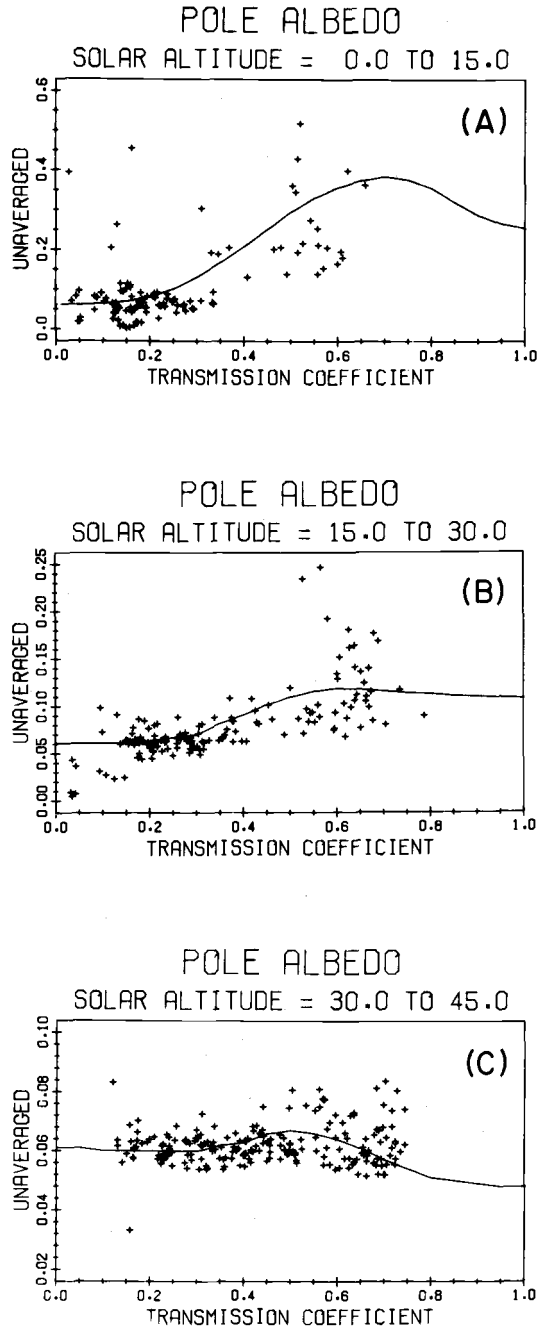

Figure 2.4 Unsmoothed albedo values as a function of atmospheric transmittance for the various ranges of solar altitude shown.

general shape of the albedo distribution predicted by Payne is confirmed. The presence of an increase in albedo in the range of transmittance, $0.3 \leq T \leq 0.5$, is supported by the data of Fig. 2.4C. However the observations do not support the decrease in Payne's curve following the maximum.

To determine the effect of sea surface roughness on albedo, the observed values were sorted by 15° intervals of solar altitude and normalized with respect to the mean albedo for the given range of solar altitude. Mean values averaged over 2 m/sec. bands were plotted as a function of wind speed. Insufficient data at low solar altitudes precludes discussion for the range $\theta \leq 15°$. No discernible dependence on sea surface roughness was evident in the large scatter associated with the high altitude range, $30° \leq \theta \leq 45°$. Values in the intermediate range, $15° \leq \theta \leq 30°$, are shown in Figure 2.5. The data qualitatively support decreasing albedo with increasing windspeed as observed by Payne (1972).

The average daily albedo values of Table 2.2 show expected correlation with daily cloud cover. The seven days of high mean cloud cover ($0.9 \leq C \leq 1.0$) have an average albedo of 0.064. This value corresponds well with Payne's value of 0.061 corresponding to a nearly isotropic radiance distribution. For the relatively cloudless period (C=0.2) higher mean daily albedo values are found 0.090 and 0.092 for 6 and 7 February when the average cloud cover was 0.2. Such augmented values are due to the large albedo values associated with low solar altitudes under clear sky conditions. A climatological estimate of albedo, 0.08 (Payne, 1972), for the month of February at 35° N latitude in the Atlantic agrees with the mean value for the experin ental period, 0.07 ± 0.01.

Long-Wave Flux

Two independent measurements of the net long-wave radiative flux were made during POLE. A direct measurement of the net

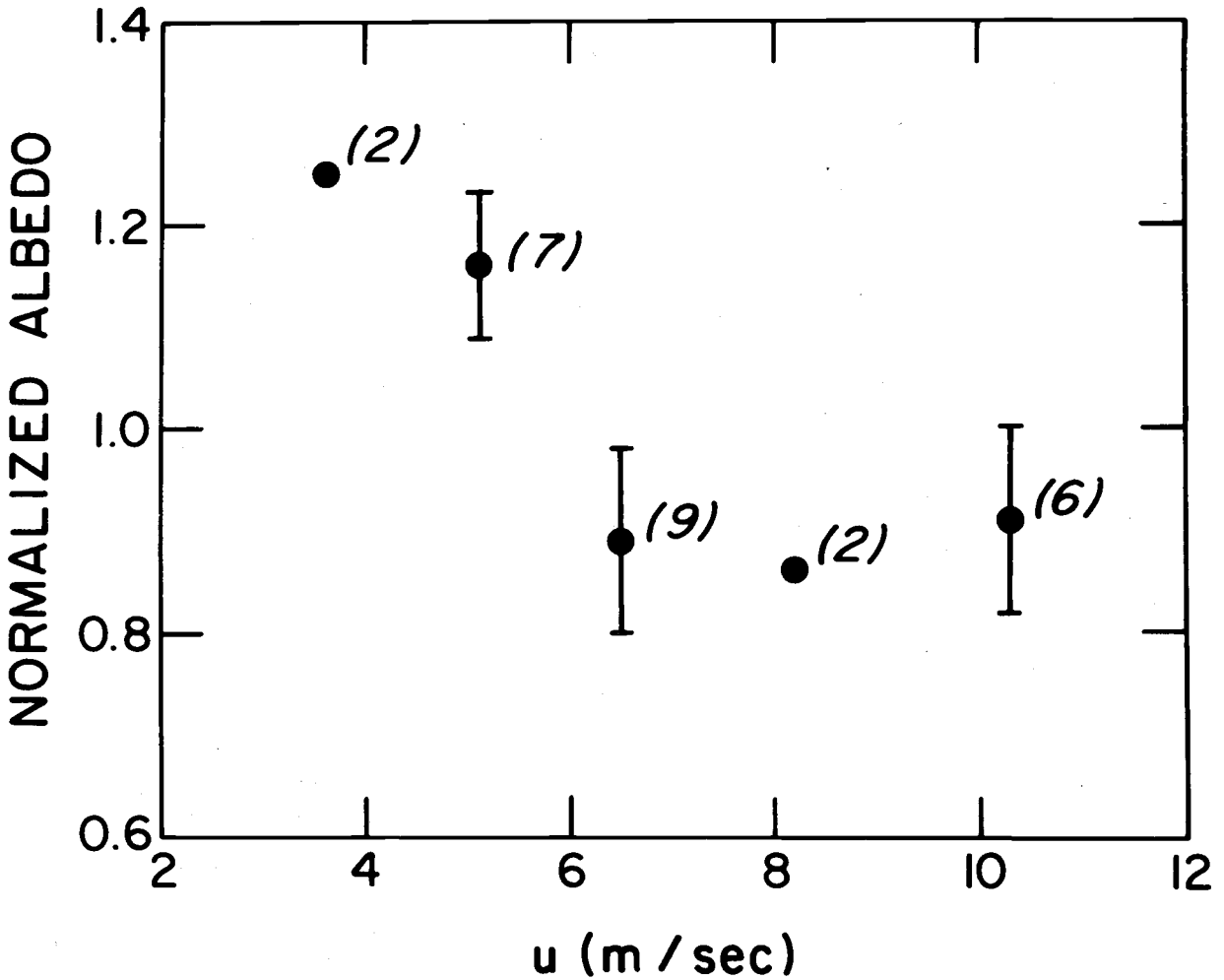

Figure 2.5 Normalized albedo vs. wind speed, transmission coefficient > 0.6, solar altitude 15 to 30 degrees. Numbers in parentheses are the number of values averaged to obtain each point. Vertical bars represent the standard errors.

long-wave flux, Q_{BN}, was obtained by using a recently developed Middleton net long-wave radiometer (described above). Values of the long-wave flux obtained in this fashion are independent of all other radiative flux measurements made during the experimental period. Values of Q_{BN} so obtained are reported as directly measured values. The more traditional approach relies upon differencing measurements of the net all-wave radiation, $(1-\alpha)Q_S + Q_{BN}$, and the net solar flux, $(1-\alpha)Q_S$. Values of the net long-wave flux obtained in this fashion are reported as indirectly measured values.

In Figure 2.6, time series of the 15 minute averages of the directly measured net long-wave flux, the indirectly measured net long-wave flux, the flux difrerenced defined as the directly measured value minus the corresponding indirectly measured value, the net all-wave flux with daytime values set to zero and the radiometrically measured sea surface temperature are shown. The daily mean atmospheric conditions under which these measurements were made are shown in Table 2.4. Two features are immediately evident. First, a high coherence between the long-wave fluxes and the sea surface temperature is exhibited as predicted by the Stefan-Boltzmann relation. Second, nighttime variation in the difference signal is seen to be small and near zero. As the net solar flux is zero during nighttime periods, the net all-wave radiometer effectively measures the net long-wave flux directly for such periods. Such qualitatively good agreement during evening periods suggests that the net long-wave radiometer may provide direct accurate daytime measurements of Q_{BN}. In addition, the high frequency variations in the difference signal appear to occur only during daytime intervals. For such periods the difference signal is not uniformly distributed about zero mean but rather significantly skewed toward high difference values strongly suggesting that the indirectly measured flux values are systematically larger than the directly measured values. The accuracy of the

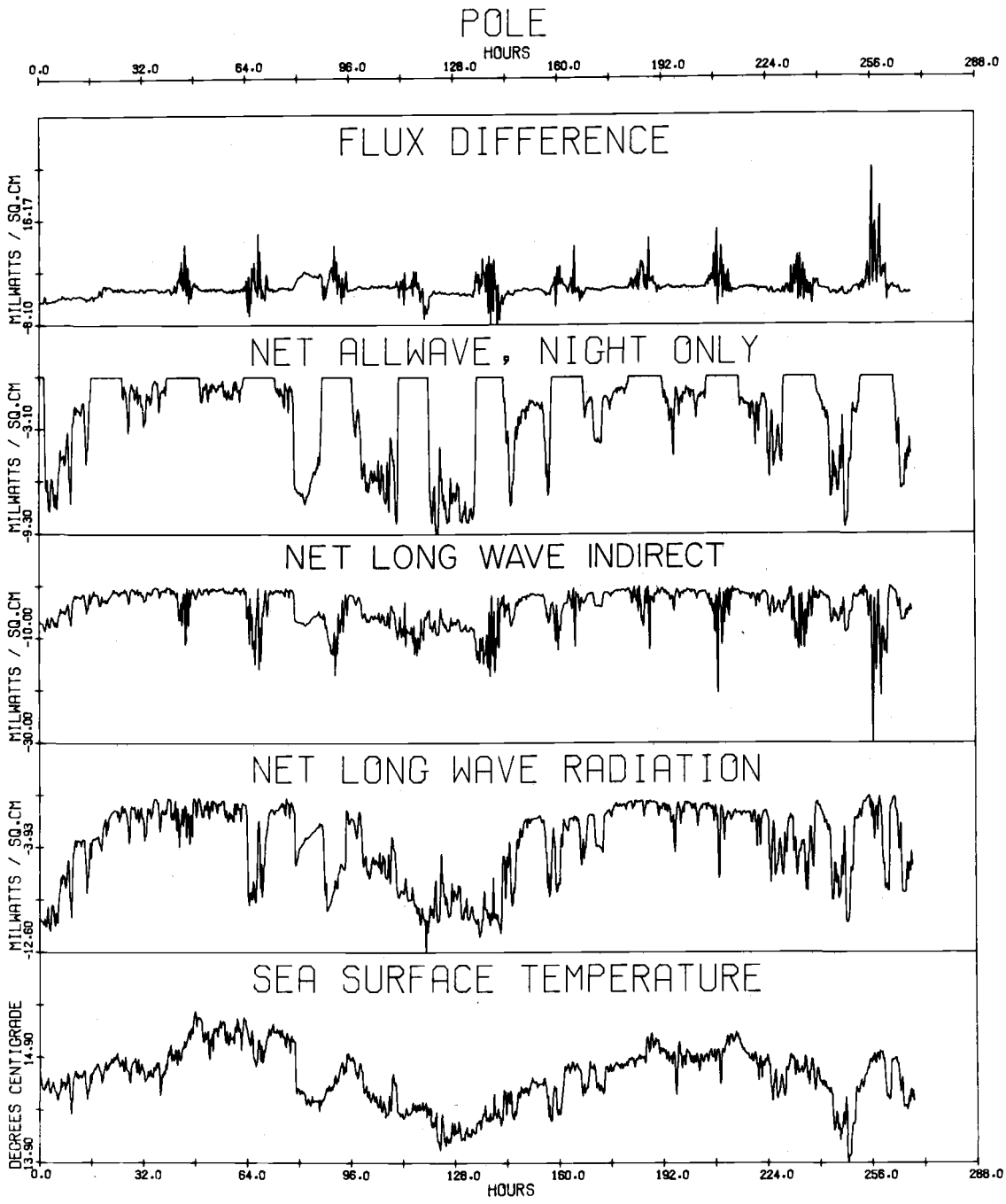

Figure 2.6. Time series of sea surface temperature, the directly measured long-wave flux, the calculated long-wave flux, the nocturnally measured net-all wave flux (net long-wave flux) and the flux difference averaged over 15 minute intervals. The flux difference is positive if the calculated flux exceeds the directly measured net long-wave flux.

Table 2.4 Mean diurnal atmospheric conditions under which the measurements of the net long-wave flux, Q_{BN}, were made.

Date	Avg. clouds	Avg. sea surf. temp. °C	Avg. air temp. °C	Avg. atmos. vapor pres. (mb)
03 Feb. 74	1.0	14.76	14.61	13.78
04 Feb. 74	1.0	14.98	14.83	16.73
05 Feb. 74	.8	15.06	15.56	17.19
06 Feb. 74	.3	14.63	14.78	13.72
07 Feb. 74	.2	14.35	13.22	9.27
08 Feb. 74	.4	14.37	14.33	11.46
09 Feb. 74	.9	14.66	13.94	15.50
10 Feb. 74	1.0	14.91	14.56	15.60
11 Feb. 74	1.0	14.93	14.22	14.21
12 Feb. 74	.9	14.64	15.22	15.37
13 Feb. 74	.7	14.64	15.72	15.88

indirectly measured values is often low as the net long-wave flux is frequently an order of magnitude less than the actually measured and differenced quantities. Small dissimilar departures from nonlinearity of the calibration curves of the radiometers would explain the bias.

For daytime periods, maximum and minimum values of the directly measured flux are -10.15 and -0.37 milliwatts cm^{-2} respectively. Corresponding values for the indirectly measured net long-wave flux are -9.55 and -1.93 milliwatts cm^{-2}. Nocturnal measurements provide a maximum value of -8.25 milliwatts cm^{-2} and a minimum value of -0.76 milliwatts cm^{-2} for the net long-wave flux as measured by the net all-wave radiometer with corresponding values of -7.36 and -0.75 milliwatts cm^{-2} respectively for the net long-wave radiometer. Charnell (1967) reports nocturnal measurements of long-wave thermal radiation made in the area of the Hawaiian Island Chain under clear sky conditions in the range of -6.27 to -8.37 milliwatts cm^{-2}. These values show good agreement with both types of nocturnal measurements reported above. Moreover, the maximum value of -7.36 milliwatts cm^{-2} measured with the net long-wave radiometer corresponds most favorably with the mean value of Charnell's clear sky observations, -7.32 milliwatts cm^{-2}. Charnell's minimum values of -2.79 to -4.18 milliwatts cm^{-2} for overcast sky conditions are significantly larger than the corresponding values presently reported. Variation in cloud type (cumulus off Hawaii, stratus and cirrus during POLE) probably accounts for this difference. Measurements made by Reed and Halpern (1975) off the Oregon coast exhibit a range of -6.97 to -0.70 milliwatts cm^{-2} in good agreement with the values reported here. Such agreement might be expected as the predominant strato-cumulus clouds observed off Oregon closely approximate the stratus clouds observed during POLE. The directly measured value of -7.36 milliwatts cm^{-2} during POLE corresponds favorably with the maximum value obtained off the Oregon coast. A summary of this intercomparison

Table 2.5 Comparison of various measurements of the net long-wave flux made over the Pacific Ocean. All units are milliwatts cm^{-2} with an asterisk (*) indicating only nocturnal measurements appear in this table.

Investigator	Date	Location	Maximum value	Minimum value
*Charnell	March-June 1965 September 1965	Hawaiian Islands	-6.27 to -8.37 (clear sky)	-2.79 to 14.18 (overcast)
Reed Halpern	July-August 1973	Off Oregon Coast	-6.97	-0.70
*Simpson Paulson (net long-wave radiometer)	February 1974	Pole Site (35^{o}, 155^{o})	-7.36	-0.75
Simpson *Paulson (net all-wave radiometer)	February 1974	Pole Site (35^{o}, 155^{o})	-8.25	-0.76

*Indicates nocturnal measurements

appears in Table 5.

The net long-wave flux difference, defined as the difference between directly and indirectly measured fluxes, shown in Fig. 2.6 indicates estimates of the net long-wave flux obtained through the differencing of measured quantities systematically overestimates the value of Q_{BN} during daytime periods. However, nocturnal agreement between the two methods of measurementis within 2% on average over the entire data set. Such uncertainties associated with the nocturnal comparison of the net all-wave and net long-wave flux determinations are well within the stated accuracies of the radiometers.

Maximum net long-wave flux is not always associated with periods of maximum sea surface temperature. Periods of large fluxes are associated with low atmospheric vapor pressures and clear sky conditions. Nocturnal measurements (~12 hour average) on 4 Feb. 74, characterized by maximum mean cloud (C=1.0), high atmospheric vapor pressure (16.73 mb) and the highest average diurnal sea surface temperature (15.06° C) for the experiment yielded an average flux of -.75 milliwatts cm^{-2} compared to a value of -7.36 milliwatts for the evening of 7 Feb. 74 when all three relevant parameters attained their minimum experimental values (C=0.2, V.P. = 9.27 mb, T_S = 14.35° C). Two distinctive physical mechanisms are operative. As the sea surface temperature rises, evaporation increases and a warm moist air mass is formed above the air-sea interface. This air layer is effective in re-radiating the outgoing long-wave flux back to the sea surface. However, it is precisely in this region that the wavelength of maximum black body emission for the normal range of sea surface temperatures is predicted by the Wien displacement law, $\lambda_m = 10\mu$. Cloud droplets, however, unlike water vapor absorb and emit energy at all wavelengths and hence partially reduce the long-wave flux that would otherwise escape through the atmospheric

window. Finally, the data for the entire experimental period suggest more long-wave flux is emitted during the daytime than during evening periods. Such a result is consistent with the generally warmer sea surface temperatures and less cloud cover (see e. g. Dorman et al.) encountered during daylight hours. (Observations of net long-wave radiative flux over the Pacific are summarized in Table 2. 5.)

Parameterizations

Short-wave Component

Numerous empirical relations have been advanced to estimate the attenuation of the incident solar flux due to the presence of clouds. Relations due to Kimball (1928), Mosby (1937), Gabites (1950), Houghton (1954), Berliand (1960) and Budyko (1974) are given in Table 2. 6. The intent of the various authors was to provide mean monthly climatological estimates of the solar flux at the surface. Application of such formulae to observations averaged over a few days can lead to significant errors in the estimates. Comparison between predicted values based on average daily cloud cover amounts and the measured daily averages of incident solar flux is shown in Table 2. 6. A positive difference implies the calculated estimate exceeds the measured value. In general, such empirical formulae tend to overestimate the amount of flux. For the twelve day experimental period percentage differences ranged from a 5. 5% underestimate (Budyko) to a 12. 7% overestimate (Gabites). However, the mean standard deviation for these relations was ±29. 6% with a minimum value of ±23. 5% (Gabites) and a maximum value of ±40. 6% (Houghton). The use of such formulae for time scales shorter than a month must be approached with caution.

A possible explanation for the inadequacy of these formulae to accurately estimate the flux values over diurnal time scales may be their failure to include the effects of different types of clouds. In

Table 2.6 Comparison of the commonly used empirical relations for estimating the incident solar flux. A positive percentage difference implies the calculated estimate exceeds the measured value.

Reference	Relation	Percent difference	Standard deviation
Kimball (1928) Mosby (1936)	$Q_S = Q_O (1.0-0.71C)$	2.6%	±24.4%
Gabites (1950)	$Q_S = Q_O (1.04-0.71C)$	12.7%	±23.5%
Houghton (1954)	$Q_S = Q_O (1.28-1.03C)$	9.4%	±40.6%
Berliand (1960) Budyko (1974) Wyriki (1965)	$Q_S = Q_O (1-r) (1-ac-bc^2)$	- 5.5%	±30.2%
Lumb (1964)	$Q_S = 135\ fs$	- 5.0%	±10.0%

addition, linear relationships between cloud amounts and short-wave flux may be in error. A linear relationship is not evident between the average daily incident flux and the average daily cloud cover observed during POLE. Observations by Reed and Halpern (1975) off the Oregon coast also failed to establish linear dependence between daily cloud cover estimates and measured incident solar fluxes. Another factor may be that visual estimates of cloud cover made during oceanographic cruises are often too crude for purposes of flux estimation.

Lumb (1964) incorporated the effects of cloud type, amount, height, precipitation and fog into a statistical model for the hourly short-wave flux, Q_S, received at the ocean surface. The general form of the relation is

$$Q_S = 135\, f\, s \ (\text{Mw hr cm}^{-2}) \qquad (2.3)$$

where $f = a + bs$ represents the fraction of solar flux transmitted through the atmosphere, s is the mean of the sines of the solar altitude at the beginning and end of the hour, and a and b are constants selected from one of nine categories of atmospheric conditions found to pertain during the hour period. Comparison between the measured values of daily total incident solar flux and those predicted by Lumb's relation show agreement generally to within ±10%. This represents a significant improvement in the estimation of solar flux. For the experimental period, agreement between mean observed and predicted values is within -5% with a standard deviation of ±10%. While the relation favored by Berliand (1960) and used extensively by Budyko (1974), and Wyrtki (1965) yields the same mean error of -5%, the standard deviation is substantially larger (±30%). Thus, the relation due to Lumb is preferred, provided adequate estimates of the cloud type, amount, height and precipitation are available.

Finally, a relation suggested by Seckel and Beaudry (1973) for

estimating clear sky values of the incident flux yielded estimates on average 20% higher than those observed for the 3 days suitable for comparison. Even larger values are obtained if the latitude correction is applied to the basic formulation.

Long-Wave Component

Empirical relations for predicting the net long-wave flux under clear skies from standard meteorological measurements yield values in poor agreement with the present observations. The formulae (Table 2.7) developed by Angstrom (1916), Brunt (1940), Swinbank (1956) and Berliand, Budyko (1956) systematically overestimate the net long-wave flux by 20 to 30 percent. However, a relation due to Anderson (1952) does provide clear-sky estimates which agree to within 10% of observed values. Again, the predicted estimate systematically exceeds the observed value.

To incorporate the effects of clouds in the above formulae a multiplicitive factor of the form $(1-kc^m)$ is frequently used. The constants k and m are empirically determined with m usually set equal to unity; however, Budyko (1956) and Geiger (1961) prefer m = 2. A linear regression analysis applied to the mean daily net long-wave flux as a function of cloud cover yielded a correlation coefficient of 0.88. An intercomparison of the various empirical relations with the measured net long-wave flux for different cloud attenuation factors is provided in Table 2.7.

The quadratic dependence favored by Budyko and most frequently used in conjunction with Berliand's relation is not supported by the data. Discrepancies as large as 100% over the entire experimental period are seen between the directly measured flux and the estimates provided by the various empirical relations.

A linear attenuation factor of the form (1-.85C) provides best

Table 2.7 Comparison of directly measured values of net long-wave flux with estimates predicted by various empirical relations. Both linear and quadratic parameterizations of the atmospheric counter radiation due to clouds are evaluated. All values represent percentage deviations from the measured flux. A positive deviation implies overestimation of the net long-wave flux by the empirical relation. (*) Reed and Halpern (1975) suggest that the stability convection term ($4\sigma\varepsilon T_s^3 (T_s - T_a)$) is not justified based on observations off the Oregon coast. (+) The coefficients (a, b) in the Anderson relation are a function of cloud height while those in the Angstrom relation are not.

Reference	Relation	CF = 1.0 - 0.8C	CF = 1.0 - 0.85C	CF = 1.0 - 0.9C	CF = 1.0 - 0.6C^2
Wyrtki (1965) Kondratyev 1969) *Reed, Halpern (1975)	$Q_{BN} = \sigma\varepsilon T_s^4 (0.39 - 0.05\, e_a^{1/2}) CF + 4\sigma\varepsilon T_s^3 (T_s - T_a)$	15±61	- 2±47	-18±37	96±121
Berliand (1961) Reed, Halpern (1975)	$Q_{BN} = \sigma\varepsilon T_s^4 (0.39 - 0.05\, e_a^{1/2}) CF$	10±51	- 6±39	-23±33	90±111
+Anderson (1952) Tabata (1958)	$Q_{BN} = \sigma\varepsilon (T_s^4 - T_a^4 (a + b\, e_a))$	2±46	-17±35	-32±29	68± 99
+Angström (1916)	$Q_{BN} = \sigma\varepsilon (T_s^4 - T_a^4 (a + b\, e_a)) CF$	17±55	0±42	-18±34	103±119
Brunt (1932) Budyko (1956)	$Q_{BN} = \sigma\varepsilon T_s^4 (1 - a - b\, e_a^{1/2}) CF$	10±51	- 6±39	-23±32	90±111
Swinbank (1956)	$Q_{BN} = \sigma\varepsilon T_s^4 (1 - a\, T_s^2) CF$	25±62	5±46	-13±36	117±113

agreement except for Anderson's formula where (1-. 80C) appears more appropriate. For totally overcast skies Sellers (1965) indicates that low stratus clouds (typical height - 500 meters) might reduce effective outgoing radiation by 95% while cirrus clouds (typical height - 12, 000 meters) would cause only a 16% reduction. A reduction of 80-85% for the observed stratus clouds observed during POLE is consistent with the estimates of Sellers. The high sensitivity of predicted values to slight changes in the empirically determined constant, k, is evident from Table 2. 7. The large standard deviations associated with all the formulae, regardless of cloud factor, indicates such estimates are most appropriate as mean monthly estimates of net long-wave radiation.

In Figure 2. 7A the total daily net long-wave flux estimates by the various empirical relations is shown as a function of cloud cover for a typical mid-ocean atmospheric vapor pressure (15 mb). The adjustable constants used with a given relation were those chosen by their respective originator. The predicted values exhibit largest disagreement for clear skies and converge only for heavy overcast conditions, $0.9 \leq C \leq 1.0$. Wyrtki's formula, however, yields significantly higher estimates for overcast conditions. Angstrom's formula with minimum coefficients departs significantly from the other formula for low values of cloud cover.

The total daily net long-wave flux is shown as a function of atmospheric vapor pressure for a constant cloud cover ($C=0.5$) in Figure 2. 7B. Disagreement between estimates is consistently largest for vapor pressures less than 10 mb, however, with increasing vapor pressure such discrepancies are somewhat reduced. The various parameterizations best converge for vapor pressures in the range $12 \text{ mb} \leq VP \leq 17 \text{ mb}$ except for Wyrtki's and Angstrom's formula (min coefficients) which disagree with the remaining formulae. Fortunately, mid values of vapor pressure correspond well with typical values

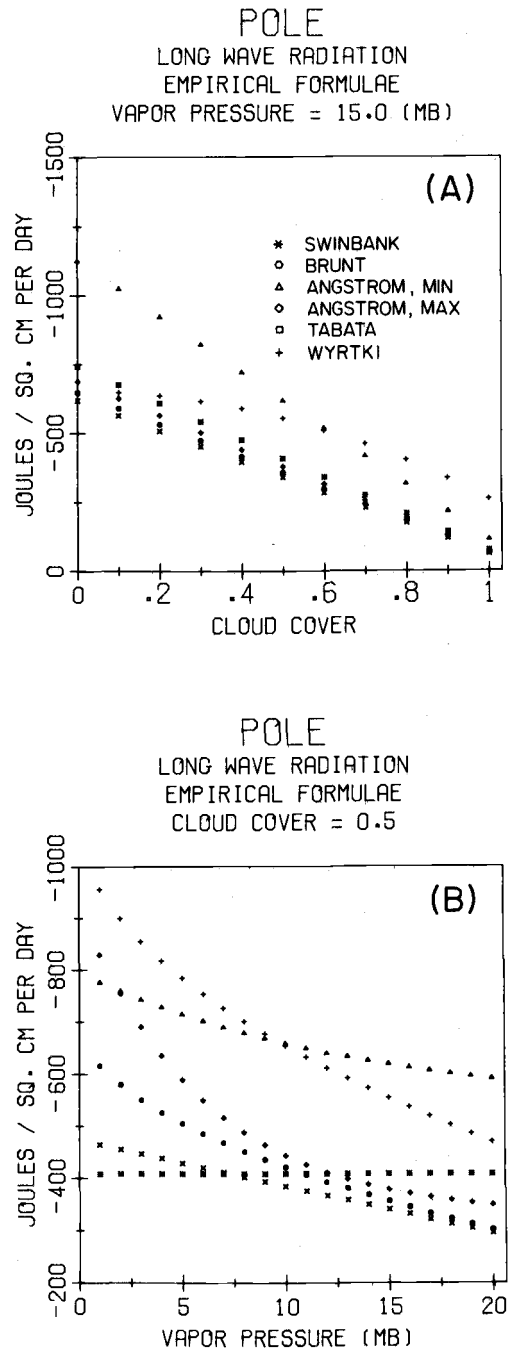

Figure 2.7. Intercomparison of empirical relations predicting the net long-wave flux for specified cloud cover and atmospheric vapor pressure, at a constant sea surface temperature of 14.78° C. The key appearing in Figure 2.7A is applicable throughout.

encountered over the open ocean. Such results suggest terrestial estimates, for which the range of atmospheric vapor pressure may be much larger than over the open ocean, might well yield estimates of the net long-wave radiation more strongly dependent upon the particular parameterization chosen.

Heat Balance Considerations

A significant component of the upper ocean heat balance is the total heat flux at the air-sea interface. The surface fluxes of heat, moisture and radiation most frequently used in heat budget studies are calculated from empirical relations based on observations of bulk meteorological parameters. Comparison of the fluxes of latent and sensible heat with the bulk aerodynamic formulae (Friehe, Schmidt; 1976) suggest that the latent heat flux is adequately parameterized by the bulk formula to within 10% of the direct flux value. Sensible heat transfer appears to be more complex. However, over the open ocean sensible heat transfer is less important than other surface processes and not likely to introduce significant error in the heat balance.

The present study suggests that with careful observations of cloud type, amount, height and precipitation the short-wave flux can be estimated to within 5%±10% of the actual flux value. However, clear sky estimates of the net long-wave flux rely critically upon the particular parameterization chosen. Incorporating the effects of cloud cover (Table 2. 7) clearly indicates the sensitivity of such relations to the cloud parameterization. The data suggest that the frequently used quadratic cloud attenuation factor (Wyrtki, 1965; Roden, 1973) is not justified. Results of Reed and Halpern (1975) support this finding. Use of such a cloud attenuation factor substantially overestimates the magnitude of the net long-wave flux, frequently by as much as 90 to 100 percent. The data also suggest that such empirical relations are highly sensitive to linear attenuation models of the form (1-kC).

Slight variations in the value of k produce substantial changes in the predicted values and again the results are highly dependent upon the particular empirical relation chosen.

For the period 3 February 74 through 13 February 74 average daytime values of 21.88 and -3.70 mwatts /cm^2 were obtained for the net solar and net long-wave fluxes, respectively. A mean nocturnal value for the net long-wave flux for this period is -3.51 mwatts/cm^2. On average the oceanic heat loss at the surface due to net long-wave radiation represents 33% of the heat gain due to the net solar flux.

If the frequently used empirical relations consistently overestimate the net long-wave flux by factors in excess of 50%, as the results of this study suggest, northward heat transports based on these empirical estimates may be too small. This suggestion is in qualitative agreement with results of Vonder Haar and Oort (1973) which suggest on the basis of satellite measurements of radiation that the oceanic transport is larger than previous estimates based on empirical estimates of radiation (e.g. Sellers, 1965).

Summary

Mid-oceanic (35° N, 155° W) observations of the various components of the radiative flux were made from R/P FLIP during the period 2 February 74 through 13 February 74. During the experimental period cloud cover ranged from clear skies to heavy overcast, atmospheric vapor pressure varied from 9 to 18 mb, and the radiometrically measured sea surface temperature fluctuated from 13.9 to 15.3° C. The observational period included four days during which the overlying air was warmer than the sea surface, otherwise the stratification was unstable.

The sea surface albedo was estimated from simultaneous measurements of the incident and reflected solar fluxes. Parametric representation of albedo in terms of solar altitude and atmospheric

transmittance appears valid for solar altitudes greater than 25 degrees. For overcast conditions the sky radiance distribution becomes nearly isotropic and the albedo is 0.06. For clear skies the albedo exhibits a strong functional dependence on solar altitude at low sun angles. Good agreement exists between the values presently reported and those obtained by R. E. Payne from observations over coastal waters, except for conditions of low sun angle. For these conditions the values obtained in the North Pacific are systematically lower than the corresponding coastal values. The variations of albedo with sea surface roughness is also investigated.

Most of the previously reported daytime measurements of the net long-wave flux were obtained indirectly by subtracting simultaneous measurements of the net radiation and the net solar flux. The accuracy of such estimates can be low during the day because the net long-wave flux is frequently an order of magnitude less than the actually measured and differenced quantities. The net long-wave fluxes reported in this paper represent a direct flux measurement. Nocturnal intercomparison of the net long-wave and the net all-wave radiometers yield values which agree on average to within 2%, well within the stated accuracies of either device.

Empirical relations for estimating both the short-wave and long-wave components of the radiative flux are evaluated in the context of the present measurements. A relation due to Lumb for determining the incident solar flux based on standard meteorological observations consistently yields values in good agreement with observations. The formulae available for estimating the net long-wave flux yield poor agreement with observations. Significant error is introduced if the effect of atmospheric counter radiation is modeled in terms of a quadratic dependence on mean cloud cover. Large overestimates of the net long-wave flux by the frequently used empirical relations may lead to heat balance discrepancies of order 50% or larger in the central North Pacific.

III. IRRADIANCE MEASUREMENTS IN THE UPPER OCEAN

Introduction

A knowledge of the distribution of solar radiation in the upper ocean is important for modeling physical, chemical and biological processes. The principal physical application is modeling the heating of the upper layers by absorption of solar radiation. The assumption often used (e. g. Denman, 1973) is that the downward irradiance, and hence approximately the absorption, is an exponential function of depth given by:

$$I = I_o \exp[-x/\zeta] \qquad (3.1)$$

where I, the downard irradiance, is the radiant flux density (energy/unit area/unit time) on a horizontal surface due to contributions from the entire upward hemisphere, I_o is the incident less reflected and emergent irradiance at the surface, z is the vertical space coordinate, positive downward with origin at mean sea level and ζ is the attenuation length. Upward irradiance, due to backscattering, ranges from about 0. 3 to 3% of downward irradiance and is neglected in the present context. We assume that optical properties of the upper ocean are independent of depth: a reasonable approximation in the surface mixed layer.

The assumption of an exponential decay with depth is a poor approximation in the upper 5 meters of the ocean because of the preferential absorption of the short and long wavelength components of sunlight. Below 10 meters depth, however, the assumption of exponential decay is a good approximation because the preferential absorption above has left only blue-green light. These facts concerning the distribution of light in the upper ocean have long been known (Jerlov, 1968), but they have not always been completely taken into account when modeling the upper ocean (e. g. Denman, 1973). Even

if one were only concerned about the distribution of light below 10 m where ζ is approximately constant, (3.1) is a poor approximation because I does not equal I_o when extrapolating up to the surface (ζ varies in the upper 10 meters).

Another aspect of modeling the distribution of solar radiation is the variation of optical characteristics with depth, geographical location and season. Jerlov (1968) has devised a system of classifications of surface water types based on spectral transmittance of downward irradiance at high solar altitude. Jerlov shows variations of water type with geographical location. Observations are lacking in many areas.

The purpose of this Chapter is to describe measurements of downward irradiance made in the upper 40 m of the North Pacific and to support a more accurate parameterization of irradiance than has often been used.

Observations

Observations were made from the R/P FLIP about 800 miles north of Hawaii in the vicinity of 35° N, 155° W during the POLE experiment, a component of the North Pacific Experiment (NORPAX).

The irradiance meter used for the measurements had a uniform spectral response within ±5% for wavelengths from 400 nm to 1000 nm. The sensing surface was flat and remained horizontal and facing upward while suspended from FLIP by an electrical conductor and strain member. The instrument was lowered by hand and measurements were recorded from a meter on deck. Values were recorded at each level both when lowering and raising the instrument. The values at each level were averaged to reduce errors caused by variations of I_o over the period of the run (about 10 minutes). Nevertheless, four out of a total of 10 runs were omitted because of variations in I_o caused by variations in cloudiness. Observations of

Secchi disc depth were usually made during each run.

Because of the characteristics of FLIP it was possible to make measurements of irradiance which were negligibly affected by platform motion or shading of the surface of the superstructure. Vertical motions of FLIP are only about 10 cm amplitude. The measurements were made from a deck extending well away from the hull. Care was taken to avoid measurements when the area below the deck was shaded by the superstructure. The variability in irradiance caused by waves was averaged by eye and the mean value recorded.

A summary of the conditions for each run is given in Table 3.1. The value of I_o was determined by subtracting reflected and emergent radiation from the incident radiation measured by an Eppley pyrheliometer facing upwards. Values of albedo according to Payne (1972) were used to estimate the reflected radiation. The estimated albedo was .06 for all runs except No. 1 which had a value 0.15. Emergent radiation was assumed to be 0.5% of incoming (Payne, 1972).

The observations of irradiance in the water were corrected for the immersion effect (see e.g. Westlake, 1965). The immersion effect is the difference in the response of the irradiance meter in water from that in air. Correction for the effect was determined from measurements in the laboratory and can be expressed as

$$I/I_o = 1.18\, I_m/I_{am}$$

where I_m and I_{am} are the measured downward irradiances in water and air respectively. The difference in reflectivities of the plane water surface in the laboratory and the rough surface characteristics of the field observations was taken into account. The coefficient in the above expression for Run No. 1 is 1.31 rather than 1.18 because of the higher reflectivity of the water surface during that run.

Table 3.1 Irradiance measurements during the POLE experiment. ζ_2 is the attenuation length calculated between 10 and 40 m depth.

Run no.	Date (Feb)	Time (local)	Sun Alt. (deg.)	I_o (mw/cm^2	Cloud (tenths)	Wind (m/sec)	Secchi depth (m)	ζ_2 (m)
1	7	1625	16	32.7	0	3.5	23	16
4	10	1129	38	7.2	10	3	26	20
5	10	1501	30	18.3	10	5	24	19
6	11	1500	30	26.4	10	3	24	20
9	13	1112	38	23.3	10	12	--	16
10	13	1436	34	26.3	10	13	18	21
							Ave.	19

Analysis and Discussion

The observations from each of the six runs are plotted in Figure 3. 1. As expected, there is strong attenuation near the surface because of the dependence on wavelength. Below 10 m depth, however, the decay is nearly exponential. Values of the attenuation length over 10 to 40 m depth were determined for each run by a least squares fit of (3. 1) to the observations below 10 m. These values (ζ_2) are given in Table 3. 1.

The observations of Run No. 1 show a significantly larger attenuation with depth than the remaining runs, particularly near the surface. This can be explained by reference to Table 3. 1 where it is seen that the sky was cloudless and the altitude of the sun was only 16° for Run No. 1 compared with overcast skies and a minimum solar altitude of 30° for the remaining runs. The combination of low sun angle and clear sky causes more rapid attenuation with depth because the path of the sun's rays is far from vertical.

A composite of the observations excepting Run No. 1 was formed by averaging I/I_o for each depth. A plot of the composite is shown in Figure 3. 2 together with a plot of Run No. 1. A least squares fit below 10 m depth of

$$I/I_o = (1-R)\exp[-z/\zeta_2] \tag{3. 2}$$

to the composite observations and to Run No. 1 yielded values of R and ζ_2. I/I_o, computed from (3. 2) with the determined values of R and ζ_2, was then subtracted from the observations above 6 m. A second least squares fit of

$$I/I_o - (1-R)\exp[-z/\zeta_2] = R\exp[-z/\zeta_1] \tag{3. 3}$$

to the differenced observations [left side of (3. 3)] over 0 to 6 m depth yielded an estimate of ζ_1 with R and ζ_2 specified from the previous fit. The combined expression obtained by rewriting (3. 3) is

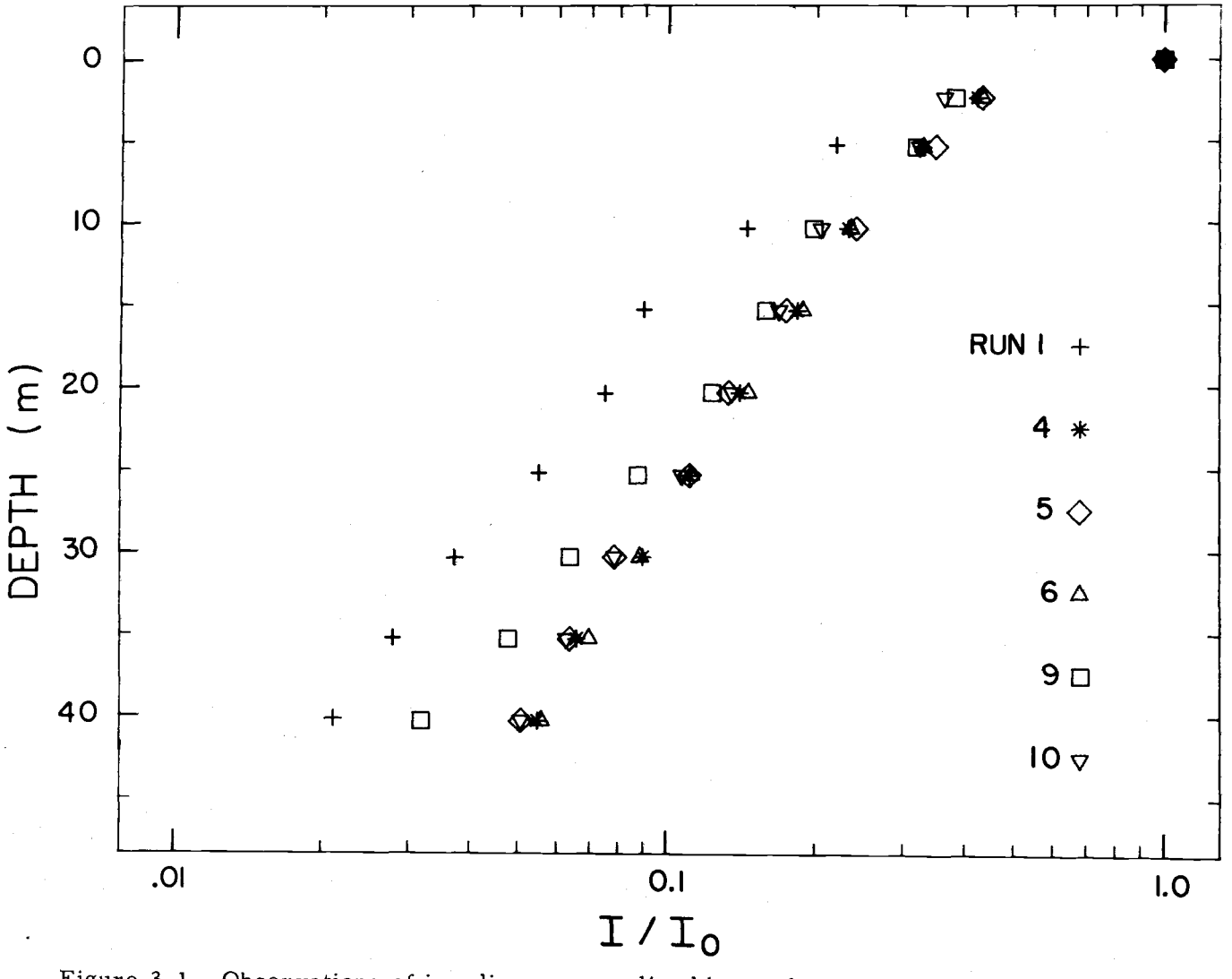

Figure 3. 1 Observations of irradiance normalized by surface values as a function of depth. The conditions for each run are given by Table 3. 1.

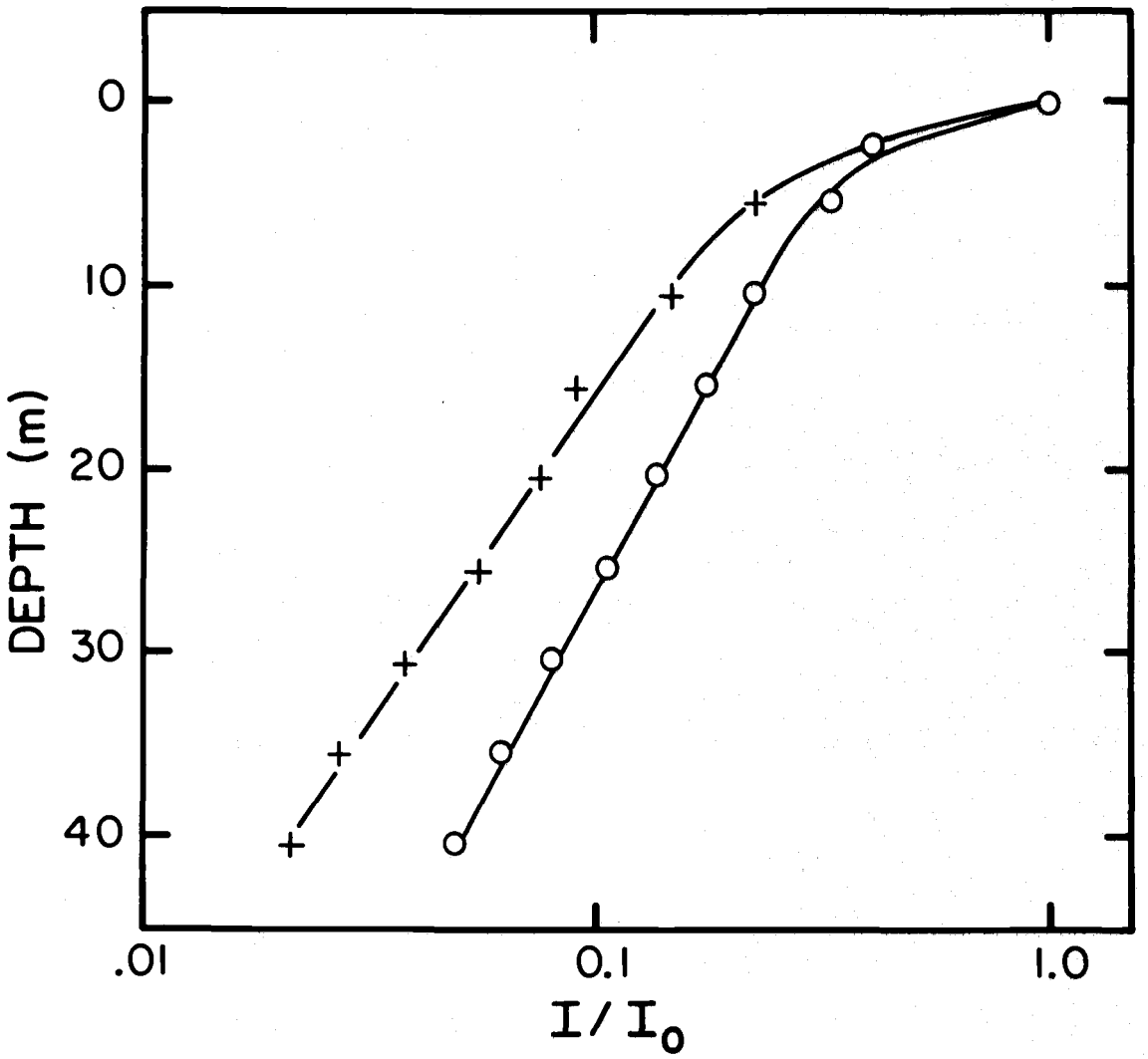

Figure 3.2. Averaged observations of normalized irradiance (except Run No. 1) vs. depth (circles) and a similar plot of Run No. 1 (crosses). The curves are from Equation 4 with parameters given in Table 3.2.

$$I/I_o = R \exp[-z/\zeta_1] + (1-R) \exp[-z/\zeta_2] \qquad (3.4)$$

Values for R, ζ_1 and ζ_2 for Run No. 1 and the composite observations are given in Table 3.2. The curves plotted in Figure 3.2 are computed from (3.4) with the best-fit parameters. The first exponential term of (3.4) characterizes the rapid attenuation in the upper 5 m due to absorption in the red end of the spectrum. The second exponential represents the attenuation of blue-green light which remained monochromatic below 10 m.

An expression identical in form to (4) was previously suggested by Kraus (1972, p. 92) as approximation to the irradiance field. Kraus suggested values of R, ζ_1 and ζ_2 of 0.4, 5 m and 40 m respectively for very clear ocean water based on observations in Crater Lake, which is among the clearest of natural water bodies. Comparison with the other estimates of R in Table 3.2 suggests that R = 0.4 may be too small.

Jerlov (1968) has proposed a scheme for classifying oceanic water according to its clarity. He defines 5 types: I, IA, IB, II and III, ranging from clear to dirtier water. We have determined best-fitting parameters by the method used above for each set of irradiance values (Jerlov, 1968, Table XXI) corresponding to different water types. The parameters are given in Table 3.2 and are determined from a fit to the data in the upper 100 m (neglecting the 10 m value) except for Type I where a set of parameters was also determined for the upper 50 m because of a change in slope of ln I vs. z below 50 m. A comparison of the parameters for the composite observations with the parameters for Type IA shows remarkable similarity, suggesting that the upper ocean during the POLE experiment can be classified IA. The lack of agreement between ζ_1 for the two cases is not critical because of inaccuracies in the representation (3.4) in the upper 5 m.

Table 3.2 Values of parameters determined by fitting the sum of two exponentials to observations of downward irradiance: $I/I_o = R \exp[-z\,\zeta_1] + (1-4)\exp[-z/\zeta_2]$.

	R	ζ_1(m)	ζ_2(m)
Run No. 1	0.74	1.7	16
Composite observations (Runs 4, 5, 6, 9 and 10)	0.62	1.5	20
Kraus (1972) - very clear water	0.4	5	40
Jerlov (1968) - Type I	0.58	0.35	23
- Type I (upper 50 m)	0.68	1.2	28
- Type IA	0.62	0.60	20
- Type IB	0.67	1.0	17
- Type II	0.77	1.5	14
- Type III	0.78	1.4	7.9

A comparison between the representation (3.4) and Jerlov's Table XXI is shown in Figure 3.3. As would be expected, the fit is least accurate in the upper 10 m. The fit at 10 m could be improved by including the value at 10 m in the determination of R and ζ_2. The values of I vs. depth below mean sea level in the upper 5 m will be affected by the magnitude of the waves because of the nonlinear relation between I and depth.

It is, of course, possible to devise more complicated and perhaps more realistic expressions than (3.4) for the irradiance as a function of depth by including additional exponential terms and explicitly accounting for solar altitude and refraction. This has been done in studies of lakes (e.g. Jassby and Powell, 1975). Even through crude, (3.4) is a significant improvement over (3.1) and is likely to be a satisfactory approximation for many applications.

Observations of Secchi disc depth (Table 3.1) were made simultaneous to all of the runs reported except one. The observations are remarkably consistent except for Run No. 10. The mean of the first four runs is 24±1 m while Run No. 10 has a Secchi depth of 18 m. The reason for the lower value is likely because of the higher winds during Run 10, 13 m/sec compared to a maximum of 5 m/sec for the remaining runs. The higher winds increase the roughness and motion of the surface which tends to fragment the image of the disc and decrease its visibility. Neglecting Run No. 10, the Secchi disc depth appears to be a consistent indicator of optical characteristics, assuming the variation in characteristics over the series of observations was small.

The Secchi disc depths are plotted in Figure 3.4 vs. the depth at which the irradiance falls to 10% of its surface value. The drawing of a line in Figure 3.4 with a slope of one is motivated by a relationship suggested by Tyler (1968):

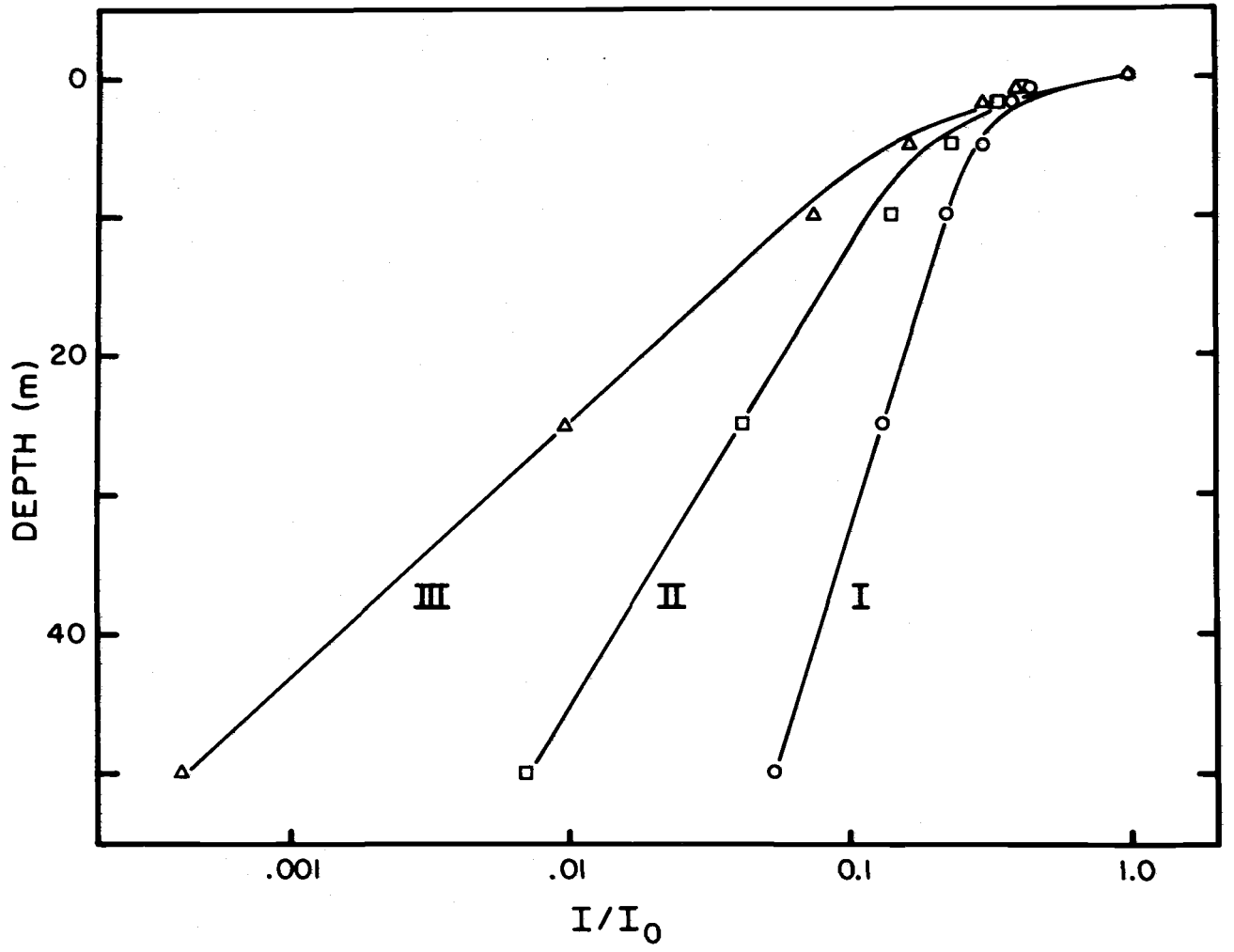

Figure 3. 3 Values of irradiance from Jerlov's (1968) Table XXI for water types I, II and III. The curves are a plot of Equation (4) with parameters given in Table 3. 2. The parameters are from a fit to values in the table for the upper 100 m except type I where parameters for the upper 50 m are used.

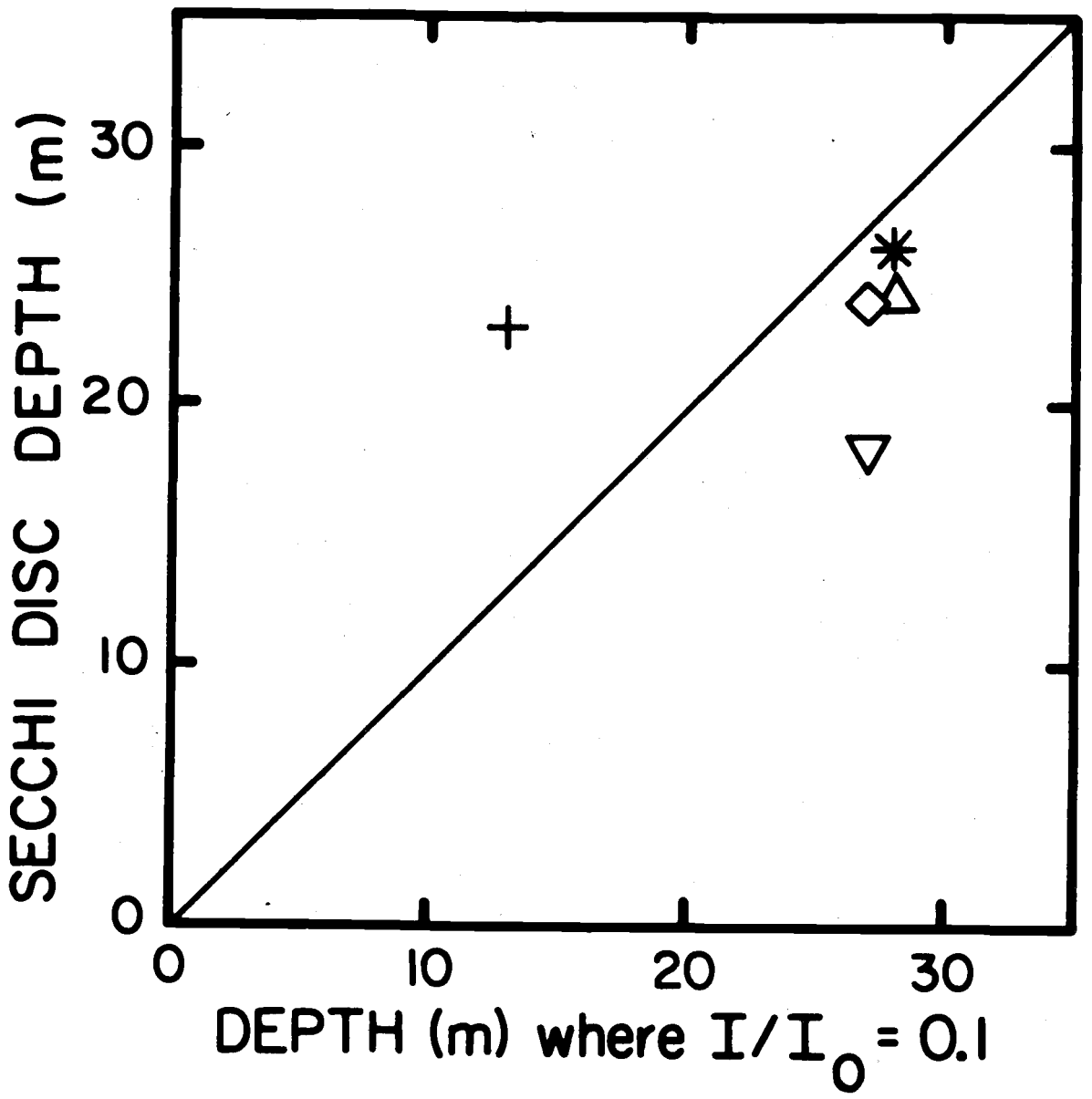

Figure 3.4 Observations of Secchi disc depth vs. depth at which I/I_o equals 0.1. The symbols correspond to Run numbers identified in Figure 3.1.

$$\frac{3.78K}{(\alpha+K)} = \frac{Z_{SD}}{I_{0.1}} \qquad (3.5)$$

where α and K are the attenuation coefficients for collimated and diffuse light respectively, Z_{SD} is the Secchi disc depth and $I_{0.1}$ is the depth at which I falls to 10% of the surface value. Eq. (3.5) is consistent with the line of slope one in Figure 3.4 if $\alpha = 2.78K$, a value close to that observed in a clear lake (Smith et al., 1973). Caution should be exercised in interpretation of Figure 3.4. As pointed out by Tyler (1968), α is not necessarily a fixed multiple of K and other assumptions are made in the deviation of (3.5). The data presented in Figure 3.4 are by themselves inadequate for a critical test of (3.5). More extensive observations over a wide range of optical properties are required. The scatter in a plot similar to Figure 3.4 presented by Tyler (1968) encourages doubt in the validity of (3.5).

Although crude, observations of Secchi disc depth are economical and are often all that is available to characterize the optical properties of the upper ocean. The historical record of Secchi disc observations far outweighs that of less ambiguous optical measurements. Frederick (1970) has compiled an atlas of Secchi observations which shows variation in Secchi depth over the world oceans of remarkable detail. Atlases of this sort would be very useful to modelers if the relationships between Secchi depth and other optical properties could be improved.

Summary

Observations were made of downward solar radiation as a function of depth during an experiment in the North Pacific (35° N, 155° W). The irradiance meter employed was sensitive to solar radiation of wavelength 400 to 1000 nm arriving from above at a horizontal

surface. Because of selective absorption of the short and long wavelengths, the irradiance decreases much faster than exponential in the upper few meters, falling to one-third of the incident value between two and three meters depth. Below 10 meters, the decrease was exponential at a rate characteristic of moderately clear water of Type IA. Neglecting one case having low sun altitude, the observations are well represented by the expression

$$I/I_o = R \exp[-z/\zeta_1] + (1-R) \exp[-z/\zeta_2]$$

where I is the irradiance at depth -z, I_o is the irradiance at the surface less reflected solar radiation, R equals 0.62, ζ_1 and ζ_2 are attenuation lengths equal to 1.5 and 20 m respectively. The depth at which the irradiance falls to 10% of its surface value is nearly the same as observations of Secchi depth when cases with high wind speed or low solar altitude are neglected. Parameters R, ζ_1, and ζ_2 are computed for the entire range of oceanic water types.

IV. UPPER OCEAN STRUCTURE: TEMPORAL VARIATIONS IN THE CENTRAL NORTH PACIFIC

Introduction

Temporal variations in the structure of the upper ocean are caused by the exchange of energy, momentum and mass across the air-sea interface. The development of the surface well-mixed layer often is regarded as a locally generated and vertically propagated process. The depth of the mixed layer is modeled as a combination of forced and free convective processes. Forced convection is caused by the wind stress acting on the surface. Free convection results from gravitational instability caused by cooling and evaporation of the sea surface.

Wind generated inertial oscillations within the well-mixed layer are suggested by Pollard, Rhines and Thompson (PRT, 1973) as a factor responsible for deepening the mixed layer. Their mechanism envisages the generation of turbulent energy at the base of the mixed layer which is used to entrain fluid from the stably stratified region below. The mechanism is active on time scales of less than a half pendulum day. Kraus and Turner (1967) and Denman (1973) (KTD) emphasize wind-induced surface stirring as the mechanism in supplying mechanical energy for deepening and maintaining the well-mixed surface layer. The KTD mechanism is effective on a time scale greater than a few days. Niiler (1975) incorporated both mechanisms in a three-layer model of upper ocean dynamics. The surface production rate ($\vec{\tau}_o U_o$) employed by KTD is found to dominate for both small ($t < N^{-1}$) and large ($t > f^{-1}$) time scales, where N and f are the Vaisala frequency of the ocean below the well-mixed layer and the inertial frequency respectively.

To better understand upper ocean processes and evaluate existing parameterizations of such processes, the POLE experiment, a component of the North Pacific Experiment (NORPAX) was conducted during the period 28 January 74 through 14 February 74. The

experimental site (near 35° N, 155° W) is hydrodynamically complex as shown in Figure 4. 1. The Subtropical Front is known to meander between 32° and 35° N. lat. (Roden, 1973; Barnett, 1976). The region of the Trade Winds northeast of the Hawaiian Island Chain has fluxes of latent heat in excess of 850 joules cm^{-2} day^{-1} (Wyrtki, 1965). The Subtropical Water Mass formed in this region contrasts markedly with the less saline Eastern North Pacific Central Water characteristically encountered north of 35° N lat. The Horse Latitudes are located only 3° of latitude to the south of the observational area and the North Pacific Current is expected to affect the general hydrography of the region.

Observations

Vertical profiles of temperature and salinity were taken from R/P FLIP throughout the period 30 January through 14 February 1974. During the experiment, FLIP occupied a station approximately 800 miles north of the Hawaiian Island Chain under free drift conditions. The position of FLIP ranged from 35° 39' to 34° 36'N. latitude and 155° 05' to 155° 25' W. longitude. Profiling was concentrated in the mixed layer and thermocline. The maximum depth reached was 325 meters. On average, 8 profiles were measured per day. On occasion, more intensive sampling was maintained.

In addition to temperature and salinity profiles, measurements of atmospheric and oceanic radiation, sea surface temperature, wind speed, air temperature and humidity were made. Details of the atmospheric radiative fluxes can be found in Chapter II while attenuation of solar flux is discussed in Chapter III. Standard cup anemometers were used to measure wind speed while a Barnes PRT-5 radiation thermometer monitored the sea surface temperature. Hourly values of observed and derived quantities are shown in Figure 4. 2. The hourly values were obtained by interpolating between observations by

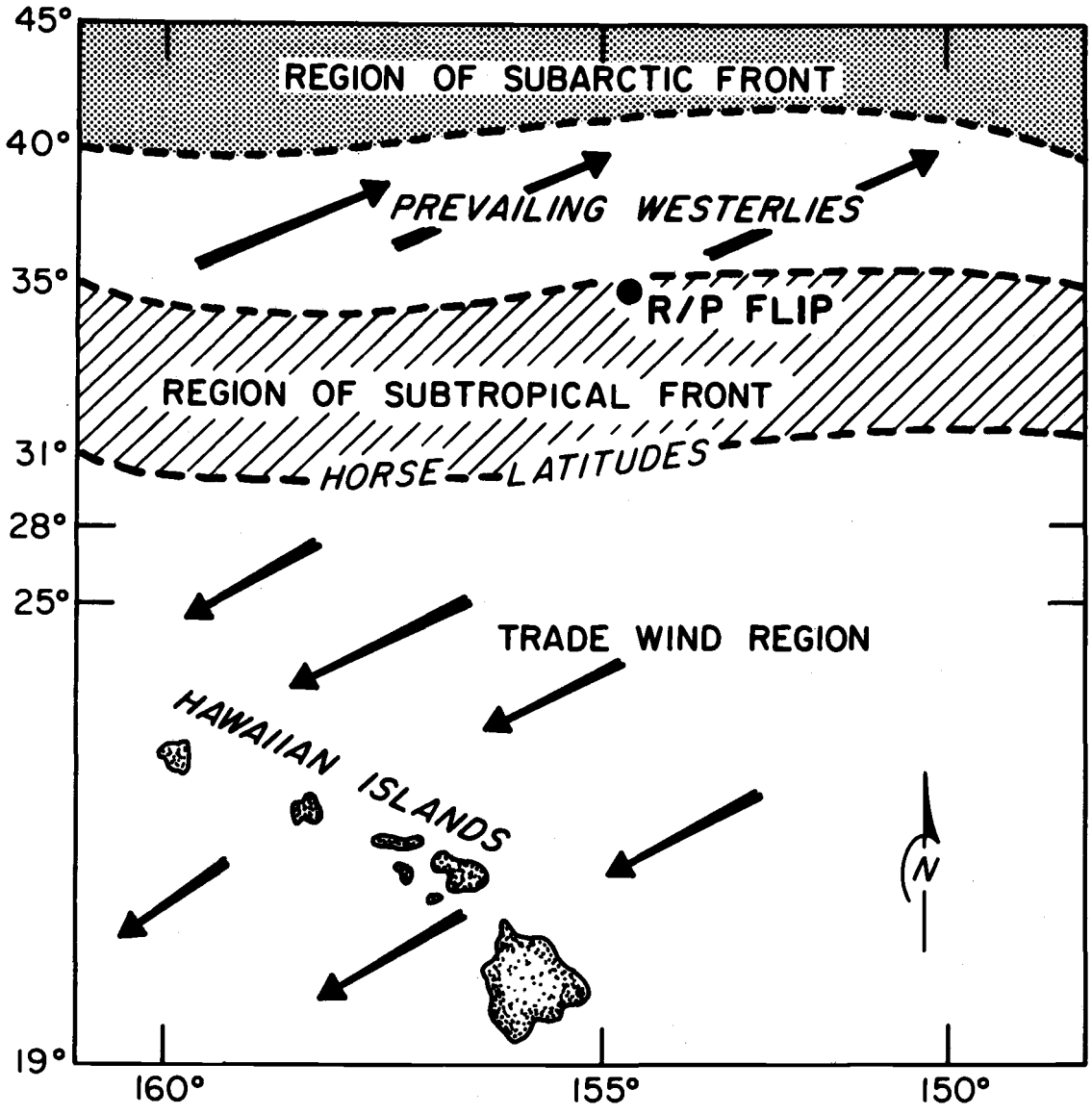

Figure 4.1 The location of the R/P FLIP during the POLE experiment (35° N, 155° W) in relation to general oceanic features.

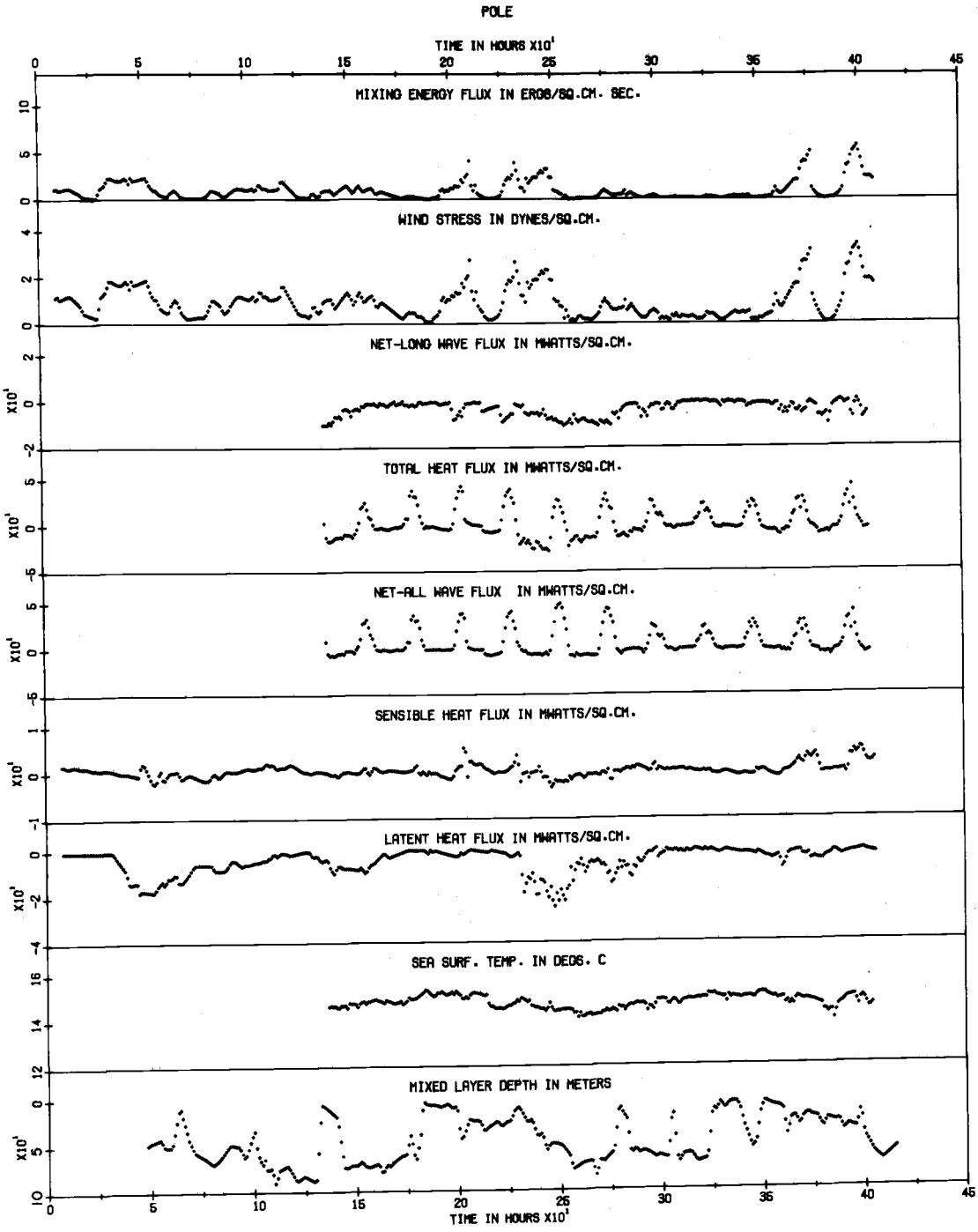

Figure 4. 2 Interpolated hourly values of the various components of the surface momentum and heat balance are shown.

use of a spline under tension.

Instrumentation and Corrections

A Bissett-Berman Model 9040 Salinity/Temperature/Depth (STD) Measuring System was employed as the profiling device. Temperature is determined with a platinum resistance thermometer whose time constant is 0.35 seconds. Salinity is determined from simultaneous measurements of conductivity, temperature and depth. The time response of the conductivity probe is 10 milliseconds. Unfortunately, conductivity is not the recorded variable. Rather, the instrument internally compensates for the effects of temperature and pressure and gives a direct estimate of salinity. Accuracies for depth, temperature and salinity are 1 meter, 0.01° C and 0.03‰ with corresponding resolutions of 0.2 meters, 0.005° C and 0.01‰. Data was recorded in digital form with a sampling rate of 5 per second.

Temperature was standardized against a Mueller platinum resistance bridge. Values presently reported are based on the 1968 temperature scale. Salinity was standardized with reference to surface samples taken during each profile. A Bissett-Berman model 6230 inductive salinometer was used to determine the salinity of the surface samples. This device can accurately resolve salinity to within 0.03‰.

A d.c. correction was applied to the depth signal to eliminate the effect of ambient atmospheric pressure. Corrections due to vertical platform motion were unnecessary as the amplitude of FLIP's vertical oscillations is typically 10 cm.

Spectral analysis of GATE Scale-B data, taken with Bissett-Berman model 9040 STDs, suggested a large percentage of the variance associated with the pressure signal was contributed at frequencies greater than 0.67 Hz. This variance is thought to be internal system noise (Elliot, 1975). The GATE results suggested a low-pass filter is

required to attenuate signals above 0.67 Hz. A two-stage running mean filter designed by J. Z. Holland (1968) was employed.

Differences in the time constants of the temperature and salinity sensors introduce errors in the observed values of temperature and salinity. To correct the temperature signal for thermal inertia of the sensor, a local temperature gradient was calculated from a 12 point non-centered linear regression. The center of regression is 0.3 seconds ahead of the point to be corrected. The corrected temperature, T_c, is then given in terms of the uncorrected temperature, T_o

$$T_c = T_o + \gamma \frac{\Delta T_o}{\Delta t} \tag{4.1}$$

where γ is the response time of the temperature sensor.

The salinity correction is based on a relation (Mosetti, 1967) between the conductivity, C, and the measured temperature and salinity, T_o and S_o.

$$C = (\gamma + \mu T_o^{\,k}) S_o^{\,h} \tag{4.2}$$

where $\gamma = 1.17013$, $\mu = 0.03299$, $k = 1.05257$ and $h = 1.10807$. As this relation is assumed to hold for both corrected and measured values the correction factor assumes the form

$$\lambda = \left[\frac{\gamma + \mu T_o^{\,k}}{\gamma + \mu T_c^{\,k}} \right]^{-h} \tag{4.3}$$

The corrected salinity, S_c, specified in terms of the observed salinity, S_o, then assumes the form

$$S_c = S_o * ((\lambda - 1.) * SF + 1.) \tag{4.4}$$

This relation reduces to the correction used by Elliott for the case

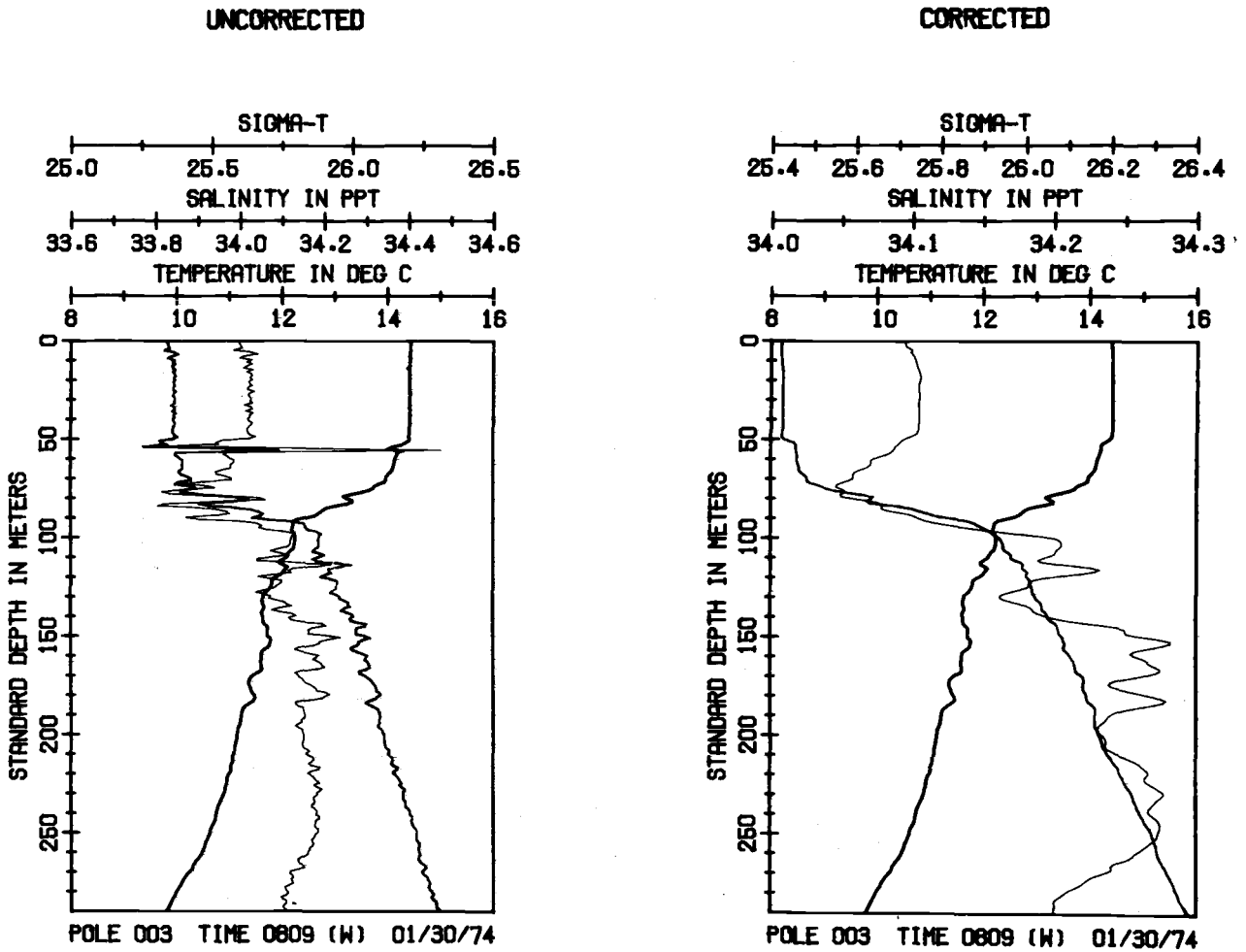

Figure 4.3 Examples of corrected and uncorrected temperature, salinity and density profiles. Corrections were made for the difference in time response of the conductivity and temperature sensors.

SF = 1. The factor SF was introduced to minimize the cumulative magnitude of the inversions in the density profiles determined from corrected values, T_c and S_c. Observations of density inversions are most likely introduced by erroneous salinity measurements made in the presence of sharp temperature gradients. The corrected salinity is then low-pass filtered analogous to pressure. Numerous numerical experiments indicate observed density inversions can be minimized with SF = 6. The resulting triplets (T_c,S_c,D) are then averaged over 1 meter intervals and standard depth values are computed by interpolation from the averaged data sets. The sigma-t profiles were computed using a series expansion in terms of the corrected temperature and salinity (Fofonoff, 1958). In Figure 4. 3, uncorrected and corrected profiles of temperature, salinity and sigma-t are shown for a typical observation.

Surface Conditions

Surface Wind Stress

The observational periods are characterized by low wind speeds. The wind stress calculated under the bulk approximation with a drag coefficient of 1.4×10^{-3} has a mean value of 0.66 dynes cm^{-2} for the experimental period. For periods up to as long as 4 days the stress is considerably less than 1 dyne cm^{-2}. From Figure 4. 2, it is evident that only two periods of relatively high winds were encountered during the experiment; one near the center of the experiment with a maximum wind stress of 2. 7 dynes cm^{-2} and the other at the end of the experiment with a maximum wind stress of 3. 3 dynes cm^{-2}.

The Kraus-Turner (1967) mixing energy hypothesis suggests that the turbulent energy available for entrainment (increasing the potential energy P of the water column) is produced at a rate that is some constant fraction m of the downward transfer of turbulent energy from the wind, i. e. ,

$$\frac{dP}{dt} = m\rho_a C_D \overline{U}_{10}^3 \qquad (4.5)$$

where ρ_a is the density of air, C_D is the drag coefficient, and $\overline{U}_{10}$ is the mean wind speed at a height of 10 meters. To compute the mixing energy flux, shown in Figure 4.2, a value of m = 0.0012 (Denman, 1973) was used.

Surface Heat Fluxes

The net all-wave and net long-wave radiative fluxes were measured with a Swissteco Pty. Ltd. net radiometer M S-1 and a Middleton Instruments net long-wave radiometer, respectively. (Details can be found in Chapter II.) The latent and sensible heat fluxes were determined from standard meteorological observations using the bulk approximations with a drag coefficients of 1.4×10^{-3}. The observations, together with the total heat flux and the radiometrically measured sea surface temperature, were fit with a spline under tension to yield hourly values of the various components of the surface heat flux. The results appear in Figure 4.2.

The net all-wave flux is generally the dominant term in the surface heat balance. However, a two day period of enhanced latent heat flux, due largely to a significant increase in wind speed midway through the experiment, is evident. The sensible heat flux never exceeded ±2.0 milliwatts cm^{-2} and typically was less than ±1.0 milliwatts cm^{-2}. Friehe and Schmitt (1974) computed average values of the latent and sensible heat fluxes for the 17 days of observations. They found the sensible heat flux two orders of magnitude less than the latent heat flux for the observational period. The average Bowen ratio was +0.013, substantially smaller than the commonly used value of +0.1. Diurnal variations in the sensible heat flux are not as evident as might be expected. This may in part be due to the anomolous

condition, ocean colder than atmosphere, intermittently observed, throughout the experiment, i. e. the boundary layer was both stably and unstably stratified, undoubtedly affecting the sensible heat transfer.

A daily heat budget is provided in Table 4. 1. In this context heat gain by the ocean is defined positive. Daily flux values were calculated as a centered average about local solar noon (time zone W). The heat budget results indicate the ocean gained heat (on average 323 joules cm^{-2} day^{-1}) for 6 days, was in near thermal equilibrium with the atmosphere for 2 days and lost heat to the atmosphere for the 2 day period during which the turbulent heat fluxes (on average -484 joules cm^{-2} day^{-1}) dominated the local heat budget at the surface. The total heat budget for the experiment suggests the ocean gained 843 joules cm^{-2} during the 10 complete days of radiative flux observations. If partial days at the beginning and end of this period are included the ocean gained 1036 joules cm^{-2}. These results, coupled with the low wind stresses, imply upper ocean dynamics might have been dominated by net surface heating for a significant part of the experiment.

Mass and Buoyancy Fluxes

The net mass flux at the surface represents the combined effects of evaporation (a loss) and precipitation (a gain). A period of precipitation is evident in Figure 4. 4. During this period an average of 5×10^{-5} grams cm^{-2} sec^{-1} of rain fell on the ocean. During periods of intense evaporation, mass fluxes of order -9×10^{-5} grams cm^{-2} sec^{-1} were measured. A background level of 0. 1 to 1. 0 μgrams cm^{-2} sec^{-1} loss or gain was typical for the observational period. Overall, evaporation and precipitation were in near-equilibrium, precipitation exceeding evaporation by 23 milligrams cm^{-2}.

Table 4.1 Daily heat flux budgets for the POLE experiment computed symmetrically about local solar noon. All units are in joules cm^{-2} day^{-1}. Heat gain by the ocean is assumed positive. Initial time is 0000 hours on 28 January 74.

Date	Time (noon)	Total heat flux	Radiative heat flux	Turbulent heat flux
3 Feb 74	156	- 90.0	444.5	- 533.5
4 Feb 74	180	548.1	608.2	- 60.1
5 Feb 74	204	515.6	566.7	- 51.2
6 Feb 74	228	- 37.4	449.2	- 486.6
7 Feb 74	252	-768.0	657.9	-1425.9
8 Feb 74	276	-199.9	542.1	- 741.9
9 Feb 74	300	186.9	346.2	- 159.3
10 Feb 74	324	283.2	376.9	- 93.7
11 Feb 74	348	208.9	490.4	- 281.4
12 Feb 74	372	196.1	388.6	- 192.5

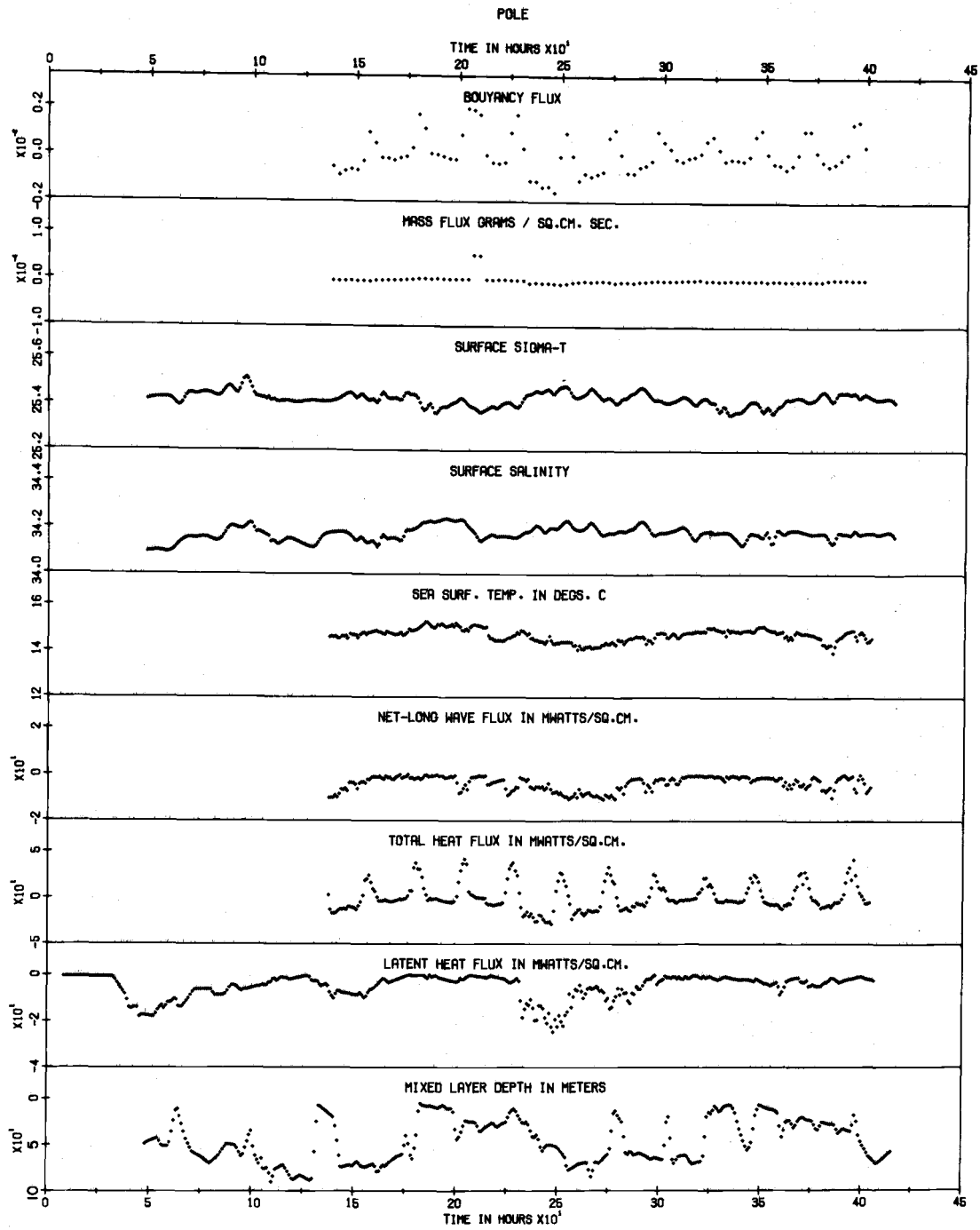

Figure 4.4 Interpolated hourly values of mass and buoyancy fluxes, surface salinity, sea surface temperature, surface sigma-t, and the various components of the heat flux involved in the determination of the buoyancy flux.

Stratification in the ocean exerts a strong dynamical influence on mixing since a stably stratified fluid requires work against buoyancy forces if mixing is to occur. The rate of ptoential energy change per unit mass is given by

$$M = \frac{-g}{\rho} \overline{\rho' w'} \tag{4.6}$$

For a stably stratified fluid the density increases with depth and the buoyancy force is directed upward, while the converse is true for an unstably stratified fluid. At the surface the buoyancy flux, M_o, is determined by air-sea transfers (Monin, 1972).

$$M_o = \frac{g}{\rho} \left[B c_p^{-1} (Q_{NA} + Q_T) + 10^{-3} S (R+E) \right] \tag{4.7}$$

where g is the acceleration due to gravity, ρ the density of seawater, B is the thermal coefficient of expansion of seawater, c_p is the specific heat of seawater, S is the surface salinity and E and R are the rates of evaporation and precipitation, respectively. The turbulent flux, Q_T, represents the sum of latent and sensible heat fluxes while the net all-wave radiative flux is given by Q_{NA}. The gain of heat or mass by the ocean is defined positive. Figure 4.4 suggests that the mass flux had little influence on the buoyancy flux except possibly during the one period of precipitation. Rather, the net heat flux dominates the surface values of buoyancy flux. During daytime periods, positive buoyancy flux results from the dominant role of solar heating at the surface while during evening periods a negative buoyancy flux is produced by the combined effects of net long-wave radiation and the turbulent fluxes of heat and moisture.

The Well-Mixed Layer

Profiles of temperature and sigma-t for the entire duration of the experiment are shown in Figures 4.5 and 4.6, respectively.

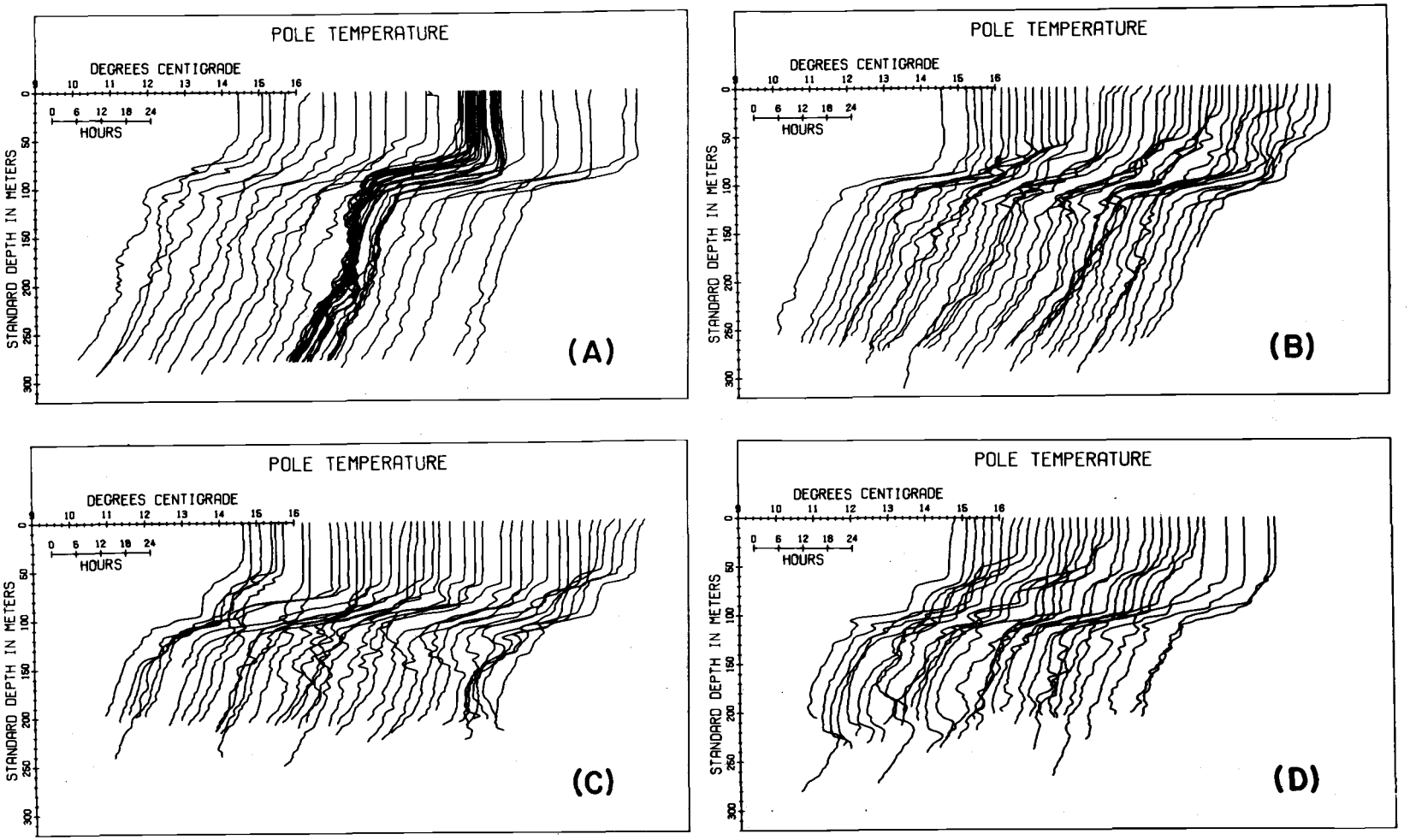

Figure 4.5 Profiles of temperature for the entire experimental period. The spacing between adjacent profiles is proportional to the real-time between hydrocasts.

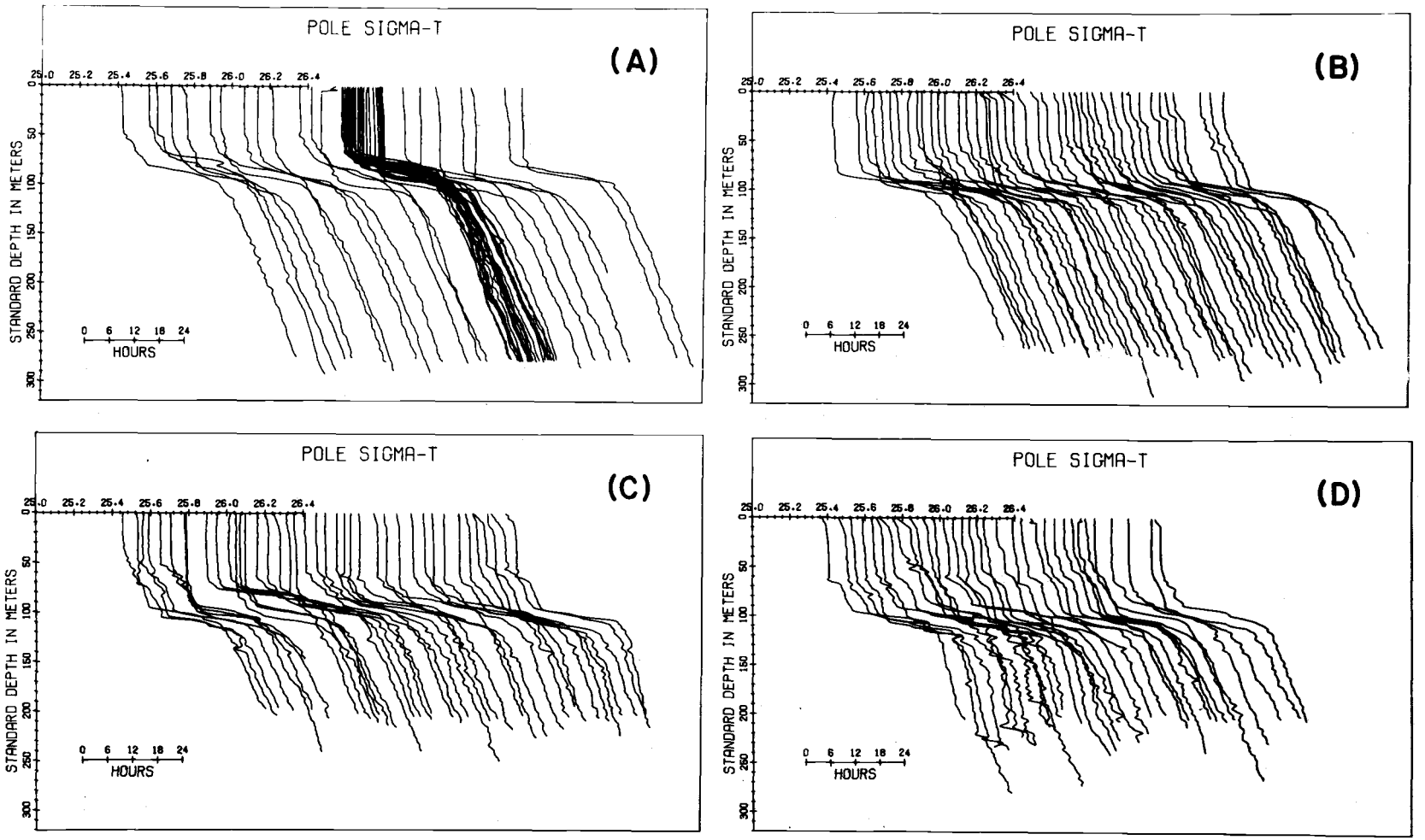

Figure 4.6 Profiles of sigma-t for the observation period 30 Jan 74 through 14 Feb. 74. The spacing between adjacent profiles is proportional to the real-time between observations.

The spacing between adjacent profiles is proportional to the time interval between measurements. The seasonal thermocline is clearly evident at a depth of approximately 100 meters. However, for large periods of time the layer above the seasonal thermocline is far from uniform. Temperature inversions are frequently seen at the base of the mixed layer. Step-like structures and multiple mixed layers, formed during periods of low winds and net heat gains at the surface of the ocean, frequently appear above the seasonal thermocline. During periods of high winds these structures are eroded quickly. Comparison of the temperature and sigma-t profiles indicates the dominant role of temperature in establishment of the density structure above 250 meters. The possibility of vertically propagating internal waves is evident in the closely sampled temperature profiles near the beginning of the experiment.

Contours of temperature, salinity and sigma-t for the observational period are shown in Figures 4.7A, 4.7B, and 4.8, respectively. The scale at the base of these plots indicates the time at which a given observation was made. Upon comparison with the wind distribution of Figure 4.2, it is evident that the isotherms and isopycnals between 50 and 80 meters converge during periods of high winds. This feature is noticeably absent from the isohaline contours. This suggests that the temporal variations in the density structure of the upper 100 meters primarily are due to thermal processes. During periods of calm winds a light warm surface layer, corresponding to a 25.4 isopycnal, forms rapidly. Thus, for part of the observational period the ocean gained heat due to surface processes, acting on diurnal time scales or longer, and intermittently took on some of the characteristics of a summertime well-mixed layer. These observations are consistent with those of Barnett (1976) who found that the total heat content down to a depth of 300 meters along a 170° W. long. section at approximately 30° N. lat. was slightly greater in February than

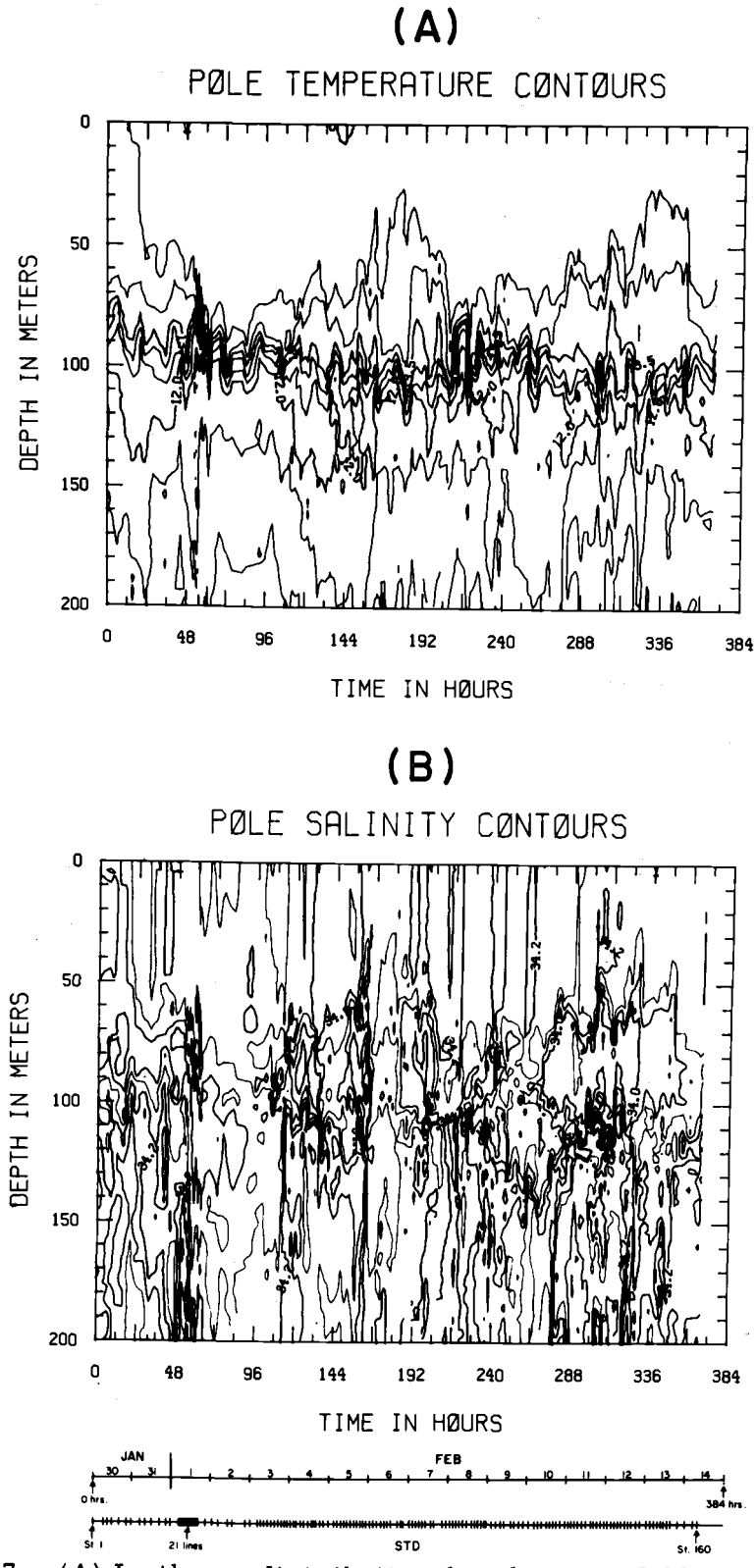

Figure 4.7 (A) Isotherm distribution for the period 30 Jan 74 through 14 Feb 74. The scale at the bottom of the figure indicates the STD profiling times. The contour interval is 0.5° C. (B) Isohaline distribution for the period 30 Jan 74 through 14 Feb 74. The contour interval is 0.05‰.

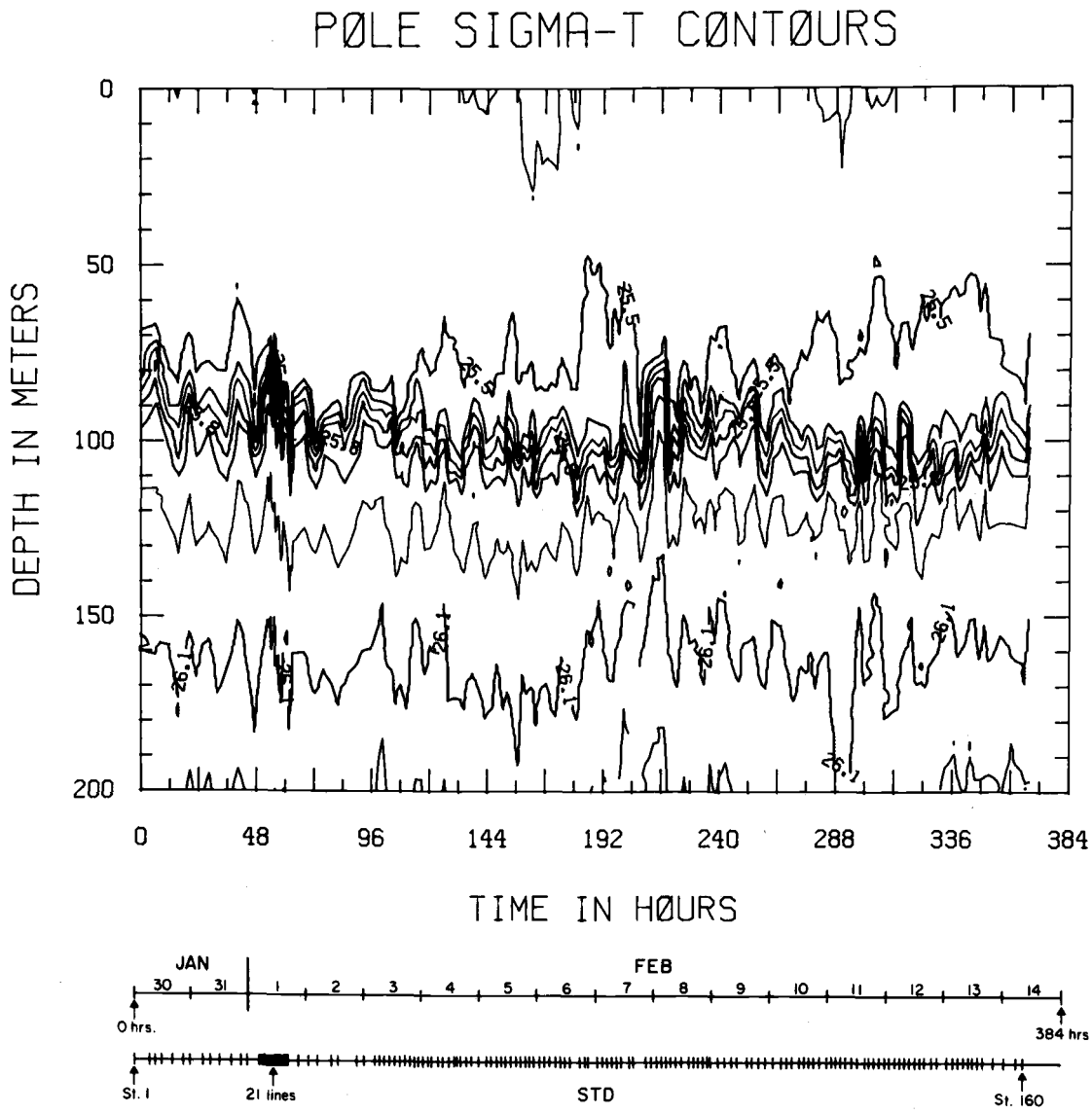

Figure 4.8 The isopycnal distribution during POLE. The contour interval is 0.1‰.

in January.

The well-mixed layer usually consists of the upper 10 to 100 meters of the ocean, is characterized by near-uniform density structure, and responds directly to atmospheric forcing on time scales of longer than an hour. The mixed layer depth (Figure 4. 2) is defined as the shallowest depth at which the temperature is not more than 0. 05° C less than the temperature at a depth of 5 meters. A similar definition based on the observed density structure yielded substantially the same mixed layer depth. Diurnal variations in mixed-layer depth resulting from local surface processes are often present. The low wind conditions encountered during POLE coupled with the observed diurnal heating cycle favored the formation of multiple layers having nearly uniform density. Such layers are observed to migrate vertically downward as a new layer is formed at the surface. Turbulent diffusive processes are likely to account for the observed migration. In the absence of strong winds, the water mass characteristics of a given layer can persist for several days. However, it is only the uppermost layer which interacts directly with the driving fluxes of momentum, heat and mass. Previously established layers become significant only when sufficient mechanical energy, supplied by either forced or free convective processes, becomes available to erode the density gradient at the base of the topmost layer. For the time scales associated with this study the present definition of mixed layer depth seems most appropriate. For studies involving seasonal and/or climatological time scales an alternate definition of mixed layer depth, emphasizing the behavior of the seasonal and permanent pycnoclines might be more appropriate.

The frequent establishment of a warm surface layer in the upper 10 meters on a diurnal time scale is clearly evident in Figure 4.8. Nocturnal cooling, coupled with a small surface wind stress ($\tau \lesssim 1$ dyne/cm^2) subsequently erodes this layer and re-establishes the depth

of a well-mixed layer at 50 to 60 meters. The only significant departures from this pattern occur midway into the experiment and at the very end. The period 6 through 8 February is marked by intermittently high wind stress (frequently exceeding 2.5 dynes/cm^2), and enhanced evaporative and net-long wave radiative flux rates. These processes combined to produce the period of sustained deepening shown.

The rapid response of the well-mixed layer to the natural variability of the surface boundary conditions is also illustrated by this event. Initially, high wind stress ($\sim$2.9 dynes/cm^2) results in a period of rapid deepening during the interval 200 to 215 hours. A subsequent quiescent period ($\tau \leq 0.5$ dynes/cm^2) allows for the quick re-establishment of the warm surface layer. A period of sustained winds (τ generally greater than 2.0 dynes/cm^2) results in the rapid and sustained deepening seen to occur during the interval 230 to 270 hours. During part of this period an entrainment rate of approximately 1 meter/hr. is observed. The higher wind stress conditions at 400 hours into the experiment (τ as high as 3.3 dynes/cm^2) result in a still more rapid deepening of the mixed layer.

Comparison with Theory

The local response of the well-mixed layer to a transient wind stress is discussed theoretically by Pollard et al. (1973). The PRT model predicts that after 1/2 pendulum day deepening is arrested at a depth h_{max} given by

$$h_{max} \approx \frac{2^{3/4} U_*}{(Nf)^{1/2}} \tag{4.8}$$

where U_* is the friction velocity, f the Coriolis parameter and N the Brunt-Väisälä frequency of the stably stratified fluid below. The mixed layer depth observed in the experiment is typically 2 to 3

times greater than the predicted value h_{max}. This suggests that entrainment at the base of the mixed layer due to shear of the mean flow was not the dominant mechanism in mixed layer formation during POLE. This result is consistent with the current meter observations of Davis and Regier (1974). They found that at frequencies below 0.05 Hz the currents at all levels were nearly parallel and of similar magnitude. Their measurements imply that little shear was available to erode the base of the mixed layer as required by the PRT mechanism.

Niiler (1975) suggests that for steady positive surface heating and wind stress, the erosion process is arrested at a depth

$$h_{max} \approx 2m_o \left(\frac{\tau_o}{\rho_o}\right)^{3/2} c_p \rho_o / B g Q_o \qquad (4.9)$$

where Q_o is the surface heat flux, c_p is the specific heat of seawater, B is the thermal coefficient of expansion and g is the acceleration of gravity. The constant m_o is related to the Kraus-Turner constant m through the relation $m = (C_{10}\rho_a/\rho_o)^{1/2} m_o$. In this context, C_{10}, ρ_a and ρ_o are the drag coefficient at ten meters, and the densities of air and water respectively. For values of Q_o greater than a few mwatts cm^{-2}, the predicted value of h_{max} with m = .0012 underestimated the observed mixed layer depth by about a factor of 2. This implies that the assumed value of m is too small by a similar factor.

The theory of the seasonal thermocline advanced by Kraus and Turner (1967) assumes that the turbulent energy available for mixing is some constant fraction m of the rate of downward transfer of energy from the local wind field. This portion of the turbulent energy is used to raise the potential energy of the water column (Equation 4.5). Turner (1969) estimated m from the observed winds and the rate of change of the potential energy of the well-mixed layer (Equation 4.5). Under the assumption that salinity does not contribute significantly to the observed density structure the potential energy with respect to a

reference depth r may be calculated from

$$P = \rho g B \int_{o}^{z} (T(z) - T_r) z dz \qquad (4.10)$$

where B is the thermal coefficient of expansion (2×10^{-4}/° C), g is the acceleration due to gravity, ρ the density of seawater, T(z) the observed temperature profile, and T_r the reference depth. A reference depth of 46 meters, corresponding to the observed mean mixed layer depth for the experimental period, was chosen. Hourly values of the potential energy relative to the 46 meters reference level are shown in Figure 4.9. To eliminate the high frequency variation in potential energy due to the presence of internal waves and horizontal advection, a twenty-four hour running mean of potenital energy was also calculated. It appears as the darker trace of Figure 4.9.

Examination of Figure 4.2 suggests that for a 25 hour period centered approximately 200 hours into the experiment, the wind speed increased abruptly and the well-mixed layer began to deepen more rapidly. This mixing event seems suitable for the experimental determination of m. Hourly values of m were calculated for this period by use of Equations (4.5) and (4.10) and a mean value of m = .0027 was obtained. This estimate of m is approximately double that of Denman (1973b), three-quarters that suggested by Halpern (1975) and about one-fourth the value obtained by Turner (1964). A second mixing event 370 hours into the observational period yields a value of m = 0.0017 in better agreement with the value m = 0.0012 observed by Denman.

The large degree of scatter between the various estimates suggests that additional observations are required to accurately determine the characteristics of the m parameter. Perhaps the mixing energy flux coefficient is not a constant but rather a function of local oceanic conditions. The possible presence of high energy inertial oscillations

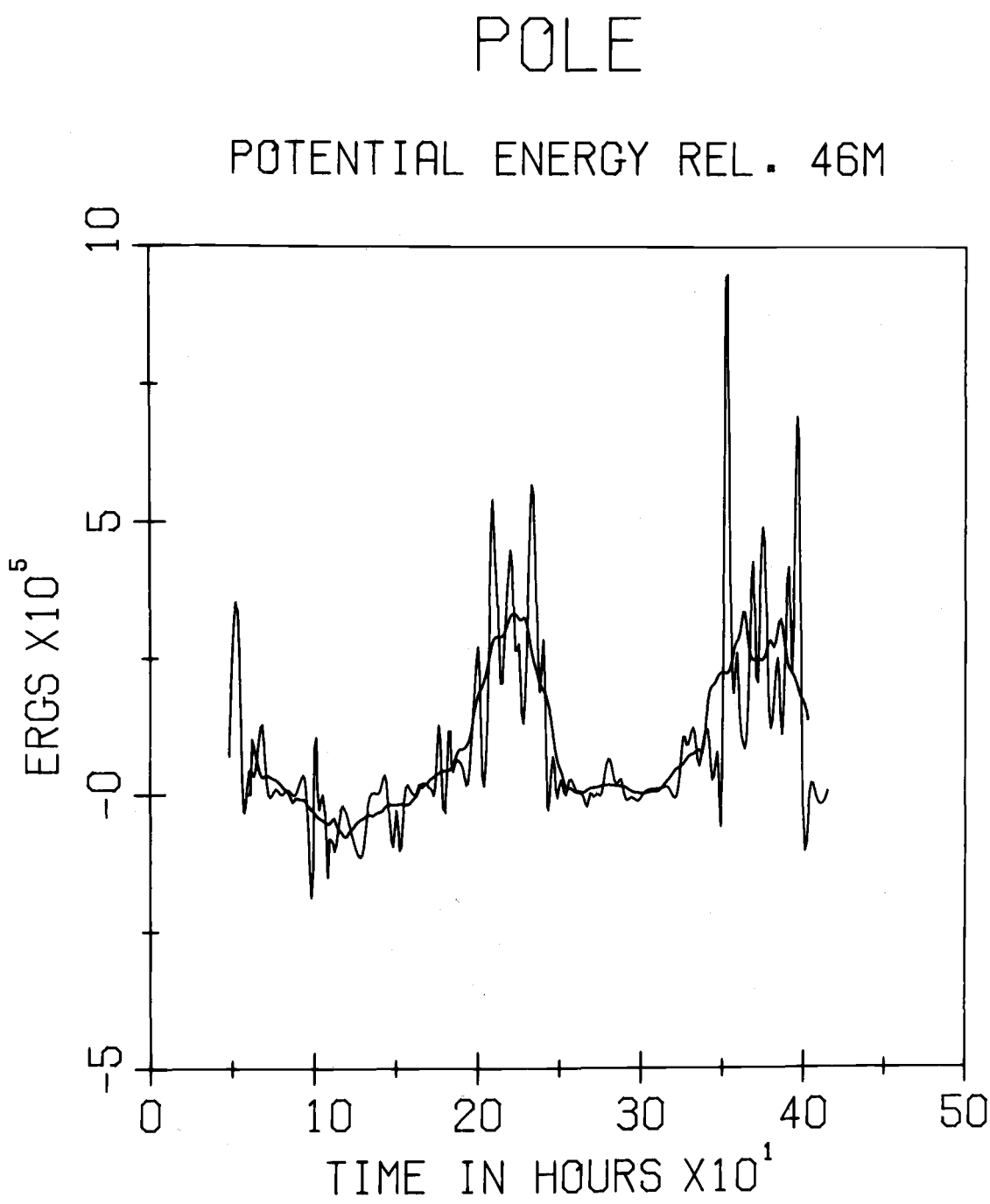

Figure 4. 9 Time series of the potential energy of the water column relative to the 46 meters, the mean mixed layer depth for the experiment. A running 24 hour mean of potential energy appears as the darker

in the upper mixed layer at the time of observations reported by Turner (1969) may partially explain the order of magnitude discrepancy in the reported values of m.

Improved Diagnostic Model

Parameterization of Solar Penetration

The one-dimensional mixed layer model of Kraus and Turner (1967) has been used to predict the depths of both diurnal and seasonal mixed layers. In the few cases where comparisons with observations have been made, a single exponential of the form $S(z) = S_o \exp[-\beta z]$ has been used to parameterize the penetrative radiation where S is the downward irradiance and S_o is the surface value. The attenuation coefficient, β, has been assumed constant with depth. Total downward irradiance profiles for typical ocean water types have been reported by Jerlov (1951, 1968). Values of β in the range 0.03 to 0.1 m^{-1} provide good agreement with observed absorption profiles for depths greater than 20 meters. However, the strong attenuation of solar flux observed in the upper 5 to 10 meters is not adequately parameterized by such a simple expression.

Observations of solar radiation as a function of depth in the central North Pacific (Chapter III) indicate that the irradiance decreases much faster with depth than exponential in the upper few meters, falling to one-third of the incident value between 2 and 3 meters depth. The departure from exponential is due to the selective absorption of the short and long wave components of the solar spectrum. The data suggest a more appropriate parameterization for the absorption of solar flux in the upper ocean is a double exponential of the form (suggested originally by Kraus, 1972)

$$S(z) = S_o \{\alpha_1 \exp(-\beta_1 z) + \alpha_2 \exp(-\beta_2 z)\} \qquad (4.11)$$

Best fit to the data taken during POLE yields values for the adjustable coefficients of $\alpha_1 = 0.62$, $\beta_1 = 0.67$, $\alpha_2 = 0.38$, and $\beta_2 = 0.05$. To conserve heat α_1 and α_2 must sum to unity.

The Extended Model

With this parameterization of the absorption of solar flux the complete set of vertically integrated equations defining the behavior of the upper mixed layer, under the assumptions of Kraus-Turner (1967) deepening assume the form

Conservation of mechanical energy:

$$\frac{dT_s}{dt} = \frac{2}{h^2}\left[-(G-D)+Q_o h + S_o h(\alpha_1+\alpha_2) - R\left(\frac{\alpha_1}{\beta_1}+\frac{\alpha_2}{\beta_2}\right)\right.$$

$$\left. + S_o\left(\frac{\alpha_1}{\beta_1}\exp(-\beta_1 h)+\frac{\alpha_2}{\beta_2}\exp(-\beta_2 h)\right)\right] \qquad (4.12)$$

Conservation of heat:

$$H\left(w+\frac{dh}{dt}\right) = 2\left[G-D+S_o\left\{\left(\frac{\alpha_1}{\beta_1}+\frac{\alpha_2}{\beta_2}\right) - \left(\frac{\alpha_1}{\beta_1}\exp(-\beta_1 h)+\frac{\alpha_2}{\beta_2}\exp(-\beta_2 h)\right)\right\}\right]$$

$$-h\left[Q_o + S_o(\alpha_1+\alpha_2) + S_o(\alpha_1\exp(-\beta_1 h)+\alpha_2\exp(-\beta_2 h))\right]$$

$$h(T_s - T_{-h}) \qquad (4.13)$$

Bottom Boundary Condition:

$$\frac{dT}{dt}(h) = \frac{\partial}{\partial t}T(h) - \frac{dh}{dt}\frac{\partial T}{\partial z}\Bigg|_h = S_o(\alpha_1\beta_1\exp(-\beta_1 h)+\alpha_2\beta_2\exp(-\beta_2 h))$$

$$-\left(w+\frac{dh}{dt}\right)\frac{\partial T}{\partial z} \qquad (4.14)$$

T_s = sea surface temperature

h = mixed layer depth

G-D = difference between vertically integrated turbulent production and dissipation rates

Q_o = heat flux at the surface: (sensible, latent and net long wave)

S_o = net solar flux

H = Heaviside function, o for $w + \frac{dh}{dt} \leq o$, i. e. no entrainment

w = mean vertical velocity at the base of the mixed layer

For conditions of steady, positive surface heating, entrainment of cold water from below is balanced by heating within the mixed layer and the equations assume a simpler form:

$$h[Q_o + S_o(\alpha_1 + \alpha_2) + S_o\{\alpha_1 \exp(-\beta_1 h) + \alpha_2 \exp(-\beta_2 h)\}$$

$$= 2[G\text{-}D + S_o\{(\frac{\alpha_1}{\beta_1} + \frac{\alpha_2}{\beta_2}) - (\frac{\alpha_1}{\beta_1} \exp(-\beta_1 h) + \frac{\alpha_2}{\beta_2} \exp(-\beta_2 h)\}] \quad (4.15)$$

with a finite difference form for the sea surface temperature of

$$\Delta T_s = \frac{1}{h}[Q_o + S_o\{\alpha_1 + \alpha_2 - (\alpha_1 \exp(-\beta_1 h) + \alpha_2 \exp(-\beta_2 h))\}]\Delta t \quad (4.16)$$

The surface heat fluxes have been transformed, i. e. $Q_o = Q_{o*}/\rho_o c_p$ etc. Equations 4.12-4.14 are identical to those of Denman for the case $\beta_1 = \beta_2 = \gamma$ and $\alpha_1 + \alpha_2 = 1$. Restoring the correct dimensions of the fluxes and rearrangement of Equation (4.13) yields a diagnostic model of the behavior of the mixed layer during heating periods.

$$2(G_*\text{-}D_*) - \rho_o g B h\{\frac{Q_o}{\rho_o c_p} - \frac{S_o}{\rho_o c_p} \Pi(\alpha_1, \beta_1, \alpha_2, \beta_2, h)\} = o \quad (4.17)$$

where c_p, ρ_o and B are the specific heat, density and coefficient of thermal expansion of seawater, resepctively. Under the conditions of Equation (4.11) the solar penetration function becomes

$$\Pi(\alpha_1, \beta_1, \alpha_2, \beta_2, h) = \frac{2}{h}\{\frac{\alpha_1}{\beta_1}(1-\exp(-\beta_1 h)) + \frac{\alpha_2}{\beta_2}(1-\exp(-\beta_2 h))\}$$

$$-\{\alpha_1 \exp(-\beta_1 h) + \alpha_2 \exp(-\beta_2 h)\} \qquad (4.18)$$

The net heat flux and the incident solar flux at the surface are given by Q_o and S_o, respectively. For the special case of $\beta_1 = \beta_2 = \beta$, the last two equations yield the diagnostic model employed by Alexander and Kim (1976).

The closure hypothesis employed by Denman (1973b) following Kraus and Turner (1967), assumes that $(G_* - D_*)$ is the rate at which wind stress energy is made available for mixing within the upper layer (see also Equation 4.5)

$$G_* - D_* = m \rho_a c_D \overline{U}_{10}^3 \qquad (4.19)$$

The diagnostic model is not applicable during periods of net surface cooling because equilibrium cannot be achieved for these cases. Of the eleven days of simultaneous observations of the surface forcing conditions and the mixed layer depth (Table 4.1) only seven satisfy the condition of net surface heating averaged over 1 day. Daily means of the observed total heat flux, incident solar flux, wind velocity, sea surface temperature and mixed layer depth are given in Table 4.2 for the seven days of interest. Of these, four have mean wind speed slightly greater or less than 4 meters /sec., the wind velocity at which Denman obtained numerical solutions for the heat dominated regime. The remaining three days are characterized by significantly higher wind speeds. During such periods the effectiveness of the turbulent exchange of heat and mass across the air-sea interface is greatly enhanced and the net heat gain at the surface of the ocean is substantially reduced. For these periods, the approach to equilibrium may not have occurred and the results may therefore be unsatisfactory.

Table 4.2 Observed input parameters associated with diagnostic model computations of mixed layer depth and sea surface temperature. The observed mixed layer depth and sea surface temperature are also shown.

Time	Total heat mwatts/sq.cm	Incident flux mwatts/sq. cm	Wind m/sec	MLD (m)	Sea surf. temp. (^{o}C)
180.0	6.43	8.49	4.72	34.7	14.99
204.0	5.76	9.23	8.40	24.9	15.05
300.0	2.42	7.05	4.55	58.9	14.66
324.0	3.27	6.03	3.73	35.7	14.91
348.0	2.08	8.10	4.73	24.2	14.93
372.0	2.40	8.36	9.27	27.1	14.63
396.0	7.32	10.93	10.35	42.8	14.65

Results

In Figure 4.10 observed and diagnostically predicted values of mixed layer depth and sea surface temperature are shown for those periods satisfying the condition of net surface heating averaged over 1 day. Closure was obtained using the Kraus and Turner (1967) mixing energy hypothesis. A mixing coefficient of m = 0.0018 was used. Good agreement exists between observed and predicted values of both mixed layer depth and sea surface temperature for conditions of low wind speed and large total heat flux. With a total heat flux of 6.4 mwatts/cm^2 and a wind speed of 4.7 m/sec. agreement between observed and predicted mixed layer depth is within 1.7 meters. As the total heat flux becomes small and/or the wind stress becomes large agreement becomes poor. The failure of the diagnostic model to yield satisfactory results under these conditions indicates that during such periods the approach to equilibrium does not occur. In general, better agreement is seen between observed and predicted sea surface temperatures than between observed and predicted mixed layer depths.

The present results indicate that Kraus-Turner deepening yields unrealistic depths for the well-mixed layer under conditions of weak heating. Measurements of the vertical profiles of turbulent production and dissipation rates (G_*-D_*) are needed before significant improvement in the closure hypothesis can be made. The improved parameterization of solar absorption with depth (Chapter III) results in a more realistic distribution of absorbed heat in the upper layers and partially arrests unreasonable deepening rates in the absence of strong surface heating.

The frequent appearance of salinity compensated temperature inversions at the base of the well-mixed layer (100 meters) indicates that horizontal advection intermittently influenced the character of

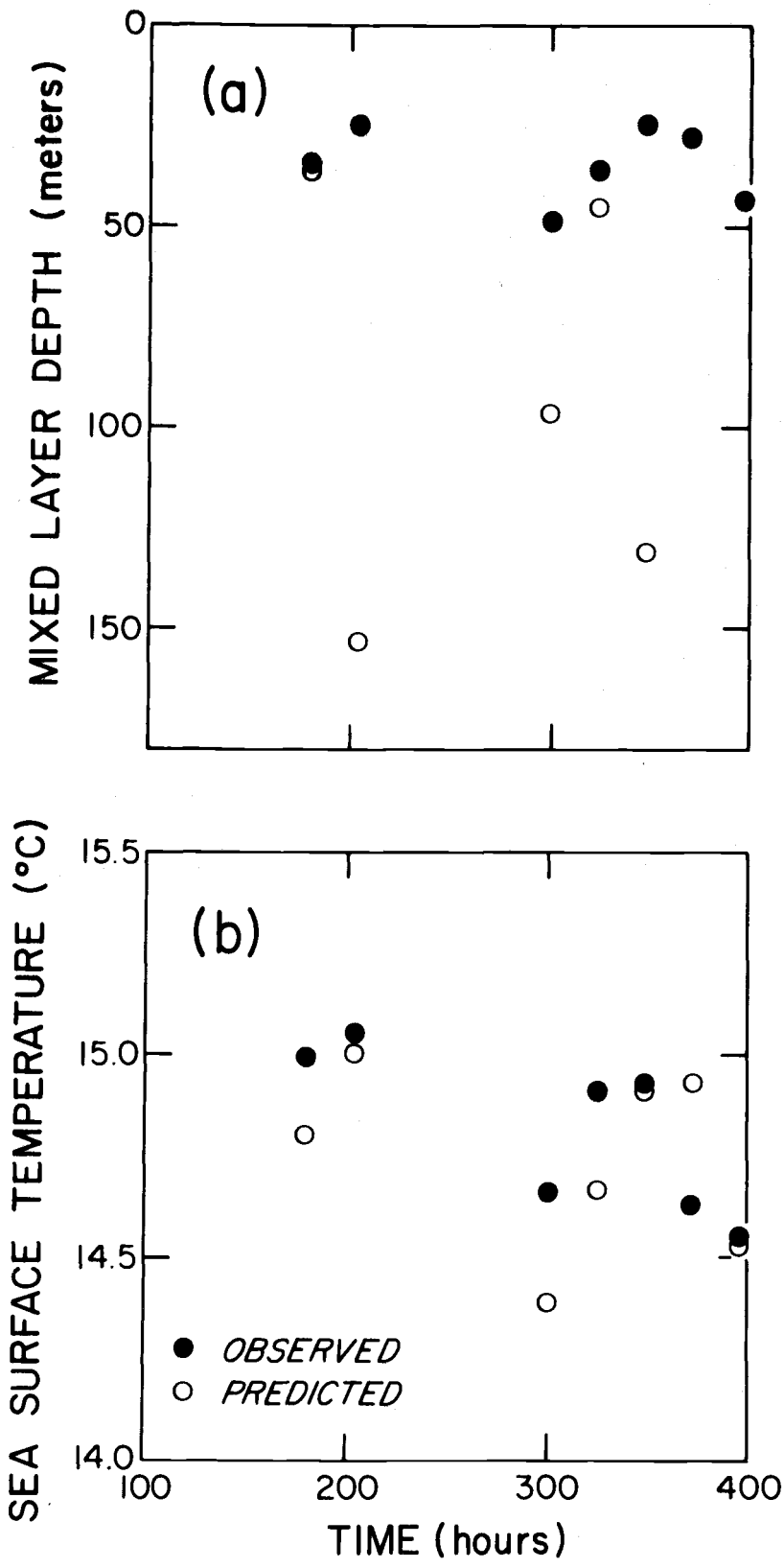

Figure 4.10 Observed and predicted sea surface temperatures and mixed layer depth, the POLE experiment.

the well-mixed layer (Simpson, 1976). The significance of horizontal advection in determining the behavior of the well-mixed layer is further suggested by finestructure and microstructure observations (Gregg, 1976) in the central North Pacific. His results indicate that in late winter in the absence of storms (the POLE conditions) strong lateral variability is more likely to significantly alter the heat content of the surface layer than is heat exchange at the surface. Lateral mixing (Stommel and Fedorov, 1967) may be a significant mechanism in determining the development of the well-mixed layer during POLE. These ideas are more fully developed in subsequent sections.

Horizontal Advection

The temporal variability discussed above was interpreted in terms of local surface processes acting vertically to produce the observed temporal variation in the upper ocean. However, the presence of salinity compensated temperature inversions at the base of the mixed layer was shown in Figure 4.11 suggest that horizontal advection, variable with depth, may also be relevant to a complete understanding of the observed structure. The basis for such an interpretation lies in the vertically integrated, averaged, conservation of heat equation

$$\frac{\partial H}{\partial t} + \nabla \cdot (UH) + \nabla \cdot (\nabla AH) = \sum_i Q_i \qquad (4.20)$$

where

$\frac{\partial H}{\partial t}$ is the local rate of change of the heat content, H.

$\nabla \cdot (UH)$ is the horizontal divergence of the heat flux, due to advective processes by ocean currents, U.

$\nabla \cdot (\nabla AH)$ is the divergence heat flux, both horizontal and vertical, associated with mixing processes, characterized by an Austrauch coefficient, A.

$\sum_i Q_i$ is the total heat flux due to radiative and turbulent transfer processes at the surface.

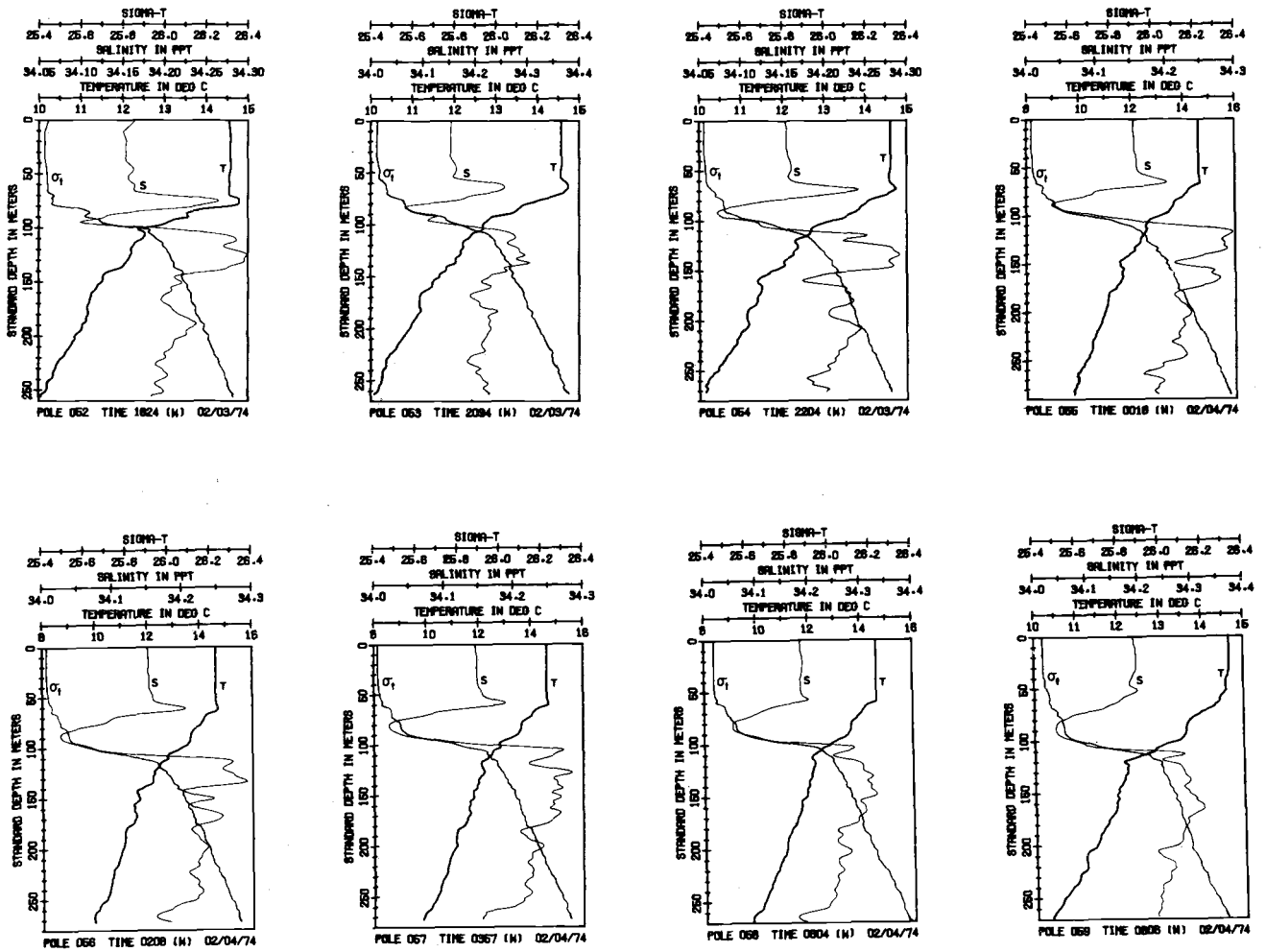

Figure 4.11 Individual hydrocasts illustrating the formation of inversions at base of mixed layer.

Vertical motions at the base of the vertically integrated layer are neglected. Mixing processes of the form $\nabla \cdot (\nabla AH)$ may reasonably be neglected for time scales of a few hours. The air-sea heat exchange processes were directly measured and the local change in heat content was calculated from the observed temperature profiles. Typical values of the hourly change in heat content vertically integrated over depths of 20, 40, 60, and 80 meters are of order $\pm 1.0 \times 10^{-6}$° C/sec. The second term in Equation 4.20 was calculated as the residual of the remaining terms. Current meter observations of Davis and Regier (1974) suggest typical velocities past FLIP (i.e. relative currents) are of order 1 to 10 cm/sec. Thus, horizontal temperature gradients are of order ±0.1 to ±0.01° C/km. Horizontal temperature gradients of this order are most probably due to local small scale structures which can be expected to be of limited horizontal extent. One might expect the large temporal variability in the local advective field to be scattered about a smaller mean value. Over the observational period advective effects are indeed significantly less, typically of order ±0.01 to ±0.001° C/km.

Errors associated with total surface heat flux are about ±10%. The vertically integrated changes in heat content are within the stated accuracies of the observed temperature profile, ±5%. The most serious error in the estimates of horizontal temperature gradient may be the neglect of vertical advection at the base of the vertically integrated layer. These errors, coupled with errors associated with the current observations of Davis and Regier suggest the above estimates of horizontal advection are accurate only to within an order of magnitude. Should the Subarctic Front have meandered into the experimental region, an upper value of 0.1° C/km would not be unreasonable. The role of advective processes cannot be fully explored until the analysis of additional observations taken during POLE are completed.

The Pycnocline

Temperature inversions at the base of the well-mixed layer have been observed in various parts of the world's oceans. Stommel and Federov (1966) report temperature inversions as large as 0.5° C at the base of the well-mixed layer near Timor. Bathythermograms taken in the northern tropical waters of the Atlantic Ocean by R/V CRAWFORD exhibit similar features just below a well-mixed layer typically no deeper than 50 meters. Observations by Tait and Howe (1968, 1972) in a region west of the Straits of Gibraltar indicate salinity compensated temperature inversions of high stability are characteristic of the region.

Similar features, shown in Figure 4.11, were observed in the central North Pacific during POLE. Other temperature inversions can be seen within and below the thermocline structure. The vertical extent, Δz, of an inversion is taken as that distance over which the temperature differential, ΔT, attains its maximum value. Inversions associated with the entire set of hydrocasts were sorted into six groups based upon their vertical length scale. A summary of the inversion characteristics associated with each grouping is provided in Table 4.3.

An approximate relation for the hydrostatic stability of the upper ocean at a level z is given by

$$E = 10^{-3}\left(\frac{\partial \sigma_T}{\partial T}\frac{dT}{dz} + \frac{\partial \sigma_T}{\partial S}\frac{dS}{dz}\right) \qquad (4.21)$$

Fedorov (1969) suggests that for the typical range of temperature and salinity gradients found within inversions, $\partial \sigma_T / \partial T$ and $\partial \sigma_T / \partial S$ may be assumed constant. Thus for a given vertical extent Δz Equation 26 may be rewritten as

$$\Delta S = -\frac{\alpha}{\beta}\Delta T + \frac{\Delta z E}{\beta} \qquad (4.22)$$

where $\alpha = 10^{-3}\ \partial \sigma_T / \partial z$ g cm^{-3}/° C and $\beta = 10^{-3}\ 2\sigma_T / \partial S$ gram cm^{-3}/‰.

Table 4.3 Characteristics of the salinity compensated temperature inversions observed during POLE.

Group	Length scale (meters)	Npts	Depth (meters)	$\triangle T$ (^{o}C)	$\triangle S$ ‰
1	2-3	556	2 ±.3	.02	.01
2	3-5	197	4 ±.5	.06 ±.004	.03 ±.001
3	5-10	172	7 ± 2	.10 ±.01	.05 ±.001
4	10-20	101	14 ±10	.15 ±.01	.08 ±.003
5	20-30	29	25 ±10	.14 ±.02	.07 ±.006
6	30	46	47 ±122	.06	.02

The above relation suggests a linear model of the form ΔS ‰ = a $\Delta T°$ C + b‰ is appropriate for relating the magnitudes of the salinity and temperature differentials across an inversion where b is approximately constant if E is assumed small. The results of such a model, applied to the groupings of Table 4.3, are shown in Table 4.4. The regression model indicates a high degree of correlation ($\geq .9$) between the magnitude of the temperature inversion and corresponding salinity maximum for inversions of 5 to 30 m thickness. A slightly lower correlation ($C = .8$) exists for inversions greater than 30 meters thickness. A poor degree of correlation ($\leq .65$) exists for inversions of less than 5 meters thickness. These results for the small inversions of order 5 meters or less may be uncertain because the salinities measured by the STD may be degraded for reasons given above. The high correlation coefficients associated with the regression models applied to inversion of intermediate length scale suggests that the warmer more saline water mass frequently intruding at the base of the thermocline is stable. Most likely this water mass is formed in the high evaporative region north of the Hawaiian Island Chain and is advected and mixed laterally with the colder less saline water of the central North Pacific.

Summary

Profiles of salinity and temperature (Chapter IV) in the upper 300 meters of the ocean were observed from R/P FLIP in January and February 1974 during the NORPAX POLE Experiment (35° N, 155° W). There was usually a well-mixed layer near the surface, although during light winds, a diurnal thermocline was evident. The structure below the thermocline was often complex with temperature inversions as large as 0.5° C. These inversions were compensated by salinity to stabilize the density profile. The depth of the well-mixed layer was correlated to mechanical energy input by the wind

Table 4.4 Values of the coefficients a and b obtained from application of the linear regression model ($S = a\ T + b$) to the various inversion types described above. Corresponding values of the correlation coefficient c and an estimate of the stability of each group obtained from Equation 26 are also listed.

Group	Length scale (meters)	a	b ‰	c	E* ($\times 10^8$)
1	2-3	.327	.004	.560	1.9
2	3-5	.354	.009	.644	1.5
3	5-10	.318	.013	.900	3.7
4	10-20	.369	.012	.954	3.0
5	20-30	.453	.003	.979	2.4
6	>30	.266	.008	.809	2.5

but was also influenced by horizontal advection of water having differing characteristics.

The one-dimensional mixed layer model of Kraus and Turner (1967) has been used to predict the depths of both the diurnal and seasonal mixed layers. In the few cases where comparisons with observations have been made, a single exponential of the form $S(z) = S_o \exp[-\beta z]$ has been used to parameterize the penetrative radiation where S is the downward irradiance and S_o is the surface value. The attenuation coefficient, β, has been assumed constant with depth. The data (Chapter III) suggest a more appropriate parameterization for the absorption of solar flux in the upper ocean is the double expoential of the form (equation 4.11). With this parameterization of the absorption of solar flux the complete set of vertically integrated equations defining the behavior of the upper mixed layer, under the assumptions of Kraus and Turner (1967) deepening were presented (Chapter IV). These equations were employed in diagnostic form to predict the behavior of the well-mixed layer observed during POLE. For conditions of low wind speed ($U \leq 4$ m/sec) and net heat gain at the surface predicted values of mixed layer depth and sea surface temperature agree well with observations. During periods of higher wind speed the effectiveness of the turbulent exchange of heat and mass across the air-sea interface was greatly enhanced and the net heat gain at the surface significantly reduced. For these periods, the approach to equilibrium probably did not occur and the results of the diagnostic model proved unsatisfactory.

The theory of the seasonal thermocline advanced by Kraus and Turner (1967) assumes that the turbulent energy available for mixing is some constant fraction m of the rate of downward transfer of energy from the local wind. A estimates of m, based upon the observed winds and the rate of change of the potential energy of the well-mixed layer, POLE were made. For the deepening event occurring mid-way

through the experiment a mean value of m = 0.0027 was obtained. This estimate of m is approximately double that of Denman (1973b), three-quarters that suggested by Halpern (1975) and about one-fourth the value obtained by Turner (1964). A second mixing event 370 hours into the POLE observational period yields a value of m = 0.0017 in approximate agreement with the value m = 0.0012 observed by Denman.

The large degree of scatter between the various estimates suggests that additional observations are required to accurately determine the characteristics of the m parameter. It is likely the mixing energy flux coefficient is not a constant but rather a function of local oceanic conditions. Irradiance measurements made simultaneous to a mixing event would enable elimination of one degree of freedom from the governing equations (i.e. the α's and β's would be specified by observations, Chapters III, IV). Thus the equations of Chapter IV could be used to hindcast the best value of m based upon observed model inputs and the agreement between predicted and observed values of mixed layer depth and sea surface temperature. This approach eliminates the specification of arbitrary references levels and temperatures in the calculation of the change in potential energy of the water column upon which the values of m reported in the literature are based.

V. SMALL-SCALE SEA SURFACE TEMPERATURE STRUCTURE

Introduction

Energy transfer between the ocean and the atmosphere is strongly affected by the temperature of the surface of the ocean, T_s. Radiometric measurements of the sea surface temperature (Ewing and McAlister, 1960; McAlister, 1964; McAlister and McLeish, 1969) demonstrate the existence of a cool surface layer characterized by temperature deviations as large as 0.5° C from the bulk temperature, T_b, below. Such temperature deviations are associated with variations in the thermal boundary layer thickness, δ_w (Hasse, 1963). The thermal boundary layer is defined as the layer in which heat transfer is primarily by molecular conduction. Estimates of boundary layer thickness range from a few microns (high winds) to a few millimeters. These temperature gradients are established because the net upward flux of heat Q is generally positive, that is $Q = Q_{BN} + Q_{SE} + Q_L$ where Q_{BN} is the net long-wave flux emitted from the sea surface, Q_{SE} is sensible heat transfer generally from ocean to atmosphere and Q_L is the latent heat flux due to evaporation. The divergence of solar radiation is assumed negligible. Processes associated with the formation and destruction of the thermal boundary layer are shown in Figure 5.1.

Osborne (1964) developed a steady-state model of the ocean surface energy balance in which the sea surface temperature is viewed as a small departure from the underlying bulk temperature.

$$T_s = T_b + \Delta T_c + \Delta T_r + \Delta T_e \qquad (5.1)$$

The correction term ΔT_c represents combined air and water conduction and is typically smaller than the radiation term ΔT_r or the evaporative term ΔT_e. Osborne suggests that variations in the boundary layer thicknesses δ_w and δ_a are the primary sources of variation in the correction terms. He argues that thinning or thickening the

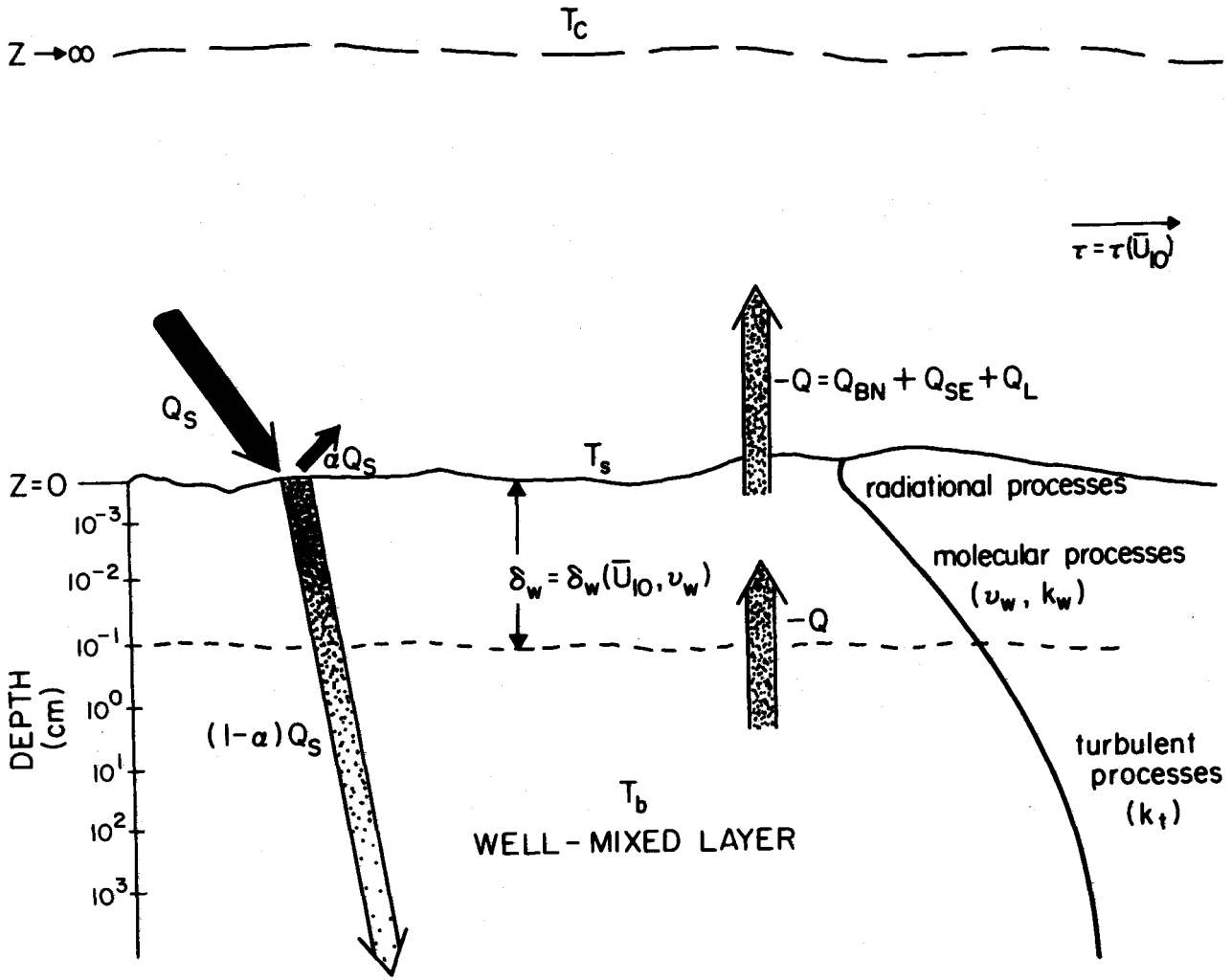

Figure 5. 1 Heat flux conditions at the air-sea interface. The upward flux of heat Q from the water below the interface is generally positive, that is $Q = Q_{BN} + Q_{SE} + Q_L$ is usually from ocean to atmosphere.

boundary layers by a factor of two can result in changes in sea surface temperature $\sim 0.5°$ C.

Large variations in the drag coefficient over water might account for rapid changes in boundary layer thickness. However, direct measurements of momentum, heat and moisture transfer (Firehe, Schmidt; 1976) made simultaneous to the observations presently reported indicated that the drag coefficient is nearly constant up to wind speeds at least as large as $\overline{U}_{10} = 10$ m/sec.

Stability-instability transitions in the thermal structure adjacent to the interface might also affect boundary layer thickness. Convective instability, resulting from cool air being heated from below ($T_a < T_s$), establishes a thin, well-defined air laminar boundary layer. A net heat loss at the ocean surface ($T_b > T_s$) resulting in the formation of a convectively unstable surface layer, establishes a thin, well-defined water laminar boundary layer.

Abrupt changes in the normal and tangential components of stress may also account for abrupt changes in boundary-layer thickness (Batchelor, 1967; Osborne, 1968). Experimental evidence (Ewing, 1950; Cox and Munk, 1954; Goodrich, 1962; Roll, 1965) suggests that discontinuities in stress (i. e. the presence of surface films and slicks) result in a reduction of drag and a thickening of the laminar boundary layer. Slicks are radiometrically cooler than clean water (Osborne, 1964); as if the boundary layer was thickened.

The physical mechanisms responsible for the abrupt boundary-layer alterations are presently a matter of dispute. Estimates of oceanic thermal sublayer thickness (Wu, 1971) assume that the dominant coupling mechanism of horizontal stress at the interface is via the horizontal component of tangential stress. Phillips (1966) supports this position. But measurements (Dobson, 1971) of the effect of atmospheric pressure on wind-generated sea waves suggest that the normal stress is the dominant mode of coupling.

Saunders (1967) postulated the existence of thin quasi-laminar oceanic boundary-layers within which the frictional component of wind stress is transmitted by viscosity and the vertical heat flux is transferred principally by molecular conduction rather than by convection or turbulent exchange. As the Prandtl number for water is greater than unity (P = 8) the thermal boundary layer is assumed somewhat smaller than the viscous sublayer. Neglecting the divergence of solar radiation and assuming the major component of the temperature deviation ΔT ($T_s - T_w$) occurs within the conduction zone a dimensional argument led him to suggest that the temperature difference between the surface and the well-mixed layer below is

$$\Delta T = \frac{\lambda Q \nu}{k_w (\tau / \rho_w)^{\frac{1}{2}}} \qquad (3.2)$$

where ν is the kinematic viscosity of water, k_w is the thermal conductivity of water, τ is the shearing stress in the air above the interface and ρ_w is the density of water. The dimensionless constant λ is empirically determined from observations. Saunders suggests that an appropriate value lies between 5 and 10. For a given heat exchange between ocean and atmosphere, minimum temperature deviation is associated with high winds, a result consistent with reduced boundary layer thickness due to enhanced levels of oceanic turbulence. Saunders cautions that strong solar heating in the presence of light winds may induce stable stratification within the upper few meters of the ocean and render the above relation invalid.

Hasse (1971) derived a relation between the temperature deviation and the solar radiation (Q_S), the wind speed at 10 meters ($\overline{U}_{10}$) and Q.

$$\Delta T = C_1 \frac{Q}{\overline{U}_{10}} + C_2 \frac{Q_S}{\overline{U}_{10}} \qquad (5.3)$$

The calculated coefficients vary slowly with the depths over which the

temperature deviation is calculated. For negligible solar radiation, Paulson and Parker (1972) have shown Hasse's model to be nearly equivalent to that of Saunders. The basic difference between the two is the temperature dependence of the coefficient of $Q/\overline{U}_{10}$ (due to the molecular viscosity ν) in Saunder's model.

Laboratory measurements of heat transfer and thermal structure near an air-water interface (Hill, 1972) support the assumptions of the above models. Hill's results confirm that at low wind speeds the boundary layer is essentially laminar and large temperature deviations are observed. The presence of a surface-active film enhances the temperature deviation. High winds result in a wave roughened surface. The boundary layer then assumes turbulent characteristics and a marked reduction in temperature deviation is observed. Hill suggests that the transition between the two regimes occurs at $U_* = 35$ cm/sec. Laboratory measurements in the absence of waves (Paulson and Parker, 1972) suggest that the dimensionless constant λ (Equation 2) is independent of heat flux or stress.

Oceanic observations (Ewing and McAlister, 1960) indicate that warm spikes in sea surface temperature records are associated with intermittent destruction of the thermal boundary layer by surface waves. Similar features were observed in sea surface temperature records taken in the Caribbean during BOMEX (Barbados Oceanographic and Meteorological Experiment) (Paulson and Leavitt, 1972). Their analysis suggests that there is a significant coherence, typically about 0.3, between sea surface temperature and surface gravity waves, and that the peak in the coherence spectrum occurs at the same frequency as the peak in the wave spectrum, 0.11 Hz. The duration of warm spikes in the temperature record was about 1 second.

The relations due to Saunders (1967) and Hasse (1971) fail to explicitly incorporate the effect of surface waves on the temperature deviation, ΔT. Witting (1971) investigated alterations of thermal

boundary-layer structure in response to two-dimensional plane progressive irrotational waves of unchanging shape in an inviscid fluid. His results suggest that capillary waves can reduce the temperature deviation by factors as large as 9 if the heat flux at the interface is independent of the presence of waves. Gravity waves at most decrease the mean temperature gradient by a factor of 1.38. Regardless of wave form, the interior fluid is found to be physically closer to the free surface at a wave trough than at a crest and hence an excess of heat is expected to be transported through troughs.

Although they do not explicityly take into account the presence of waves, the relations derived by Saunders (1967) and Hasse (1971) do provide insight into the mechanism of energy transfer at the interface. The few reported field and laboratory measurements failed to specify the characteristics of the wave fields when present. The purpose of this Chapter is to describe an experiment during which simultaneous mid-oceanic observations from a stable platform of radiometric sea surface temperature, heat flux and surface waves were made and to interpret these observations in the context of the above theories.

Observations

Observations of sea surface temperature and wave height were made from R/P FLIP during two field experiments. FLIP provides an ideal platform from which to make such observations because its vertical motion in response to normal seas is about 10 cm. For the Ocean Wave Experiment (OWAX) FLIP occupied a station under free drift conditions approximately 60 miles off the coast of Baja California during the period 23 March 73 through 28 March 73. The direction of drift was southeast with position ranging from 118° 17' W. long. and 31° 28' W. lat. at the beginning of the experiment to 117° 35' W. long., 30° 48'N. lat. at the end. Additional observations were made during the POLE experiment, a component of the North Pacific Experiment (NORPAX). During this experiment FLIP occupied a station

approximately 800 miles north of the Hawaiian Island Chain under free drift conditions. The area of drift ranged from 35° 39' to 34° 36' N. lat. and 155° 05' to 155° 25' W. long.

Measurements of the various components of atmospheric radiation, downward irradiance, wind speed, hydrography and the latent and sensible heat fluxes were made. Details of these observations are found in separate papers (Paulson and Simpson, 1977; Simpson and Paulson, 1977a; Simpson and Paulson, 1977b). Latent and sensible heat fluxes were calculated under the bulk approximation with a drag coefficient of 1.4×10^{-3}. Time series of the mean surface heat flux, wind stress and sea surface temperature are given for OWAX in Figure 5.2. The mean sea surface temperature measurements made during POLE are also shown. Representative time series, sampled at 20 Hz, of sea surface temperature and wave height are shown in Figure 5.3. The records in Figure 5.3 exhibit short period warm spikes in sea surface temperature of 0.3 to 0.6° C amplitude. They are generally associated with sharp wave crests. These spikes are likely due to the intermittent destruction of the cooler surface layer at the air-sea interface.

Instrumentation

Sea surface temperature was measured with a Barnes PRT-5 radiation thermometer whose detector is a hyperimmersed thermistor bolometer. The instrument responds spectrally in the range 8 to 14 μ. The signal band-width is 3 Hz. The half-power field of view is 2°. During POLE the instrument was mounted from the main port boom which was 11.4 meters above mean sea level. The instrument was positioned 10.25 meters along this boom and viewed a spot on the water surface 70 cm in diameter. During OWAX the main boom was 3.5 meters above mean sea level. The instrument was mounted 17.5 meters along this boom and viewed a spot on the water surface

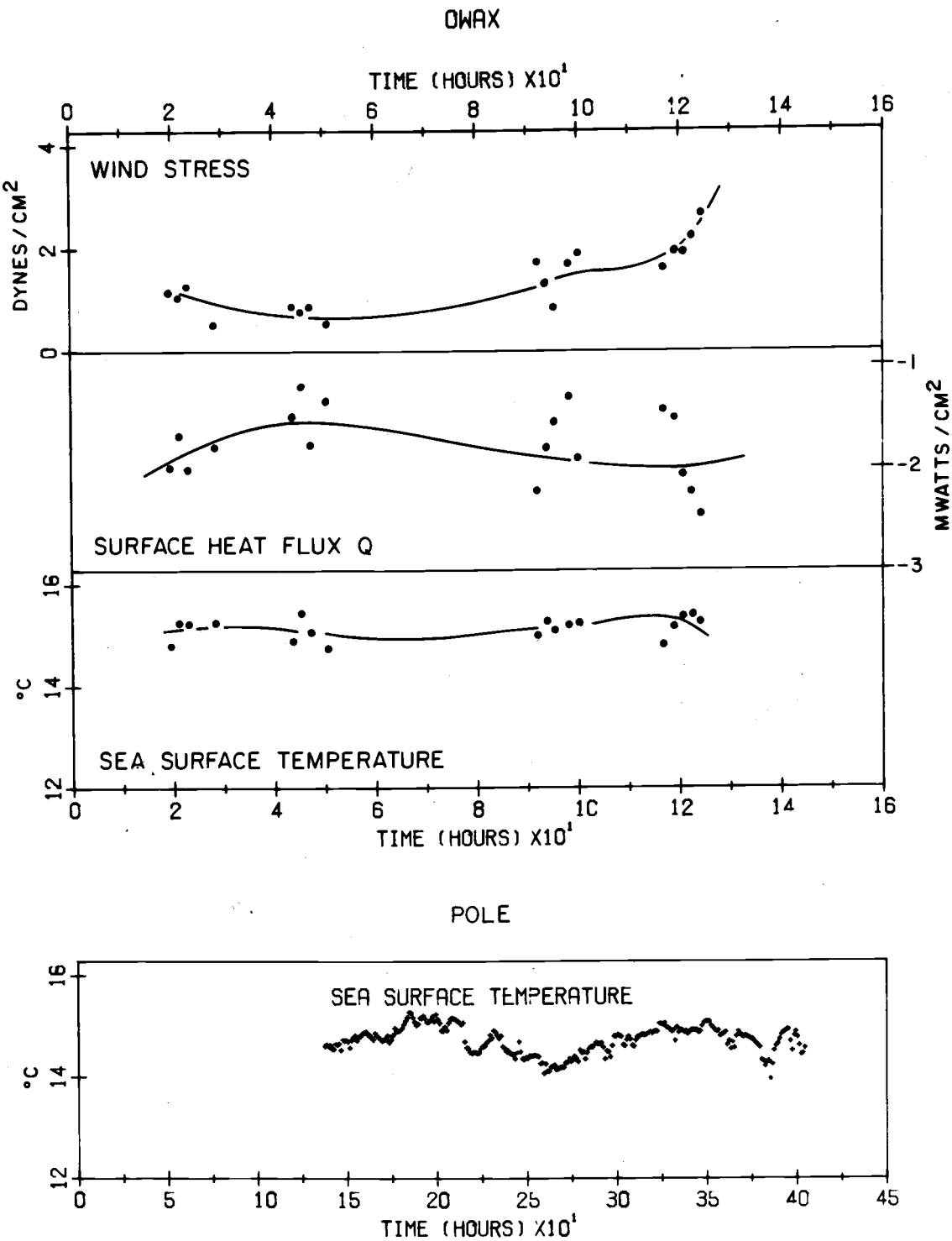

Figure 5. 2 The surface heat flux Q, wind stress τ and sea surface temperature T_S observed during the OWAX experiment. Also shown is the mean sea surface temperature time series measured during the POLE experiment.

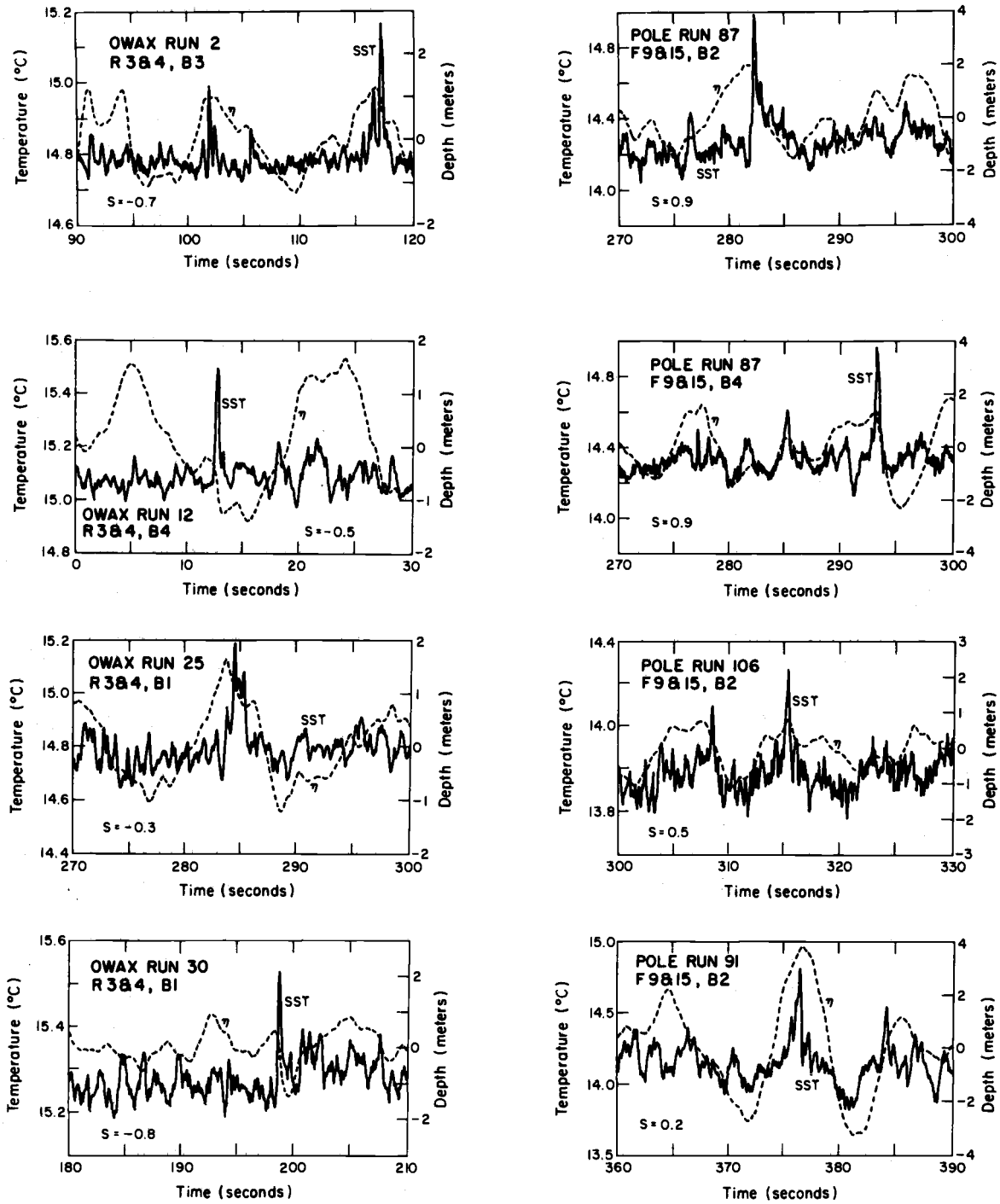

Figure 5.3 Simultaneous measurements of sea surface temperature and wave height illustrating the occurrence of warm spikes.

approximately 25 cm in diameter. The sensitivity of the instrumentation is about 0.03° C with an absolute accuracy of 0.5° C.

Wave height was measured with a resistance wave gauge. A 5.0 KHz signal was supplied to the wave staff. The instantaneous voltage across the probe was directly proportional to probe resistance. Thus, voltage output is a simple monotonically increasing function of instantaneous water depth below mean sea level. The transducer used #36 B&S gauge (diameter 0.005 in.) michrome wire with a resistance of 27.557 ohms per foot during OWAX, #32 B&S gauge (diameter 0.008 in.) michrome wire with a resistance of 10.14 ohms per foot during POLE. Resistance measurements of the transducers were made before and after each experiment to determine if stretching under load had significantly altered the resistance properties of the probes. These measurements indicate that the #36 gauge wire increased resistance by less than 0.01% during OWAX while the #32 gauge wire increased resistance by less than 0.2% during POLE. The wave staff was placed within 10 cm of the radiation thermometer during OWAX and within 30 cm during POLE. The instrumentation is shown in Figure 5.4.

Analysis

Data was recorded continuously in analogue form on magnetic tape. Runs selected for analysis were chosen to provide maximum data quality over the full range of stability conditions encountered. Prior to digitization at 20 Hz, the signals were low pass filtered at one-half the sampling frequency to prevent aliasing. Blocks of 16,384 data points, corresponding to 13.6 minutes of observations were then constructed. Each run consisted of four to six contiguous blocks.

Fourier coefficients were obtained from the various data

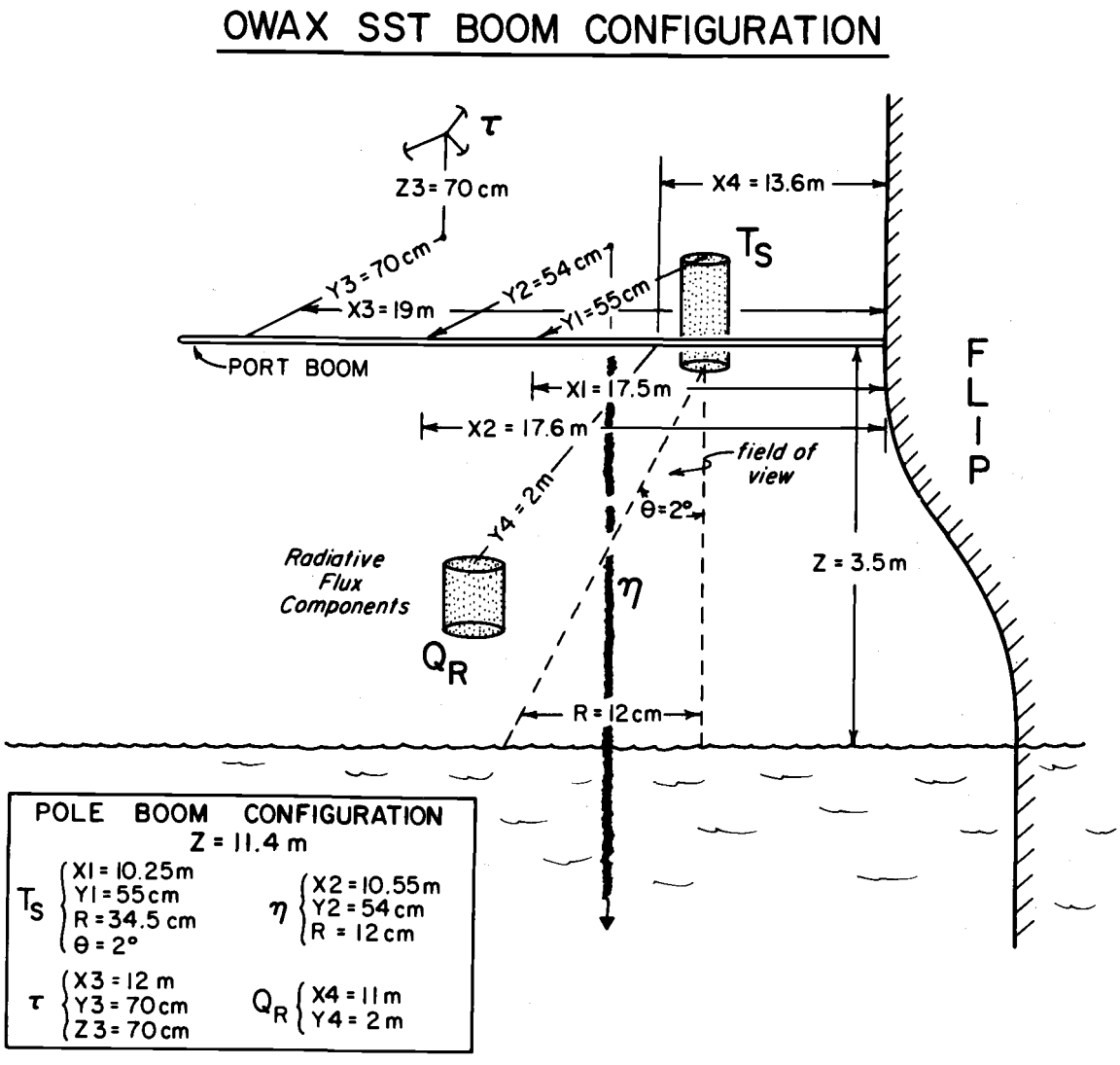

Figure 5. 4 Instrumentation configurations used to measure the sea surface temperature T_S, the wave height, η, heat fluxes and the wind stress τ during the OWAX experiment.

realizations using a fast Fourier transform (FFT) algorithm. Spectral, cospectral and quadrature spectral estimates were constructed from these coefficients. To reduce the variability in the raw spectral estimates both band and ensemble averaging techniques were used. Band averaging was accomplished by dividing the frequency range into equally spaced logarithmic frequency bands and averaging all the raw spectral estimates within a band. The band averaging process resulted in 31 frequency bands with approximately 7 bands per decade. Ensemble averaging was accomplished by averaging over all the realizations (4 to 6) associated with a given run the smoothed spectral estimates within a given frequency band.

Confidence intervals for the spectral estimates were constructed using a chi-square random variable with n equivalent degrees of freedom. Within a given frequency band the equivalent degrees of freedom n(f) is defined as twice the square of the ensemble-averaged spectral estimate divided by the estimated variance of the sample average associated with that smoothed spectral, i. e. $n(f) = 2\overline{(\phi(f))}^2/\text{var}\ (\phi(f))$. Confidence intervals so constructed reflect the measured spectral variability within a given ensemble-averaged frequency band.

Julian (1974) presents a method for calculating a significance level for the squared coherence estimator based upon tables of the distribution of the coefficients of coherence associated with a stationary bivariate Gaussian process developed by Amos and Koopmans (1963). The percentage significance level B for the squared coherence in terms of the number of degrees of freedom, df, within given ensembly averaged frequency band is

$$B = 1 - (1-P)\exp[1/(df/2-1)] \qquad (5.4)$$

where P is the desired percentage level of significance. (P = .95 for 95% significance level.) Empirical studies (Enochson, Goodman; 1965) suggest that confidence intervals for the squared coherency estimators, γ^2_{xy}, can be calculated, if the squared coherence is within the range $0.35 \leq \gamma^2_{xy} \leq 0.95$, based upon spectral density estimators with df $\geq$ 20 degrees of freedom. When these criteria were statisfied, 95% confidence intervals for the coherence were calculated using procedures suggested by Bendat and Piersol (1971). Confidence intervals (95%) for the phase estimators were determined using procedures suggested by Jenkins and Watt (1968).

The sea surface temperature deviation $\triangle T$ for a given run was calculated by subdividing each run into intervals of equal time duration $\triangle t$. Estimates of $\triangle T$ reported here are for $\triangle t$ of 2 minutes. Within each interval the maximum, minimum and mean sea surface temperatures were obtained. The maximum difference between the mean and maximum values was taken as representative of the sea surface temperature deviation from T_b for a given run. These deviations were then used to evaluate hypotheses advanced by Saunders (1967) and Hasse (1971) relating sea surface temperature deviation to momentum and heat transfer at the interface. Mean quantities related to the observed sea surface temperature deviation for a given run are shown in Table 5.1.

Sea Surface Temperature Statistics

Mean Structure

During POLE, 10 observations per minute of sea surface temperature were recorded in strip chart form using an Esterline-Angus multipoint potentiometric recorder. A digital representation was obtained with a chart digitizer. Twenty-four hour records were

Table 5.1

Run	Date	Time (w)	$\overline{U}_{10}$ (m/s)	τ dynes/cm^2	Q_L mw/cm^2	Q_{SE} mw/cm^2	Q_{BN} mw/cm^2	Q mw/cm^2	η_{RMS} meters	$\overline{T}_S$ °C	σ_{SST} (°C)^2	$\overline{\Delta T}$ °C	λ	$(\Delta T)^*$ °C	δ mm
							OWAX								
2	23 Mar 73	1928	8.22	1.16	-11.68	-1.43	-6.81	-19.92	0.69	14.81	0.05	0.29	8	0.32	0.8
3	23 Mar 73	2115	7.71	1.02	-10.79	-0.96	-5.06	-16.81	0.67	15.27	0.06	0.29	9	0.29	1.0
4	23 Mar 73	2303	8.53	1.25	-12.44	-1.69	-5.96	-20.09	0.70	15.24	0.07	0.29	8	0.31	0.8
7	24 Mar 73	0418	5.52	0.52	-12.44	-1.69	-3.72	-17.85	0.42	15.26	0.10	0.26	5	0.43	0.8
10	24 Mar 73	1941	7.12	0.87	-12.39	-0.24	-2.21	-14.84	0.40	14.90	0.08	0.19	6	0.27	0.8
11	24 Mar 73	2127	6.69	0.77	- 9.93	-0.16	-1.84	-11.93	0.61	15.45	0.08	0.16	6	0.24	0.8
12	24 Mar 73	2314	7.12	0.87	-11.51	-0.39	-5.80	-17.70	0.60	15.08	0.07	0.28	8	0.33	0.9
14	25 Mar 73	0234	5.58	0.54	- 9.20	-0.66	-3.43	-13.29	0.42	14.76	0.10	0.24	7	0.31	1.0
25	26 Mar 73	0417	6.36	0.70	-13.31	-1.14	-5.53	-19.98	0.51	13.24	0.16	0.51	11	0.41	1.5
29	26 Mar 73	2002	9.22	1.46	-15.48	-1.25	-5.46	-22.19	0.56	15.00	0.05	0.27	8	0.32	0.7
30	26 Mar 73	2152	8.74	1.31	-11.08	-0.86	-6.04	-17.98	0.60	15.29	0.04	0.28	9	0.27	0.9
31	26 Mar 73	2325	7.01	0.85	-11.28	-0.90	-3.24	-15.42	0.60	15.12	0.09	0.26	8	0.29	1.0
33	27 Mar 73	0218	9.85	1.67	-10.98	-1.07	-0.92	-12.97	0.59	15.21	0.04	0.12	6	0.17	0.5
34	27 Mar 73	0406	10.40	1.86	-16.22	-2.04	-0.80	-19.06	0.64	15.24	0.02	0.09	3	0.24	0.3
42	27 Mar 73	2048	9.62	1.60	-12.50	-1.38	-0.41	-14.29	0.78	14.81	0.02	0.10	5	0.20	0.4
43	27 Mar 73	2300	10.51	1.90	-13.36	-1.46	-0.33	-15.15	0.78	15.18	0.02	0.10	5	0.19	0.3
44	28 Mar 73	0046	10.45	1.88	-17.73	-0.92	-1.99	-20.64	0.78	15.37	0.03	0.10	3	0.26	0.3
45	28 Mar 73	0228	11.24	2.18	-18.46	-2.07	-1.75	-22.28	0.82	15.37	0.02	0.10	3	0.26	0.3
46	28 Mar 73	0411	12.24	2.58	-21.36	-1.33	-1.85	-24.54	0.84	15.25	0.02	0.11	4	0.26	0.3
							POLE								
87	7 Feb 74	0720	10.15	1.77	-19.38	-2.82	-7.73	-29.93	1.05	14.30	.08	.64	15	.36	.03
88	7 Feb 74	0923	8.63	1.28	-21.96	-2.25	-7.72	-31.93	1.04	14.25	.16	.58	11	.37	.04
91	7 Feb 74	1618	4.08	0.29	-11.98	-1.60	-9.63	-23.21	1.05	14.23	.17	.58	7	.73	.09
93	7 Feb 74	1947	1.14	0.02	- 7.74	-0.91	-8.02	-16.67	1.08	14.08	.32	.55	3	1.93	.31
150	12 Feb 74	1137	11.55	2.30	- 2.96	1.71	-4.61	- 5.86	0.42	14.91	.07	.35	47	.01	.03

merged to obtain a continuous time series of sea surface temperature for the experimental period. Occasional errors caused by radio interference were removed by interpolation from data before and after the error. Less than 1% of the data was affected by such interference. From the resulting time series, sequential one and fifteen minute averages were constructed. The fifteen minute averages were used to determine the long period spectral characteristics of the observed sea surface temperature. The one hour values shown in Figure 5. 2 were constructed from fifteen minute averages.

Daytime, nocturnal and diurnal means and standard deviations of the observed sea surface temperature (SST) are shown in Table 5. 2. As expected the daytime temperatures are generally warmer (on average 0. 19&C) than at night because of adsorption of solar radiation in the near-surface layer. Daytime variability in sea surface temperature as measured by the standard deviations of Table 5. 2 is substantially less than that associated with either nocturnal or diurnal variation in sea surface temperature. Maximum variability is associated with the diurnal variations in sea surface temperatures. Daytime, nocturnal and diurnal averages for the observational period are 14. 77 ±. 23 ° C, 14. 66 ±. 23° C and 14. 72 ±. 22° C respectively where the error is taken as one standard deviation.

The spectrum of the twelve day mean temperature series is shown in Figure 5. 5. A feature in the spectrum is the diurnal peak centered at 9 μHz (1. 2 days). This feature is associated with daytime heating of the near-surface layer due to absorption of solar radiation and cooling of the surface layer in the evening due to latent, sensible and net long-wave heat exchange at the interface. The sharp rise in power levels associated with periods greater than the diurnal is due to vertical heat exchange at the surface, deepening

Table 5.2 Mean values of the radiometrically observed sea surface temperature obtained during the POLE experiment.

Date	24 Hr. avg. (0000-2400)	Stand. dev.	Daytime avg. (0630-1830)	Stand. dev.	Night avg. (1830-0630)	Stand. dev.	Day/night diff.
2 Feb 74	--	--	--	--	14.64	.09	--
3 Feb 74	14.76	.10	14.80	.09	14.77	.07	+0.03
4 Feb 74	14.96	.19	15.04	.16	15.12	.08	-0.08
5 Feb 74	15.08	.12	15.07	.12	14.76	.27	+0.31
6 Feb 74	14.63	.14	14.70	.14	14.54	.14	+0.16
7 Feb 74	14.37	.14	14.40	.07	14.18	.08	+0.22
8 Feb 74	14.34	.14	14.36	.11	14.57	.11	-0.33
9 Feb 74	14.64	.14	14.64	.17	14.76	.09	-0.12
10 Feb 74	14.89	.10	14.95	.08	14.88	.08	+0.07
11 Feb 74	14.93	.09	14.98	.10	14.80	.13	+0.18
12 Feb 74	14.70	.16	14.70	.16	14.38	.22	+0.32
13 Feb 74	14.59	.27	14.79	.13	14.54	.10	+0.25
	Avg. 24 hr. 14.72±.22		Avg. daytime. 14.77±.23		Avg. nighttime 14.66±.23		

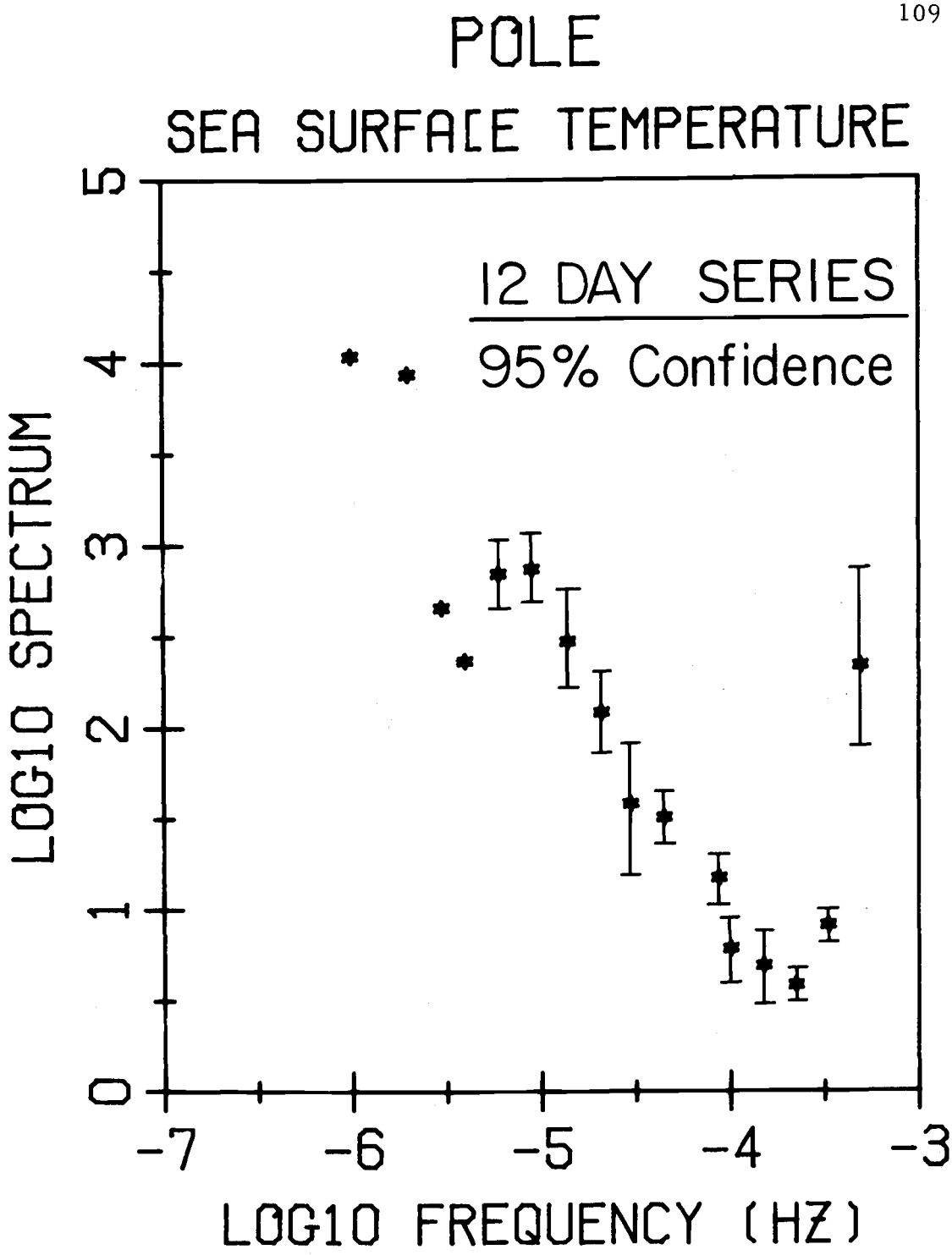

Figure 5.5 Spectrum of the twelve day mean sea surface temperature series observed during the POLE experiment.

of the well-mixed layer and horizontal advection. A characteristic time scale for this region of the spectrum is 10 days. A horizontal velocity scale based on mean current measurements relative to FLIP is 1 to 10 cm/sec. These scales combine to suggest that the advection of anomously colder or warmer patches (horizontal extend 10 to 100 kilometers) may partially account for the observed mean sea surface temperature structure. Analysis of satellite infrared sea surface temperature images supports this finding. Based on such images Stommel and Koziol (1976) have proposed a model for the adjustment of sea surface temperature due to underlying advective fields. The sharp increase in power near 1 millihz is due to aliasing of higher frequency variability into these spectral estimates. A match of the spectrum shown in Figure 5.5 with those obtained from 1 1/2 hour runs sampled at 20 Hz (see Figure 5.9) clarifies this point.

Small-Scale Structure

A total of twenty-four, 1 1/2 hour observations of sea surface temperature and gravity waves, sampled at 20 Hz, nineteen from OWAX and five from POLE are reported. The intermittent presence of a warm water surface plume, due to cooling water discharge from FLIP, altered the small scale sea surface temperature structure and contaminated the other runs made during POLE. The orientation of sensors and the direction of mean flow relative to FLIP during OWAX resulted in consistently clean records free from thermal contamination. The nature of the discharge during POLE was such as to be of little consequence in affecting the mean sea surface temperature structure discussed above.

Skewness and kurtosis for the individual 1 1/2 hour SST series, normalized by the third and fourth power of the standard deviation respectively, are listed in Table 5.3. The positive skewnesses

Table 5. 3 Skewness and kurtosis, normalized with the 3rd and 4th power of the standard deviation respectively, for analyzed OWAX and POLE sea surface temperature experiments. Each experiment contained approximately 64, 000 to 96, 000 SST values sampled at 20 Hz.

OWAX			POLE		
Run	Skewness	Kurtosis	Run	Skewness	Kurtosis
2	-0.7	4.5	87	+0.9	6.3
3	-0.7	4.0	88	+0.6	3.7
4	-0.6	3.9	91	+0.2	3.0
7	+0.3	2.4	93	-0.1	2.8
10	+0.1	2.2	150	+0.08	3.0
11	+0.8	3.4			
12	-0.5	3.4			
14	+0.03	2.5			
25	-0.3	3.6			
29	-1.0	5.2			
30	-0.8	4.8			
31	-0.2	3.9			
33	+0.6	5.4			
34	+0.3	5.9			
42	-0.09	3.2			
43	-0.2	3.3			
44	+0.02	2.9			
45	-0.2	3.4			
46	+0.2	6.7			

associated with many of the OWAX and POLE runs is indicative of the presence of warm spikes, due to the intermittent destruction of the thermal boundary layer, in the sea surface temperature. Local deepening of the mixed layer in response to enhanced wind stress and the subsequent entrainment of colder water or horizontal advection is most likely responsible for the negative skewnesses associated with some of the runs. Such runs do, however, frequently contain sections in which the presence of warm spikes is significant and for which the skewness over such sections is positive. Most of the runs have a kurtosis close to 3, the value for a normal distribution. A few of the runs (for example, POLE-87, K = 6.3, S = 0.9) are characterized by especially low background levels of sea surface temperature fluctuations superimposed on which are an abundance of warm spikes frequently exceeding 0.4° C amplitude.

Representative spectra with 95% confidence intervals for the 1 1/2 hour times series of sea surface temperature are shown in Figure 5.6. The decrease in spectral levels above 1 Hz is due to attenuation by the radiation thermometer while the increase in spectral levels above 4Hz is due to noise. Twelve runs during OWAX and POLE for which $Q/U_* \geq 0.58$ mjoules/cm^3 exhibit a spectral shape characterized by a broad flat plateau of high power level similar to that of OWAX Run #4. Q/U_* is proportional to a temperature scale as shown in Equation (2) (Saunders, 1967). Nine runs during OWAX have a value of $Q/U_* \leq 0.55$ mjoules/cm^3. These runs differ significantly from those of higher Q/U_I in that they show no broad plateau of high spectral energy but rather a decreasing power level similar to that of OWAX Run #44. At the peak in the wave spectrum all the runs with $Q/U_* \geq .58$ mjoules/cm^3 show power levels approximately an order of magnitude greater than those with lower Q/U_*. The single exception to this pattern is OWAX RUN #11 which has a plateau

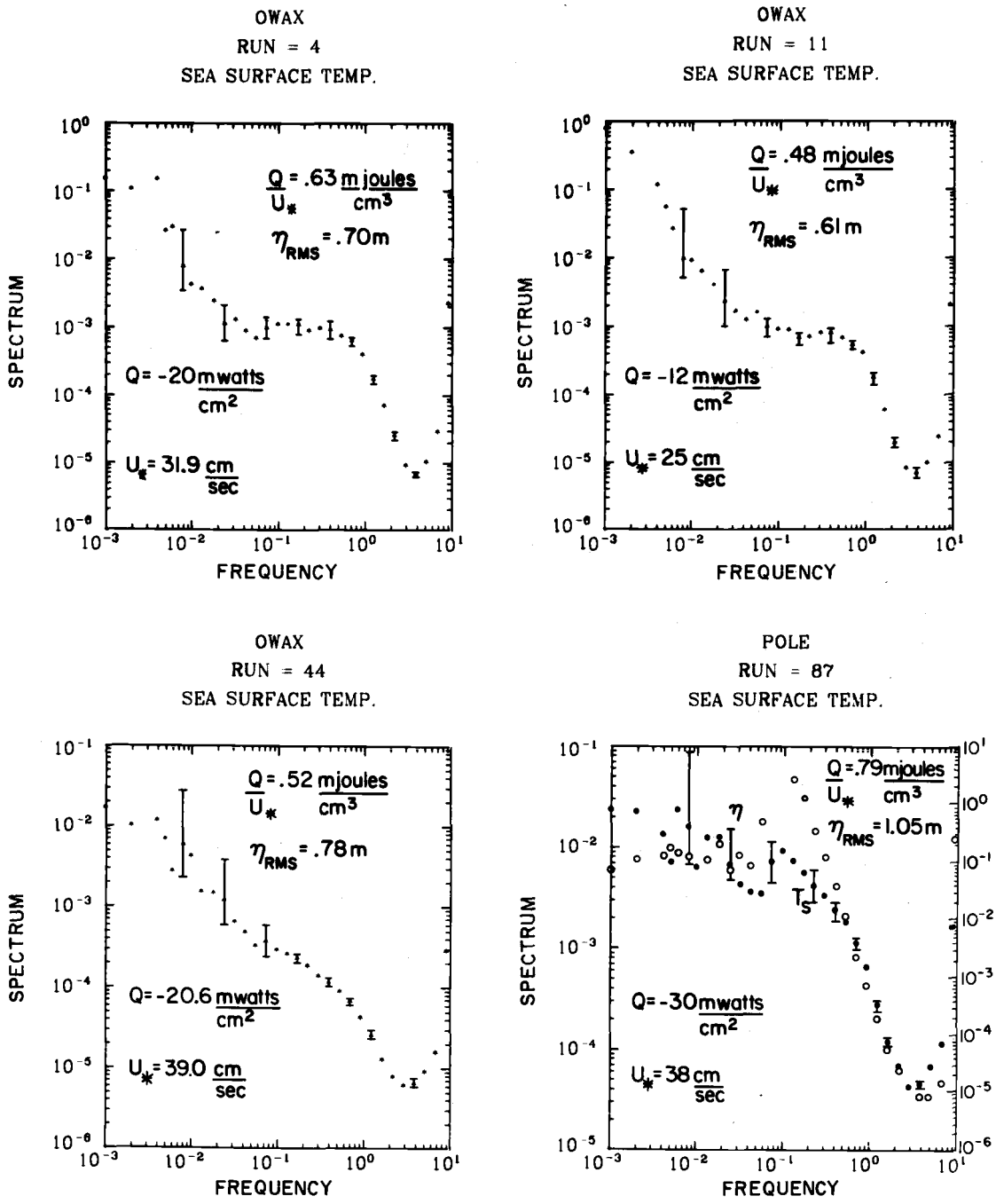

Figure 5.6 Representative spectra of sea surface temperature with 95% confidence intervals. A typical wave spectrum (open circles) is shown with POLE Run #87.

structure similar to that of OWAX Run #4 and an Q/U_* of 0.48 m/joules/cm^3. Associated with Run #11 is a temperature scale smaller than the scales associated with runs immediately preceding and following it. The spectra of OWAX Run #11 may have been influenced by the sea surface temperature structure established during the immediately preceding long-lasting period of high winds.

Most of the sea surface temperature spectra taken during POLE are associated with larger temperature scales ($Q/U_* \geq .79$ mjoules/cm^3) and higher root mean square waveheight ($h_{RMS} \geq 1$ m) than during OWAX. These runs are characterized by a peak in their sea surface temperature spectra at the same frequency as the peak in the gravity wave spectrum as in POLE Run #87. The sea surface temperature spectral level at this frequency is fully an order of magnitude greater than for the runs having the largest temperature scales during OWAX.

All of the sea surface temperature spectra of OWAX were sorted by values of Q/U_*. Those runs with highest Q/U_* (≥ 0.6 mjoules/cm^3) are shown in Figure 5.7A and exhibit the broad high-level spectral plateau discussed earlier. Those runs with lowest Q/U_* (≤ 0.45 mjoules/cm^3) are shown in Figure 5.7B and show the decreasing spectral slope characteristic of OWAX Run #44. If the spectra of all runs are plotted as shown in Figure 5.8A the two basic spectral shapes are confirmed. With the singular exception of OWAX Run #11, all sea surface temperature spectra having $Q/U_* \geq 0.58$ mjoules/cm^3 exhibit the broad high-level plateau spectral shape.

A grand ensemble-averaged sea surface temperature spectrum was constructed by averaging all OWAX runs within a given frequency band. The resultant spectrum is shown in Figure 5.8B. Such a spectral presentation cannot be justified rigorously because the relevant processes are obviously nonstationary over the wide range of conditions indicated by the spread in Q/U_* associated with individual runs. A grand ensemble-averaged SST spectrum was also calculated from the individual 1 1/2 hour POLE runs. The ensemble-averaged

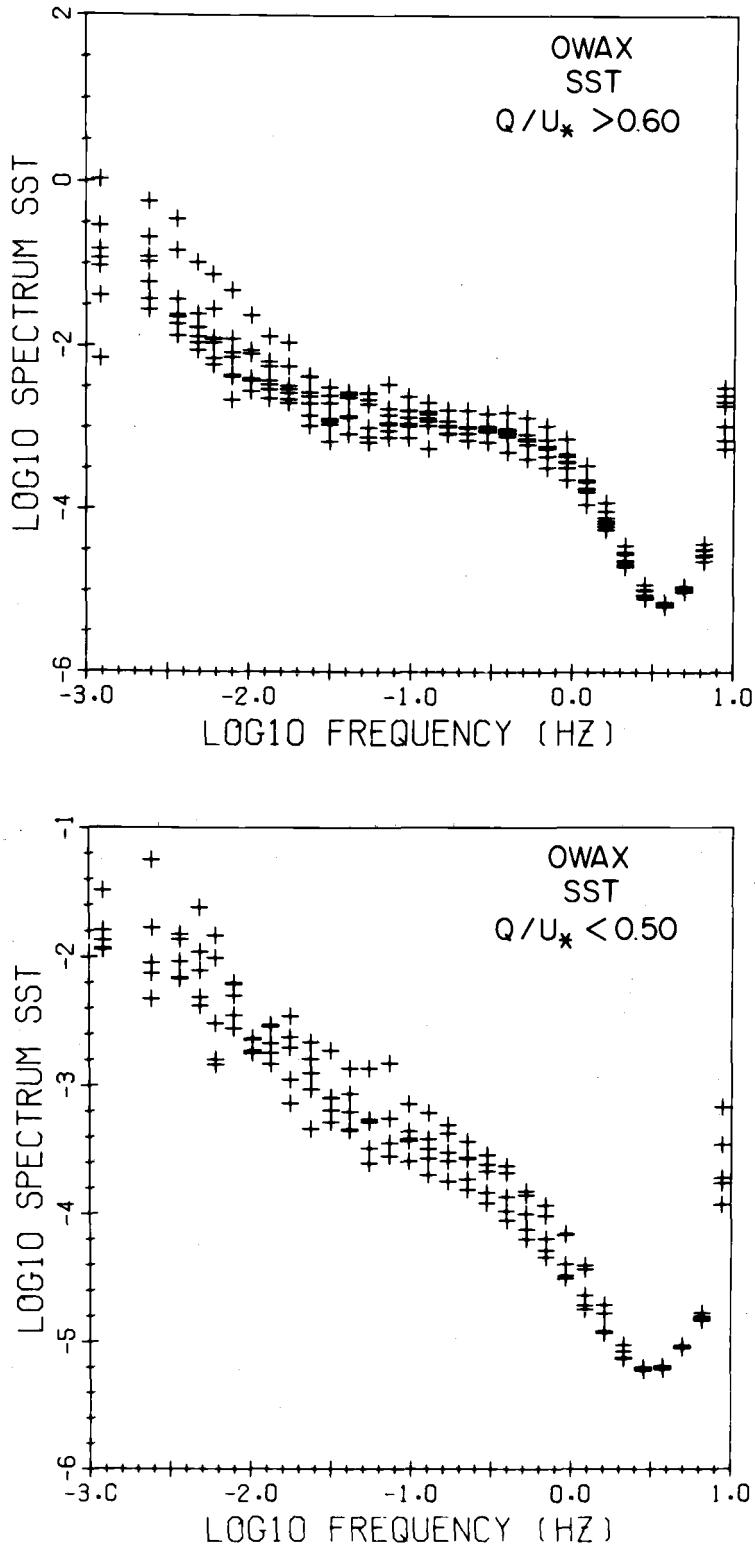

Figure 5.7 Runs with highest energy density ($Q/U_* \geq 0.6$ mjoules/cm^3) characterized by a broad high-level spectral plateau as shown in Figure 5.7A. Runs with lowest energy density ($Q/U_* < 0.45$ mjoules/cm^3) characterized by a decreasing spectral slope and lower power levels are shown in Figure 5.7B.

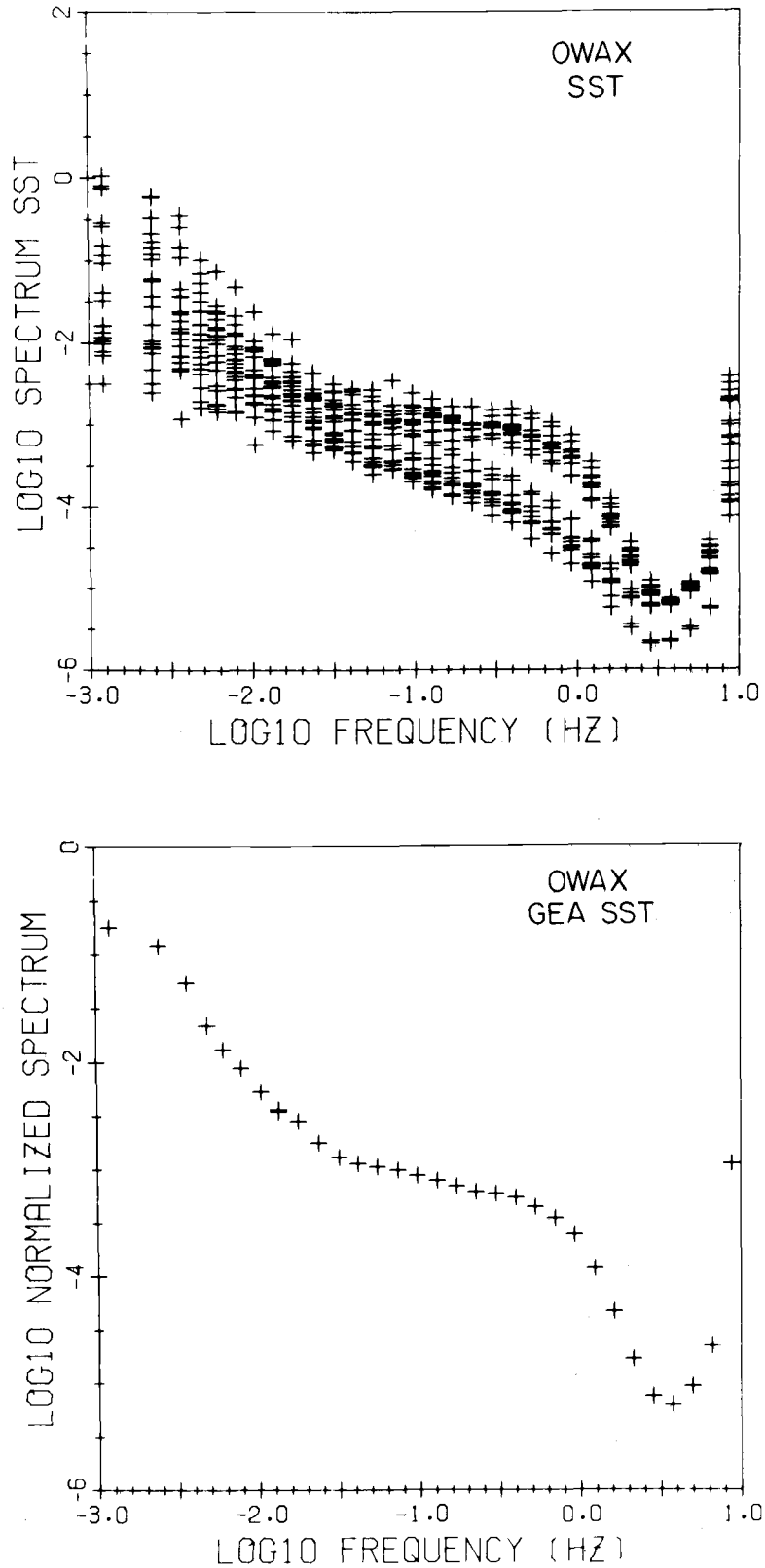

Figure 5.8 All the OWAX sea surface temperature spectra are shown. In Figure 5.8B the grand ensembly averaged SST spectrum for OWAX is shown.

spectrum was then merged with the 12 day mean sea surface temperature spectrum. The resulting sea surface temperature spectrum spans 8 decades of frequency and is shown in Figure 5.9. A good spectral match is evident at near 10^{-3} Hz.

Various normalization criteria were applied to all the OWAX runs in an attempt to collapse the individual runs to a universal spectrum form and discriminate between the various physical processes which might contribute to the generation of sea surface temperature variability. Three normalization factors for the SST spectrum were used: the sample variance calculated from the SST series, the square of the temperature deviation as predicted by Saunders (Equation 2) and the square of the measured deviation. In each case the frequency scale was normalized with respect to the peak in the gravity wave spectrum. None of these normalization factors appear successful in collapsing the spectra to a universal spectral form (Figure 5.10). The failure of the variance to collapse the spectra indicates that the operative physical processes generating the sea surface temperature fluctuations are dissimilar during the experiment. The failure of Saunders' relation to yield a unique spectral form may be related to the values of the total heat flux Q and the wind stress τ used in the determination of the sea surface temperature deviation (Equation 2). The latent and sensible heat fluxes used to compute the total heat flux Q ($Q = Q_{SE} + Q_L + Q_{BN}$) were determined from hourly standard meteorological observations using the bulk hydrodynamic approximations. The net long-wave flux Q_{BN} was determined from continuous direct observation of the net long-wave flux throughout a given run. The mean total heat flux employed by Saunders to estimate the temperature deviation ΔT has an associated time scale significantly larger than the time scale characteristic of the warm sea surface temperature spikes ($\tau \approx 1$ second). It may be the variability of the instantaneous stress and heat flux which are related to the magnitude of the sea surface

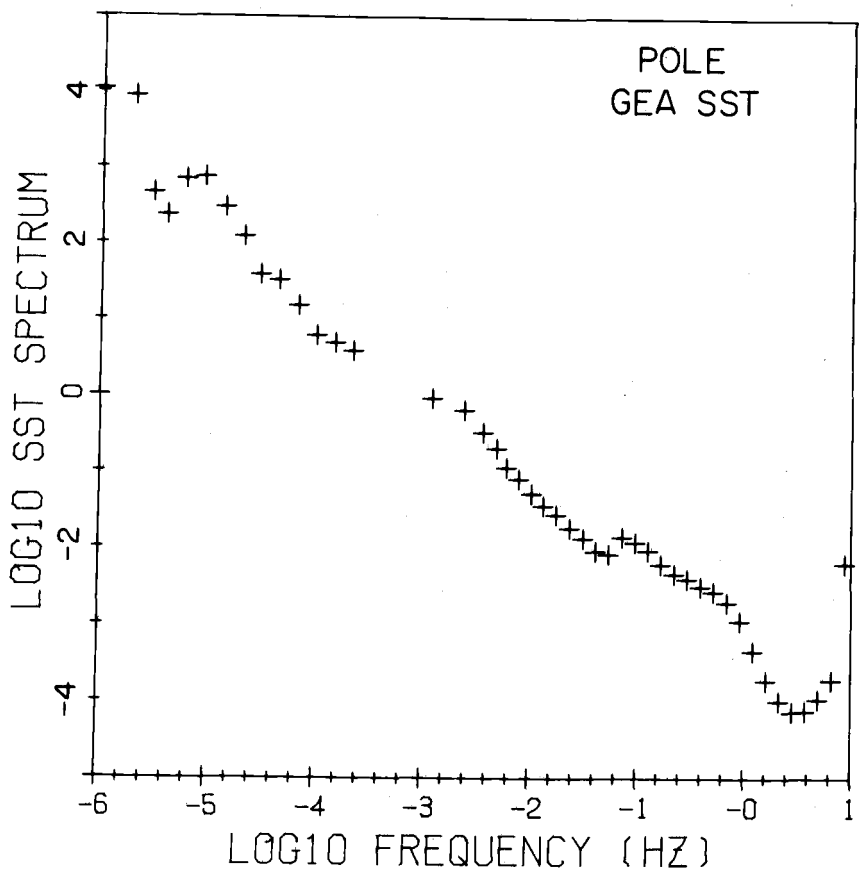

Figure 5.9 The SST spectrum resulting from the 12 day mean sea surface temperature series was merged with the grand ensembly averaged 1 1/2-hour POLE SST runs to produce the 8 decades of frequency spectrum shown.

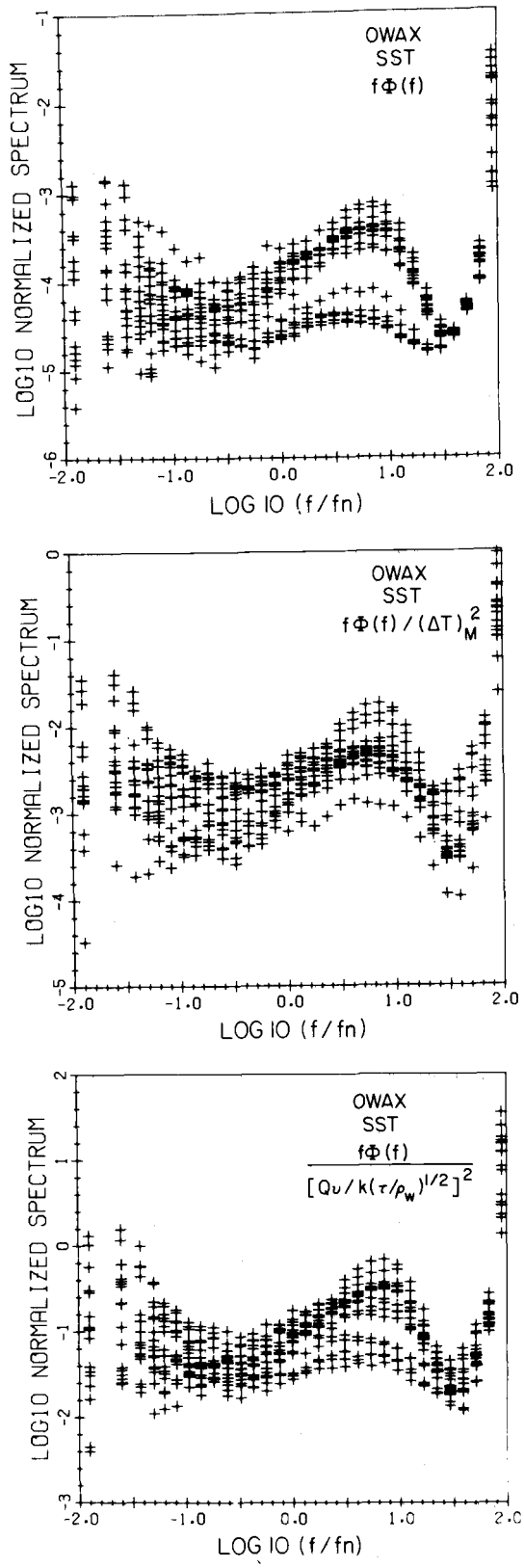

Figure 5.10 Spectra normalized by various factors to investigate the possibility of a universal form. The frequency axis was normalized with the frequency of the peak of the gravity wave spectrum.

temperature fluctuations seen in Figure 5.3. Further, the appropriate stress in relations (2) and (3) is not the wind stress at 10 meters but the viscous stress in the molecular sublayer immediately below the interface. However, both Saunders (1967) and Hasse (1970) employ the more conveniently measured total wind stress. Saunders allows the difference to be incorporated in the dimensionless constant λ. The wind stress at 10 meters will only closely approximate the stress in the viscous sublayer for the case of negligible wave generation. Such is generally not the case in the open ocean. A theoretical analysis by Witting (1971) showed that steep capillary waves may decrease the magnitude of the sea surface temperature difference across the thermal boundary layer by a factor as large as 9. The presence of steeply breaking gravity waves may also serve to reduce the magnitude of the temperature difference. Waves may affect the distribution of turbulent energy available for mixing in the uppermost layers of the ocean. The spectral evidence from the POLE time series (POLE Run #87) clearly indicates the influence of waves on the sea surface temperature spectrum.

Sea Surface Temperature-Wave Interactions

The theoretical investigations of Witting (1971), the laboratory experiments of Hill (1970) and of Paulson and Parker (1972) indicate that the magnitude of the sea surface temperature fluctuations are influenced by the presence of waves. The spectral results from the POLE and OWAX experiments (i. e. POLE Run #87) suggest that sea surface temperature fluctuations and surface waves are coupled. In Figure 5.11, standard deviations of the sea surface temperature for all the OWAX runs are shown as a function of the root-mean-square wave height measured during a given run. The linear least-squares fit shown in the figure has a correlation coefficient $R = -.80$. The decrease in total sea surface temperature variance with increasing root-mean-square wave height indicated in the figure is consistent

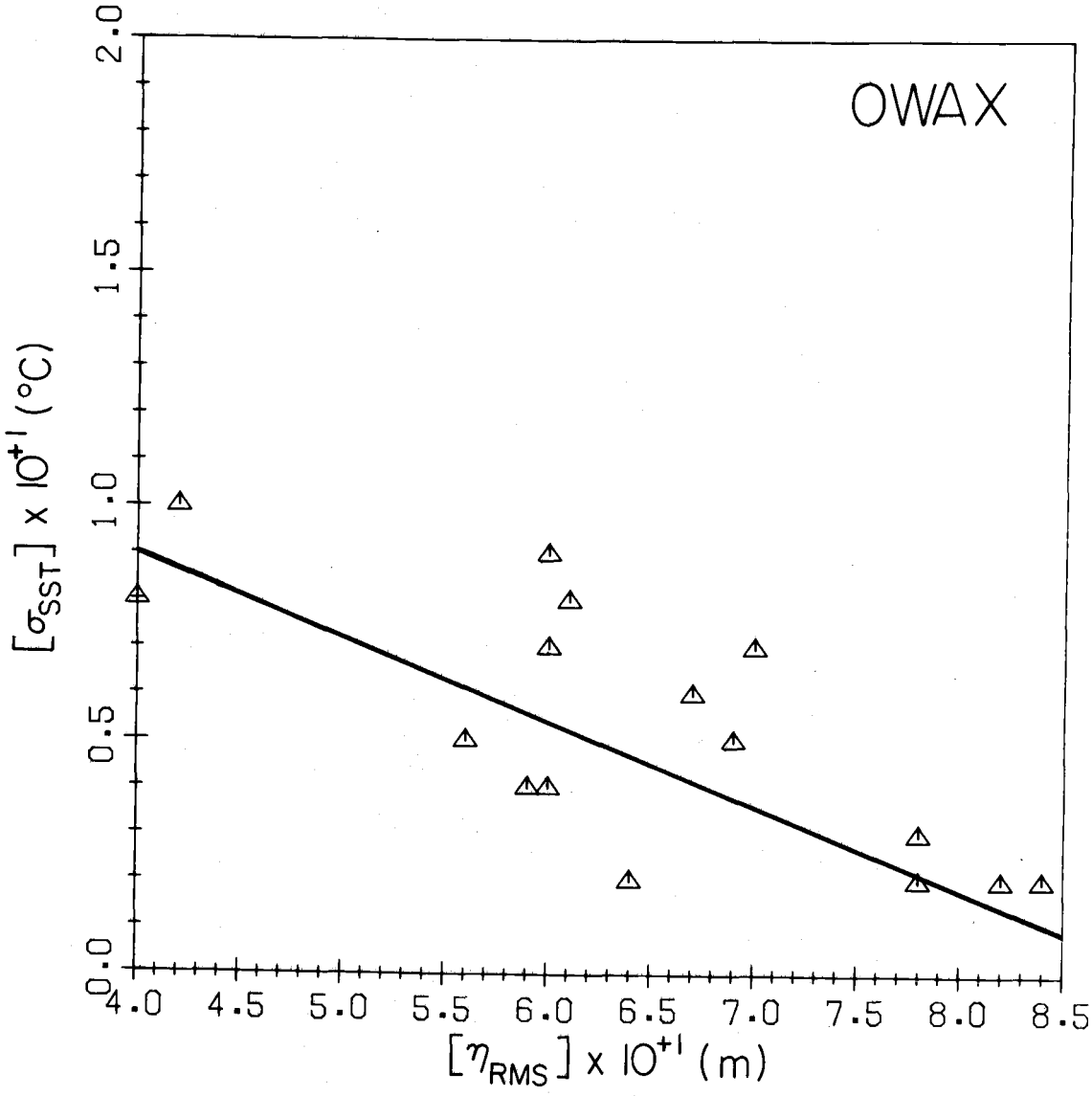

Figure 5.11 The standard deviations of sea surface temperature are shown as a function of root-mean-square wave height for all the OWAX runs.

with the theoretical predictions of Witting (1971). He suggests that the temperature deviation (ΔT) across the molecular, thermal boundary layer can be decreased by factors as large as 9 in the presence of capillary waves. If ΔT is decreased, one would also expect the magnitude of surface temperature fluctuations to be decreased. Destruction or thinning of the surface boundary layer could also be caused by processes other than capillary waves.

To investigate the coupling mechanisms between sea surface temperature fluctuations and surface waves, coherence and phase estimators were calculated between the surface gravity waves and sea surface temperature fluctuations measured during OWAX and POLE. The half-power field of view of the radiation thermometer is 2°. For geometric configurations used during OWAX and POLE (see Figure 5.4) this corresponds to a disc, of radius 12 and 35 cm respectively, over which the thermometer integrated its sea surface temperature signal. The characteristic length of a Pacific gravity wave is of order 100 meters. The limiting wavelength for capillary waves is 1.72 cm (Roll, 1965). However, observational evidence (Cox and Munk, 1954; Schooley, 1958a, b) suggests that capillary waves do not occur as isolated ripples on the surface of gravity waves but rather in patches of considerable extent. Thus one can expect to obtain physically meaningful coherence and phase estimates despite the different averaging scales of the respective transducers.

Representative coherence and phase spectra with a 95% significance level and/or confidence intervals are shown in Figures 5.12 and 5.13 respectively. All twenty-four of the OWAX and POLE runs show a statistically significant coherence, typically between 0.4 and 0.5, between surface gravity waves (η) and sea surface temperature (SST) at the frequency of the peak in the gravity wave spectrum. Some runs, such as OWAX Run #4 and POLE Run #87 have coherences as high as 0.67 and 0.8 respectively. Analysis of gravity waves and sea surface temperature measurements made during BOMEX (Paulson and Leavitt,

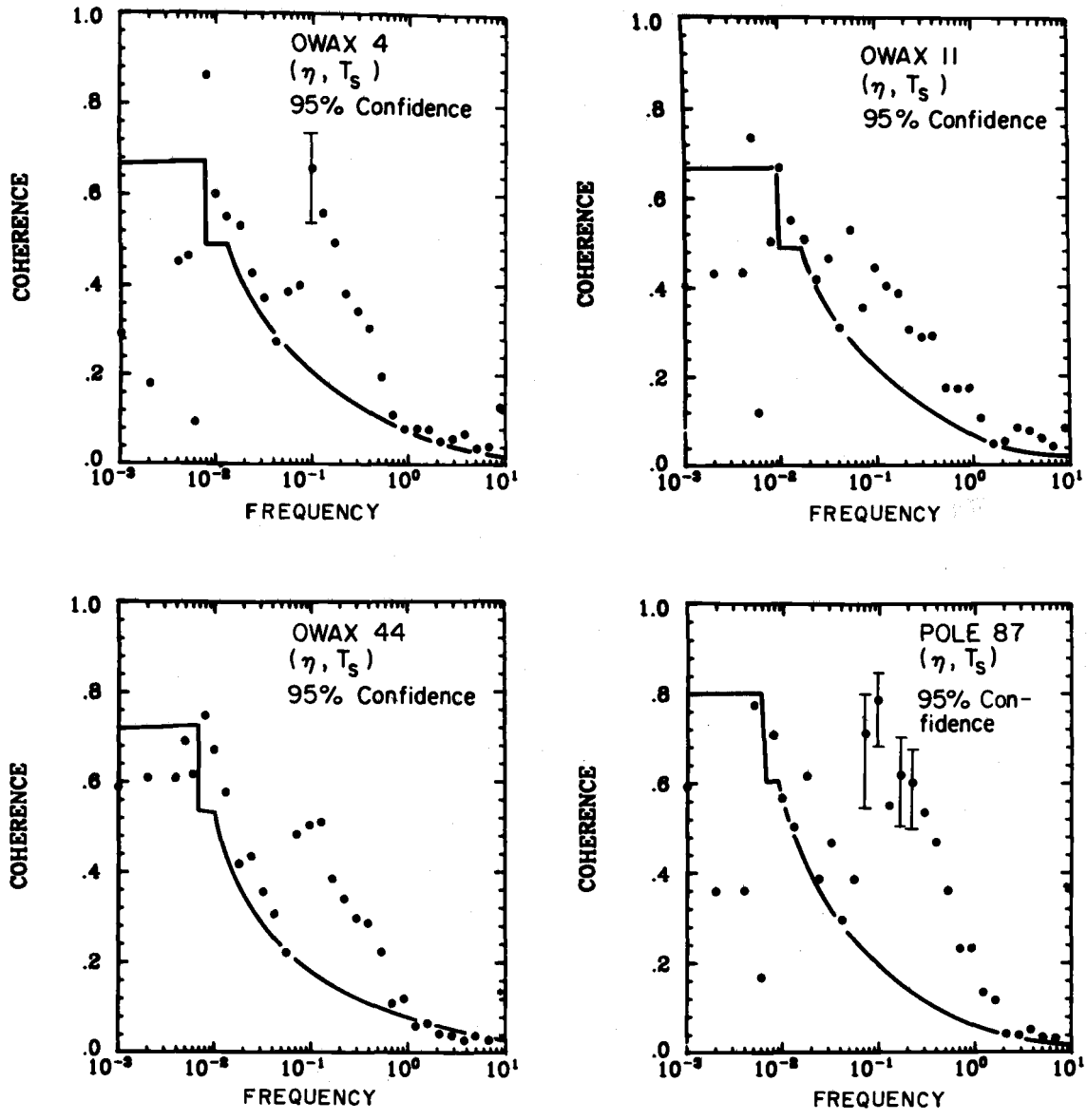

Figure 5.12 Coherency spectra for representative surface gravity waves (η) and sea surface temperature (SST) runs from both the OWAX and POLE experiments are shown. For all runs a significant coherence, typically ≥ 0.4, exists at the same frequency as the peak in the wave spectrum.

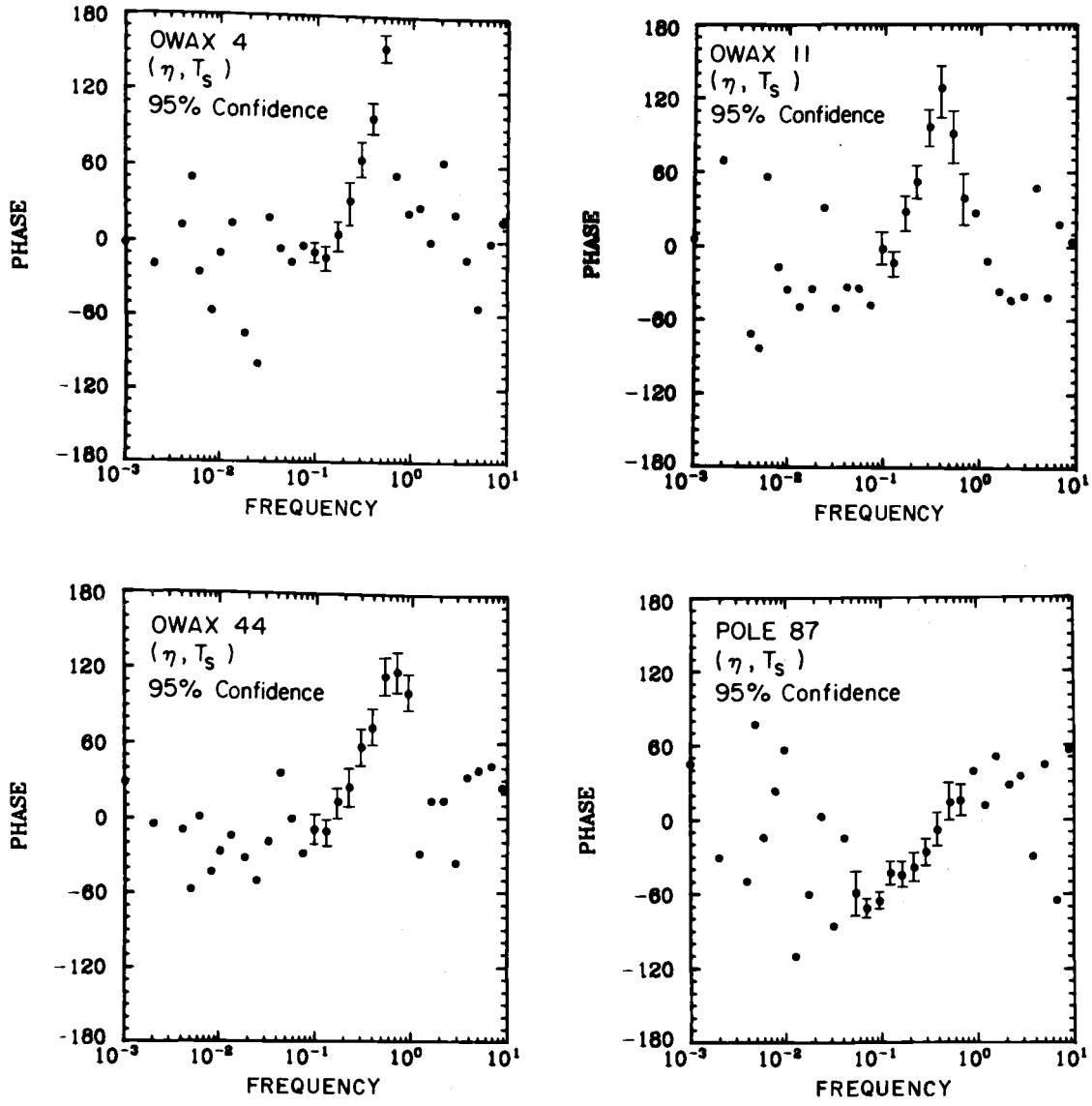

Figure 5.13 Phase spectra with 95% confidence intervals for representative surface gravity waves (η) and sea surface temperature (SST) runs from both OWAX and POLE experiments.

1972), yield a significant coherence, typically around 0.3, again at the same frequency as the peak in the wave spectrum. The higher coherence levels found during both POLE and OWAX result from differences in the geometrical arrangement of sensors employed during these experiments. During OWAX and POLE the wave gauge was within 10 and 30 cm respectively of the radiation thermometer used to measure sea surface temperature while during BOMEX the sensors were separated by approximately 3 meters. The high coherence associated with the very low frequency bands ($\leq 10^{-2}$ Hz) is due to contamination of this end of the wave spectrum by FLIP motion.

The phase spectra of Figure 5.13 are characterized by a significant positive peak (-90°) at 0.4 Hz with temperature leading the wave signal. Photographic analysis of the sun's glitter on the sea surface (Cox and Munk, 1954) shows that the downwind side of the wave is generally steeper than the upwind side. Such phase spectra suggest that breaking or thinning of the thermal molecular boundary layer on the steeply-sloped downwind side of the gravity wave is a likely mechanism for the production of warm spikes in the observed sea surface temperature records. A second feature is the negative peak at frequencies near the peak in the wave spectrum, with temperature lagging wave height. Anomalously high wind stress on the upwind slope of the wave crest may cause a decrease in the thickness of the surface boundary layer either by the generation of steeply-sloped capillary waves or directly by action of the tangential stress. This feature is present in all twenty-four runs. The suggestion that enhanced capillary waves on the upwind slope may cause warm temperatures is in qualitative agreement with the prediction of Witting (1971). To evaluate the relative effectiveness of the various wave forms in intermittently destroying the thermal molecular boundary layer additional measurements, particularly measurements of oceanic capillary waves, must be made. Breaking waves, capillary waves, turbulence in the water column, and gusts of wind causing high shear stress, are

all possible mechanisms for the destruction of the thermal boundary layer and production of warm sea surface temperature spikes. Occasionally, a cold spike is observed which is caused by a breaking wave, the form associated with the wave cooled by evaporation. In the observations reported, a small fraction of the surface (<1%) was covered by breaking waves.

Individual coherence and phase spectra for all the runs made during OWAX are shown in Figure 5.14. There is a significant coherence at the same frequency as the peak in the wave spectrum for all runs. Typically, the coherence at this frequency is greater than or equal to 0.4. The individual phase spectra all show the temperature lagging wave height ($\sim$-30°) associated with shorter period gravity waves. The variability in phase and coherence levels is associated with statistical uncertainties and the wide range of surface conditions observed during OWAX.

An attempt was made to determine sets of conditions which would allow a classification of the runs into groups within which this natural variability was significantly reduced. The runs were sorted into groups based upon maximum and minimum ranges of the variables U_*, η_{RMS}, Q, and Q/U_*. In Figure 5.15, the runs are shown sorted according to the friction velocity U_*. Those runs taken during periods of high wind stress ($U_* \geq 37$ cm/sec) show a reduction in the variability associated with both coherence and phase estimators. Runs taken during periods of reduced wind stress ($U_* \leq 25$ cm/sec) show significantly less scatter in the phase spectra. Large variability is seen in the coherence spectra associated with periods of low wind stress. Decreased variability associated with increasing U_* may be related to the transition zone at $U_* = 35$ cm/sec reported by Hill (1972) where a rapid decrease in boundary layer thickness occurred for U_* increasing. Classification according to root-mean-square wave height

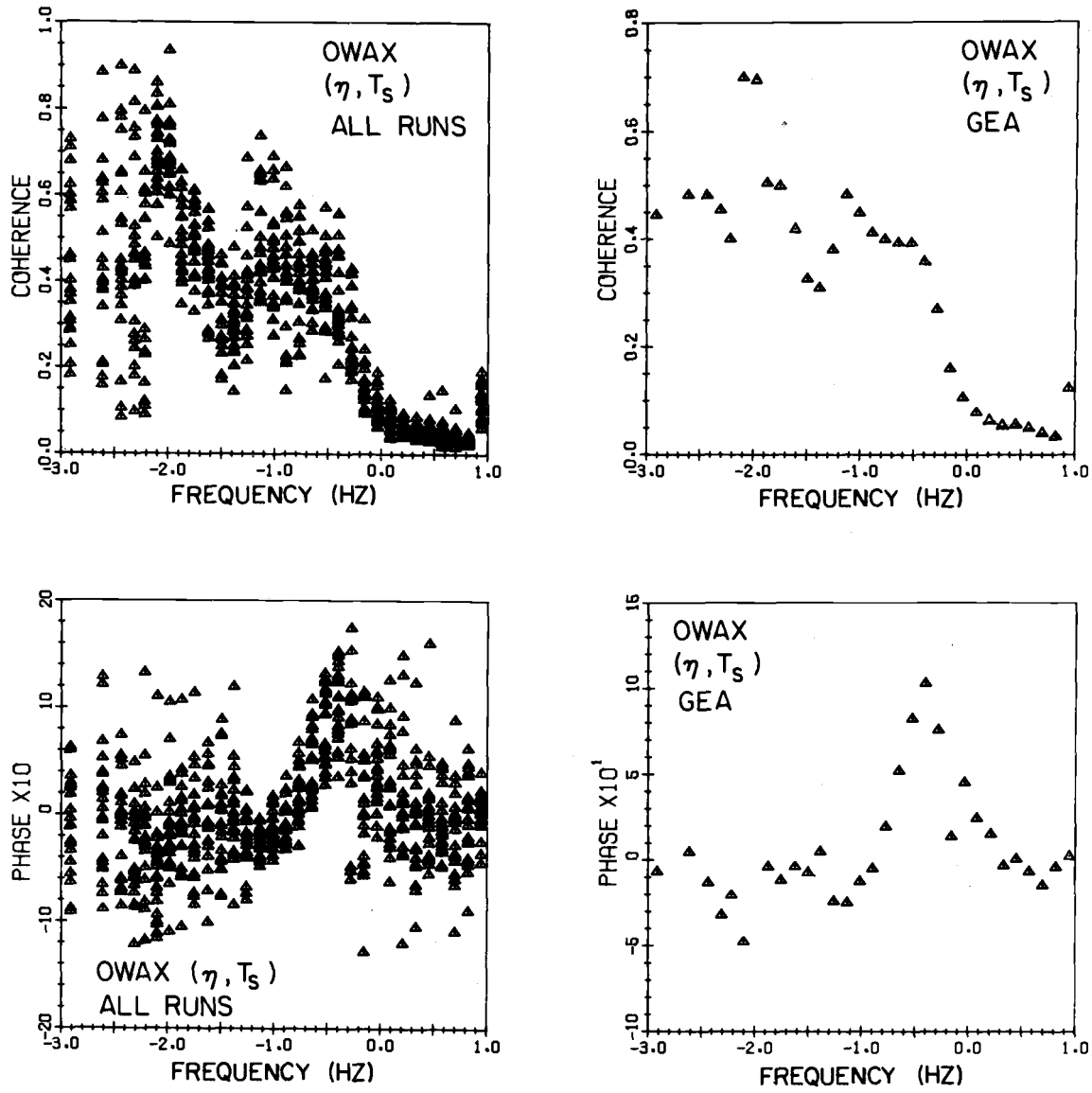

Figure 5.14 Coherence and phase spectral for all the OWAX runs. The peak in the wave spectrum occurs at about 0.1 Hz. Ground ensembly averaged coherence and phase spectra are also shown.

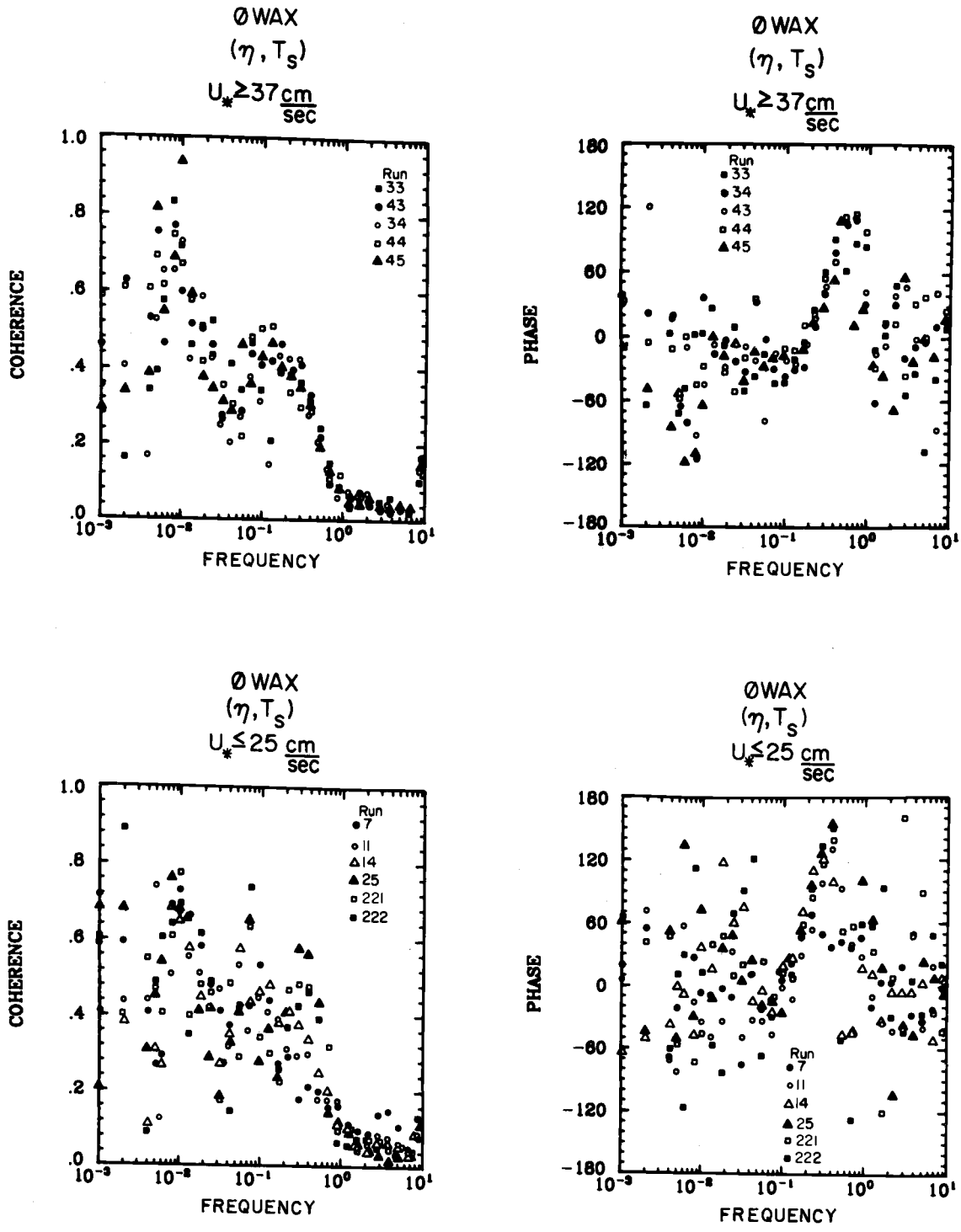

Figure 5.15 Phase and coherence spectra grouped according to the magnitues of U_*.

(η_{RMS}) yields results quite similar to those based upon classification by U_* This result is not surprising as the wave height is closely related to the wind stress. No significant reduction in variability is seen in either phase or coherence estimators when the runs are classified according to the total heat flux Q. Runs grouped according to temperature scale (Q/U_*) are shown in Figure 5.16. Significantly less variability is evident in both coherence and phase estimators for the case of Q/U_* ($\leq .48$ mjoules/cm^3) compared to those runs with high Q/U_*. These results indicate that processes associated with the production of sea surface temperature fluctuations are more strongly influenced by wind stress than heat flux.

Sea Surface Temperature Fluctuations and Heat Transfer

Saunders (1967) suggests that the temperature deviation ΔT between the cooler surface layer at the interface and the warmer oceanic bulk temperature can be related to the upward heat flux Q and the wind stress at 10 meters through a constant of proportionality λ [Equation (2)]. Mean values of the sea surface temperature, upward heat flux Q and wind stress τ and ΔT for all the OWAX runs are shown in Table 5.1. Temperature deviation was estimated from the surface temperature signal as indicated above. For the conditions shown, $\lambda = 6 \pm 2$ in agreement with the range suggested by Saunders ($5 \leq \lambda \leq 10$). Oceanic observations by Hasse (1971) over the range of wind speeds 1.45 to 11.35 m/sec yield a mean value of $\lambda = 8$ while those by Paulson and Leavitt (1972) during BOMEX yield an average value of $\lambda = 7$. Both sets of observations are in good agreement with the results presently reported.

In Figure 5.17 the temperature deviation ΔT is plotted as a function of $Q\nu/k(\tau/\rho_w)^{1/2}$ where Q is the upward heat flux, ν is the kinematic viscosity and k the thermal conductivity of water (both at 15° C), τ is the wind stress at 10 meters and ρ_w is the density of

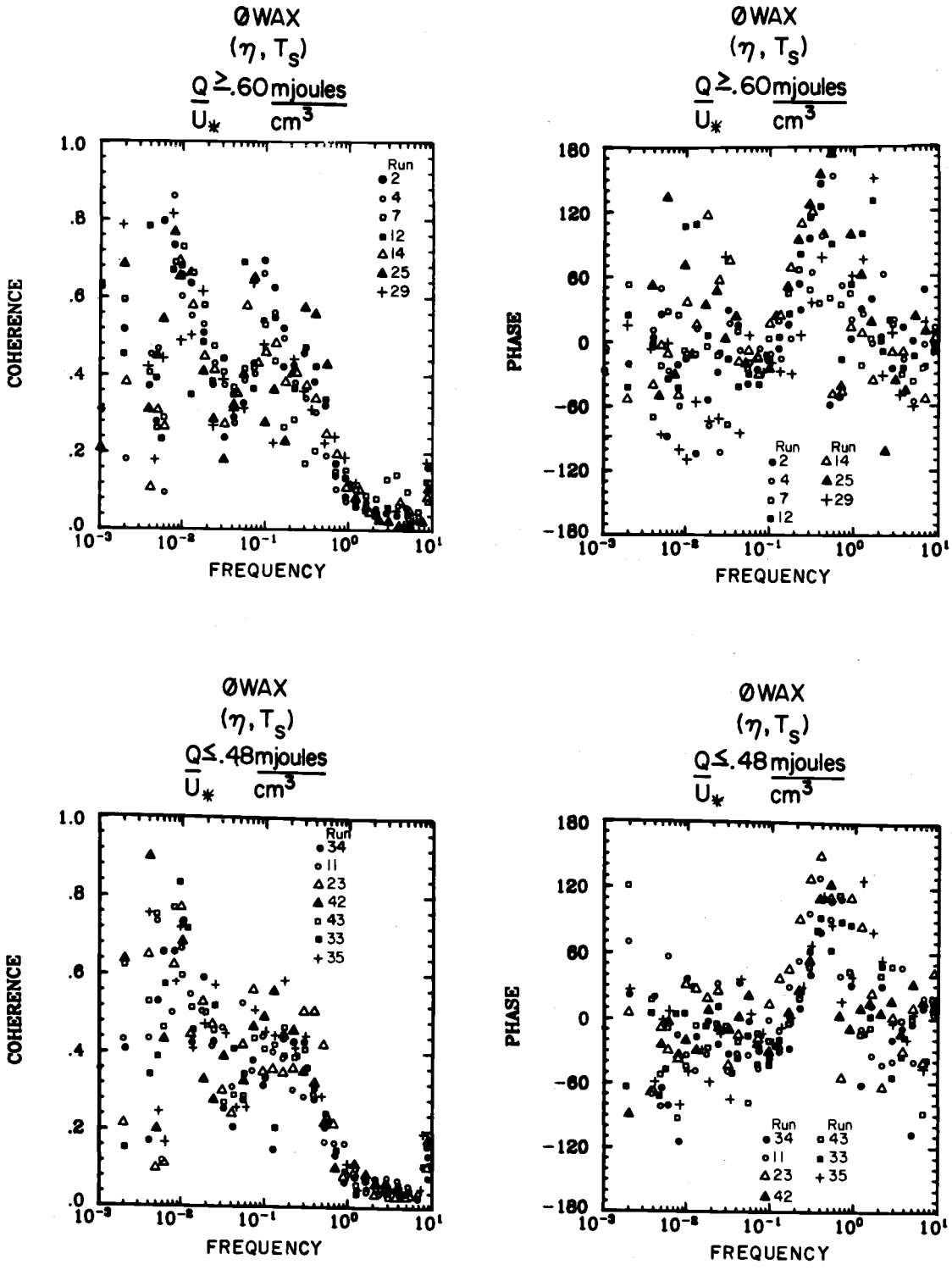

Figure 5.16 Phase and coherence spectra grouped according to the magnitude of Q/U_*.

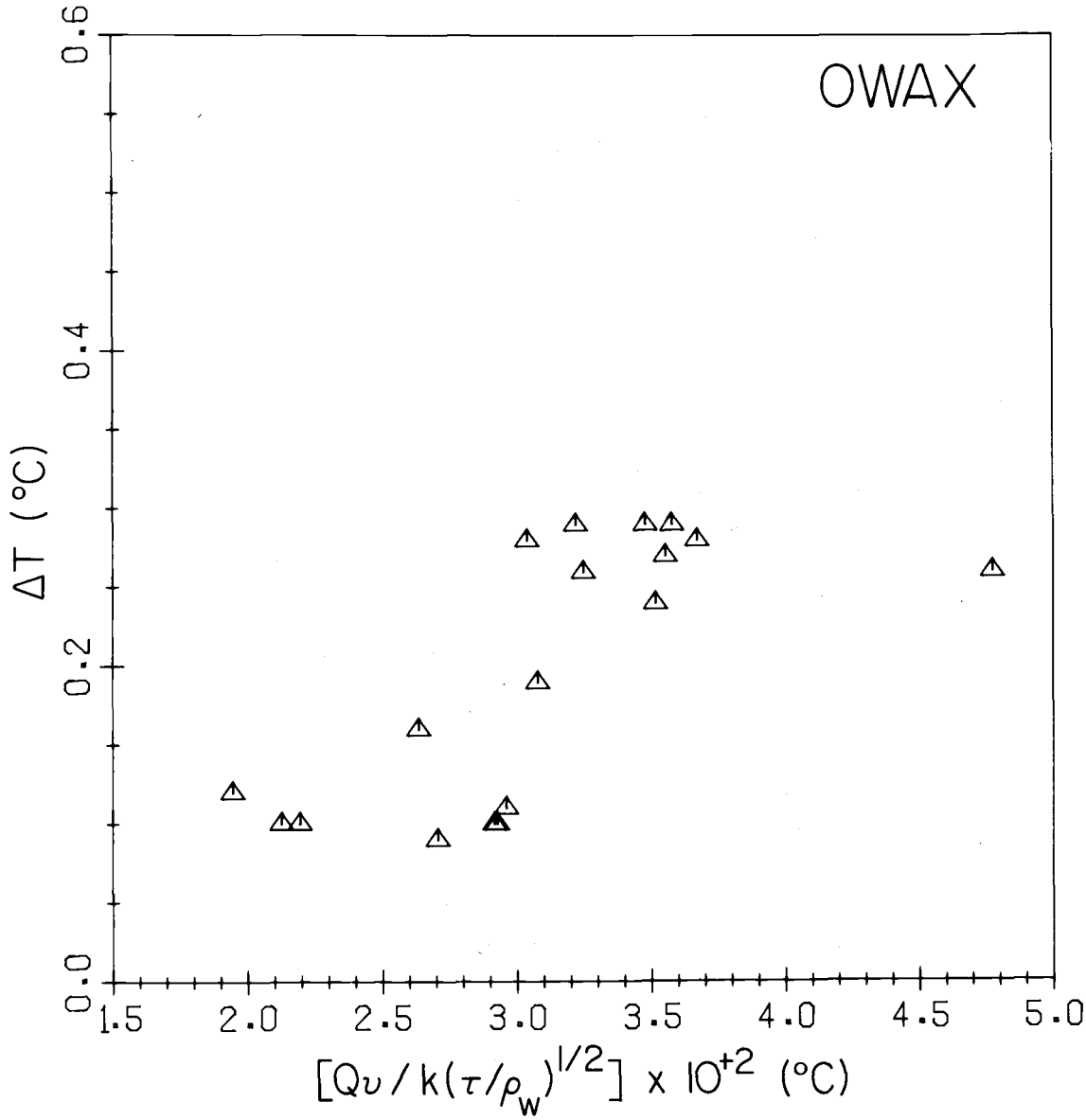

Figure 5. 17 The temperature difference ΔT between the cool surface layer and the warmer bulk temperature below is shown as a function of $Q\nu/k(\tau\rho_w)^{1/2}$. The slope of the best fit line is the dimensionless constant in Saunders' formula.

water. The slope of the line through these points is the dimensionless constant λ in Saunders' relation (Equation 2). The six points with the lowest ΔT show a value of λ in the range $3 \leq \lambda \leq 5$. The mean of these points is $\lambda = 4$. From Table 5. 1, it can be seen that these runs were all made under conditions of high waves and high U_*. An average rms wave height for this set of runs is . 77 meters. Laboratory measurements (Hill, 1970) show that the temperature deviation ΔT decreases by about a factor of 3 under fetch and wind speed conditions suitable for the generation of waves. Hill represented his measurements by an expression of the form

$$\Delta T = Q/\gamma c_p \rho_w^{1/2} \tau^{1/2} \tag{4}$$

where the dimensionless exchange coefficient γ varies between 1/60 in the absence of waves and 1/20 in the presence of waves. This variation in exchange coefficient corresponds to values of $\lambda = 11$ in the absence of waves and $\lambda = 4$ with waves present. Similar laboratory measurements by McAlister and McLeish (1969) yield a value of $\lambda = 4.5$ (see Paulson and Parker, 1972) in the presence of waves. Thus both field observations and laboratory experiments support the theoretical analysis of Witting (1971). He suggests that capillary waves can decrease the temperature deviation across the thermal molecular boundary layer by factors as large as 9 if the average heat flux at the interface is independent of the presence of waves. His analysis further suggests that deep water gravity waves reduce the mean temperature deviation by factors no larger than 1. 38.

Laboratory measurements by Paulson and Parker (1972) under conditions of negligible wave generation indicate $\lambda = 15$. This value is somewhat higher than the value $\lambda = 11$ obtained by Hill (1971) from laboratory experiments in the absence of waves.

Saunders' (1971) relation fails to yield a unique value of λ for

the various conditions reported. This failure may be explained by effects associated with the presence of waves. Wave generation processes may reduce the stress in the viscous sublayer substantially below the stress measured at the 10 meter level (Dobson, 1971). Thus larger values of λ might be expected in the presence of waves. However, steep capillary waves would tend to decrease ΔT (Witting, 1971) and hence λ. Both laboratory experiments (Hill, 1971) and the field observations reported here suggest that mechanism tending to decrease λ dominate. The OWAX measurements do not support the conclusion of Paulson and Parker (1972) that the effects of capillary may be more pronounced in laboratory experiments than field observations.

Summary

Observations were made of sea surface temperature with a Barnes PRT-5 radiation thermometer from Research Platfrom FLIP. During OWAX the instrument viewed a 25 cm diameter disc and responded in frequencies up to 3 Hz. During POLE, a component of the North Pacific Experiment (NORPAX) the instrument viewed a 60 cm diameter disc. The records suggest that sea surface temperature fluctuations are asymetric with spikes of warm temperature, frequently as large as 0.5° C. These spikes typically persist for periods of 1 to 2 seconds. Destruction of the thermal boundary layer just below the interface by capillary waves, breaking waves, gusts of wind and turbulence in the water are possible mechanisms causing the warm spikes. The temperature structure is examined in relation to simultaneous measurements of wave height, upward heat flux Q (where Q is the sum of latent, sensible and radiative heat flux at the interface) and wind stress.

The peak in the spectrum is 1 Hz as compared to the .1 Hz peak in the gravity wave spectrum. A statistically significant

coherence, typically $0.4 \leq \gamma \leq 0.5$, between the wave and sea surface temperature records occurs at the same frequency as the peak in the wave spectrum. For some runs with a root-mean-square wave height greater than 1 meter the coherence at this frequency is as large as 0.8. Phase spectra calculated from these records indicate that both capillary wave action on the upwind crests of gravity waves and steeply-sloping wave crests on the downwind side are related to the intermittent destruction of the thermal boundary layer and subsequent production of warm temperature spikes.

The magnitude of the temperature deviation between the cool surface layer at the interface and the warmer bulk temperature is examined in relation to simultaneous measurements of heat flux through the interface and wind stress on the surface as predicted by Saunders (1967). The dimensionless constant in Saunders' relation equals 6 on average.

VI. SUMMARY

This thesis examines the small scale temperature structure of the upper ocean in the context of the measurement and analysis of the heat balance at the sea surface, the radiometrically determined sea surface temperature, the distribution of downward irradiance with depth, and the atmospheric temperature field near the air-sea interface. Each chapter is a self-contained analysis of a particular phenomenon associated with upper ocean thermal structure and includes a summary section where final conclusions are presented. The present chapter provides a synthesis of all the results related to upper ocean structure.

Mid-oceanic (35° N, 155° W) observations of the various components of the radiative flux were made from R/P FLIP. The sea surface albedo was estimated from simultaneous measurements of the incident and reflected solar fluxes. Parametric representation of albedo in terms of solar altitude and atmospheric transmittance appears valid for solar altitudes greater than 25 degrees. For overcast conditions the sky radiance distribution becomes nearly isotropic and the albedo assumes the value 0.06. For clear skies the albedo exhibits a strong functional dependence on solar altitude at low sun angle. Good agreement exists between the values presently reported and those obtained by R. E. Payne (1972) from observations over coastal waters, except for conditions of low sun angle. For these conditions the values obtained in the North Pacific are systematically lower than the corresponding coastal values. The variation of albedo with sea surface roughness is also investigated.

Most of the previously reported daytime measurements of the net long-wave flux were obtained indirectly by subtracting simultaneous measurements of the net radiation and the net solar flux. The accuracy of such estimates can be low during the day because the net

long-wave flux is frequently an order of magnitude less than the actually measured and differenced quantities. The net long-wave fluxes reported in this thesis represent direct flux measurements. Nocturnal intercomparison of the net long-wave and the net all-wave radiometers yield values which agree on average to within 2%, well within the stated accuracies of either device.

Empirical relations for estimating both the short-wave and long-wave components of the radiative flux are evaluated in the context of the present measurements. A relation due to Lumb (1964) for determining the incident solar flux based on standard meteorological observations consistently yields values in good agreement (5%) with observations. The formulas available for estimating the net long-wave flux yield poor agreement with observations. The most significant conclusion of Chapter II is the effect of such formulas on heat budget studies of the world's oceans. If the frequently used empirical relations consistently overestimate the net long-wave flux by factors in excess of 50%, as the results of this study suggest, northward heat transports based on these formulas may be too small. This suggestion is in qualitative agreement with results of Vonder Haar and Oort (1973) which suggest on the basis of satellite measurements of radiation that the oceanic transport is larger than previous estimates based on empirical estimates of radiation.

Observations (Chapter III) were made of downward solar radiation as a function of depth during an experiment in the North Pacific (35° N, 155° W). Because of selective absorption of the short and long wavelengths, the irradiance decreases much faster than exponential in the upper few meters, falling to one-third of the incident value between two and three meters depth. Below 10 meters, the decrease was exponential at a rate characteristic of moderately clear water of Type IA. Neglecting one case having low sun altitude, the observations are well represented by the expression

$$I/I_o = R \exp[-z/\zeta_1] + (1-R) \exp[-z/\zeta_2]$$

where I is the irradiance at depth equals z, I_o is the irradiance at the surface less reflected solar radiation, R = 0.62, ζ_1 and ζ_2 are attenuation lengths equal to 1.5 and 20 m respectively, and z is the vertical space coordinate, positive downward with the origin at mean sea level. An improved knowledge of the distribution of solar radiation in the upper ocean is important for modeling physical, chemical and biological processes. The principal physical application is modeling the heating of the upper layers due to absorption of solar radiation.

Profiles of salinity and temperature (Chapter IV) in the upper 300 meters of the ocean were observed from R/P FLIP in January and February 1974 during the NORPAX POLE experiment (35° N 155° W). There was usually a well-mixed layer near the surface, although during light winds, a diurnal thermocline was evident. The structure below the thermocline was often complex with temperature inversions as large as 0.5° C. These inversions were compensated by salinity to stabilize the density profile. The depth of the well-mixed layer was correlated to mechanical energy input by the wind but was also influenced by horizontal advection of water having differing characteristics.

The one-dimensional mixed layer model of Kraus and Turner (1967) has been used to predict the depths of both the diurnal and seasonal mixed layers. In the few cases where comparisons with observations have been made, a single exponential of the form $S(z) = S_o \exp[-\beta z]$ has been used to parameterize the penetrative radiation where S is the downward irradiance and S_o is the surface value. The attenuation coefficient, β, has been assumed constant with depth. The data (Chapter III) suggest a more appropriate parameterization for the absorption of solar flux in the upper ocean is the double exponential of the form (equation 3.4). With this parameterization of the

absorption of solar flux the complete set of vertically integrated equations defining the behavior of the upper mixed layer, under the assumptions of Kraus and Turner (1967) deepening were presented (Chapter IV). These equations were employed in diagnostic form to predict the behavior of the well-mixed layer observed during POLE. For conditions of low wind speed ($u \leq 4$ m/sec) and net heat gain at the surface predicted values of mixed layer depth and sea surface temperature agree well with observations. During periods of higher wind speed the effectiveness of the turbulent exchange of heat and mass across the air-sea interface was greatly enhanced and the net heat gain at the surface significantly reduced. For these periods, the approach to equilibrium probably did not occur and the results of the diagnostic model proved unsatisfactory.

The theory of the seasonal thermocline advanced by Kraus and Turner (1967) assumes that the turbulent energy available for mixing is some constant fraction in the rate of downward transfer of energy from the local wind. Estimates of m, based upon the observed winds and the rate of change of the potential energy of the well-mixed layer, during POLE were made. For the deepening event occurring mid-way through the experiment a mean value of $m = 0.0027$ was obtained. This estimate of m is approximately double that of Denman (1973b), three-quarters that suggested by Halpern (1975) and about one-fourth the value obtained by Turner (1964). A second mixing event 370 hours into the POLE observational period yields a value of $m = 0.0017$ in better agreement with the value $m = 0.0012$ observed by Denman.

The large degree of scatter between the various estimates suggests that additional observations are required to accurately determine the characteristics of the m parameter. It is likely the mixing energy flux coefficient is not a constant but rather a function of local oceanic conditions. Irradiance measurements made simultaneous to

a mixing event would enable elimination of one degree of freedom from the governing equations (i. e. the α's and β's would be specified by observations, Chapters III, IV). Thus the equations of Chapter IV could be used to hindcast the best value of m based upon observed model inputs and the agreement between predicted and observed values of mixed layer depth and sea surface temperature. This approach eliminates the specification of arbitrary references levels and temperatures in the calculation of the change in potential energy of the water column upon which the values of m reported in the literature are based.

In Chapter V observations of sea surface temperature made with a Barnes PRT-5 radiation thermometer are presented. The records suggest that sea surface temperature fluctuations are asymetric with spikes of warm temperature, frequently as large as 0. 5° C. These spikes typically persist for periods of 1 to 2 seconds. Destruction of the thermal boundary layer just below the interface by capillary waves, breaking waves, gusts of wind and turbulence in the water are possible production mechanisms for the warm spikes. The temperature structure is examined in relation to simultaneous measurements of wave height, upward heat flux Q (where Q is the sum of latent, sensible and radiative heat flux at the interface) and wind stress.

The peak in the spectrum is 1 Hz as compared to the 0. 1 Hz peak in the gravity wave spectrum. A statistically significant coherence, typically 0. 4 and 0. 5, between the wave and sea surface temperature records occurs a the same frequency as the peak in the wave spectrum. For some runs with a root-mean-square wave height greater than 1 meter the coherence at this frequency is as large as 0. 8. Phase spectra calculated from these records indicate that both capillary wave action on the upwind crests of gravity waves and steeply-sloping wave crests on the downwind side are related to the intermittent destruction of the thermal boundary layer and subsequent

production of warm temperature spikes.

The magnitude of the temperature deviation between the cool surface layer at the interface and the warmer bulk temperature is examined in relation to simultaneous measurements of heat flux through the interface and wind stress on the surface as predicted by Saunders (1967). The dimensionless constant in Saunders' relation is equal to 6 on average.

BIBLIOGRAPHY

Alexander, R. C. and J-W. Kim, 1976: Diagnostic model study of mixed-layer depths in the summer North Pacific. J. Phys. Oceanogr., 6, 293-298.

Amos, D. E. and L. H. Koopmans, 1963: Tables of the distribution of the coefficient of coherence for stationary bivariate Gaussian processes. Sandia Corporation monograph SCR-483.

Anderson, E. R., 1952: Energy budget studies, Water Loss Investigations: Lake Hefner Studies, U. S. Geol. Surv. Circ., 229, 71-88.

Ashburn, E. V., 1963: The radiative heat budget at the ocean-atmosphere interface, Deep Sea Research, 10, 507-606.

Barnett, T. P., 1976: Large scale variation of the temperature field in the North Pacific Ocean. Naval Research Reviews, March 1976.

Batchelor, G. K., 1967: Introduction to Fluid Dynamics. Cambridge University Press, pp. 70, 147.

Bendat, J. S. and A. G. Piersol, 1971: Random Data: Analysis and Measurement Procedures. Wiley-Interscience, New York.

Brunt, D., 1940: Radiation in the atmosphere, Quart. J. Roy. Meteorol. Soc., 66, Suppl., 34-40.

Budyko, M. L., 1958: The heat balance of the earth's surface. Gidrometeorol., 1956 (Translated from Russian by N. A. Stepanova, U. S. Weather Bur., Washington, D. C.

Budyko, M. I., 1963: Atlas of Heat Balance, 2nd ed. Moscow. Akad. Naule. U. S. S. R. (1st ed., 1956) Leningrad, Main Geophys. Obs.

Burt, W. V., 1954: Albedo over wind-roughened water. J. Meteor., 11, 283-290.

Charnell, R. L., 1967: Long-wave radiation near the Hawaiian Islands, J. Geophys. Res., 72, 489-495.

Cox, C. and W. Munk, 1955: Some Problems in Optical Oceanography, J. Mar. Res., 14, 63-78.

Cox, C. S. and W. Munk, 1954: Statistics of sea surface derived from Sun glitter. J. Marine Res., 13, 198-227.

Davis, R. E. and L. Regier, 1974: Current meter profiling during POLE. Norpax Highlights. Volume 2, Number 5, 4-7.

Denman, K. L. 1973: A time-dependent model of the upper ocean. J. Phys. Oceanogr., 3, 173-184.

Denman, K. L. and M. Miyake, 1973: Upper layer modification at Ocean Station Papa: Observations and Simulation. J. Phys. Oceanogr., 3, 185-196.

deSzoeke, R. A. and P. B. Rhines, 1976: Asymptotic regimes in mixed-layer deepening. J. Mar. Res., 34, 111-116.

Dobson, F. W., 1971: Pressure measurements on wind-generated sea waves. J. Fluid Mech., 48, 91-127.

Enochson, L. D. and N. R. Goodman, 1965: Gaussian approximation to the distribution of sample coherence, AFFDL TR 65-57 Air Force Flight Dynamics Laboratory, Wright-Patterson AFB, Ohio, February.

Ewing, G., 1950: Slicks, surface films and internal waves. J. Marine Res., 9, 161-187.

Ewing, G. C. and E. D. McAlister, 1960: On the thermal boundary layer of the ocean. Science, 131, 1374-1376.

Fedorov, K. N., 1969: On the vertical stability of temperature inversions in the ocean. Okeanologiya, 9, 82-86.

Federov, K. N., 1970: On the step-like structure of temperature inversions in the ocean. Izv. Atmos. Oceanic Phys., 6, 1178-1188.

Fedorov, K. N., 1971: Origin of thin temperature inversions under the homogeneous surface layer of the ocean Okeanologiya, 11, 12-16.

Franceschini, G. A., 1975: Influence of clouds on solar radiation and its spectral composition (abstract), Bull. Amer. Meteorol. Soc., 54(10), 1122-1123.

Frederick, M. A., 1970: An atlas of Secchi disc transparency and Forel-Ule color codes for the oceans of the world. Report, Naval Postgraduate School, Monterey, CA, 177 pp.

Friehe, C. A. and K. Schmitt, 1974: Estimates of surface fluxes during POLE. NORPAX Highlights, Vol. 2, No. 5, 8-9.

Fritschen, L. J., 1965: Miniature net radiometer improvements, J. Appl. Meteorol., 4, 528-532.

Geisler, J. E. and E. B. Kraus, 1969: The well-mixed Ekman boundary layer. Deep-Sea Res., 16, Suppl. 73-84.

Goodrich, F. C., 1962: On the damping of water waves by monomolecular films. J. Phys. Chem., 66, 101-104.

Grant, H. L., A. Moilliet and V. M. Voget, 1968: Some observations of the occurrence of turbulence in and above the thermocline. J. Fluid Mech., 34, 443-448.

Gregg, H. C., 1976: Finestructure and microstructure Observations During the Passage of a Mild Storm, J. Phys. Oceanogr., 6, 528-555.

Halpern, D., 1974: Observations of the deepening of the wind-mixed layer in the Northeast Pacific Ocean. J. Phys. Oceanogr., 4, 454-466.

Hasse, L., 1963: On the coding of the sea surface by evaporation and heat exchange. Tellus XV, 4, 363-366.

Hasse, L., 1971: The sea surface temperature and deviation and the heat flow at the air-sea interface. Boundary Layer Meteoro Meteorol. 1, 368-379.

Hill, R. H., 1972: Laboratory measurements of heat transfer and thermal structure near an air-water interface. J. Phys. Oceanogr., 2, 190-198.

Hishida, K. and K. Hishiyama, 1969: On the variation of heat exchange and evaporation at the sea surface in the western North Pacific Ocean, J. Oceanogr. Soc. Jap. 25(1), 1-9.

Howe, M. R. and R. I. Tait, 1970: Further observations of thermohaline stratification in the deep ocean, Deep-Sea Res., 17, 963-977.

Howe, M. R. and R. I. Tait, 1972: The role of temperature inversions in the mixing processes of the deep ocean. Deep-Sea Res. 19, 781-791.

Jassby, A. and T. Powell, 1975: Vertical patterns of eddy diffusion during stratification in Castle Lake, California. Limn. and Oceanog., 20, 530-543.

Jenkin, G. M. and D. G. Watts, 1968: Spectral Analysis and Its Applications. Holden-Day, San Francisco.

Jerlov, N. G., 1968: Optical Oceanography, Elsevier, Amsterdam, 194 pp.

Julian, P. R., 1974: Comments on the determination of significance levels of the coherence statistics. J. Atmos. Sci., 32, 836-837.

Kato, H. and O. M. Phillips, 1969: On the penetration of a turbulent layer into a stratified fluid. J. Fluid Mech., 37, 643-655.

Kimball, H. H., and L. F. Hand, 1921: Sky-brightness and day-light illumination measurements, Mon. Wea. Rev., 49, 481-488.

Kimball, H. H., 1928: Amount of solar radiation that reaches the surface of the earth on the land and on the sea, and methods by which it is measured, Mon. Wea. Rev., 56, 393-398.

Kitaygorodskiy, S. A., 1961: On the possibility of theoretical calculation of vertical temperature profile in the upper ocean of the sea. Izv. Akad. Nauk. SSSR, Ser. Geofz., No. 1-6, 313-318.

Kondratyev, K. Ya., 1969: Radiation in the Atmosphere, New York, Academic Press, 912 pp.

Kraus, E. B., 1972: Atmosphere-Ocean Interaction. Oxford University Press, London, 275 pp.

Kraus, E. B. and J. S. Turner, 1967: A one-dimensional model of the seasonal thermoclines: II, the general theory and its consequences. Tellus, 19, 98-106.

Laevastu, T., 1960: Factors affecting the temperature of the surface layer of the sea, Commentat Phys. Math., 25, 1-36.

Laevastu, T., 1967: Cloud factor in long-wave radiation formulas, J. Geophys. Res., 72, 4277.

Lumb, F. E., 1964: The influence of clouds on hourly amounts of total solar radiation at the sea surface. Quart. J. Roy. Meteorolo. Soc., 40, 43-56.

McAlister, E. D., 1964: Infrared optical techniques applied to oceanography, 1, measurements of total heat flow from the ocean surface. Appl. Optics, 3(5), 609-612.

McAlister, E. D. and McLeish, 1969: Heat transfer in the top millimeter of the ocean. Geophys. Res., 74, 3408-3414.

Monahan, E. C., 1971: Oceanic whitecaps, J. Phys. Oceanogr., 1, 139-144.

Monin, A. S., 1972: Specific features of the sea turbulence, Rapports et Proces-Verboux des Reunions, 162, Conseil Internationa, pour l'Exploration de laMer, Charlottenlund Slot, Denmark, 7-11.

Niiler, P. P., 1975: Deepening of the wind-mixed layer. J. Mar. Res., 33, No. 3, 405-427.

Osborne, M. F. M., 1964: The interpretation of infrared radiation from the sea in terms of its boundary layer. Deut. Hydrogr. Z., 17, 115-136.

Osborne, M. F. M., 1968: The theory of the measurement of surface viscosity. Kolloid Z. Palym., 224, 150-161.

Paltridge, G. W., 1969: A net long-wave radiometer, Quart. J. Roy. Meteorol. Soc., 95, 635-638.

Paulson, C. A. and T. W. Parker, 1972: Cooling of a water surface by evaporation, radiation and heat transfer, J. Geophys. Res., 77, 491-495.

Paulson, C. A. and E. D. Leavitt, 1972: Sea surface temperature microstructure. Trans. Amer. Geophys. Union, 53, 1021.

Paulson, C. A. and J. J Simpson, 1977: Irradiance Measurements in the Upper Ocean, Submitted to J. Phys. Oceanogr.

Payne, R. E., 1971: Albedo of the sea surface. Ph. D. dissertation, University of Rhode Island.

Payne, R. E., 1972: Albedo of the sea surface. J. Atmos. Sci., 29, 959-970.

Phillips, O. M., 1966: The Dynamics of the Upper Ocean. Cambridge University Press, p. 144.

Pollard, R. T., P. B. Rhines and R. O. R. Y. Thompson, 1973: The deepening of the wind-mixed layer. Geophysical Fluid Dyn., 3, 381-404.

Reed, R. K. and D. Halpern, 1972: Insolation and Net Long-Wave Radiation off the Oregon Coast, J. Geophys. Res., 80, 839-844.

Roden, G. L., 1974: Thermohaline structure, fronts and sea-air energy exchange of the trade wind region east of Hawaii, J. Phys. Oceanogr. 4(2), 168-182, 1974.

Roll, H. U., 1965: Physics of the Marine Atmosphere. New York, Academic Press, 1961-1963.

Saunders, P. M., 1967: Shadowing on the ocean and the existence of the horizon, J. Geophys. Res., 72, 4643-4649.

Schooley, A. H., 1958a: Probability distributions of water-wave slopes under conditions of short fetch. Trans. Am. Geophys. Union, 39, 405-408.

Schooley, A. H., 1958b: Profiles of wind-created water waves in the capillary-gravity transition region. Trans. Am. Geophys. Union, 39, 531.

Schooley, A. H., 1969: Radiation Measurements at Sea, J. Geophys. Res., 74, 958-

Seckel, G. R. and F. H. Beaudry, 1973: The radiation from sun and sky over the North Pacific Ocean (abstract) Eos. Trans. AGU, 54, 1114.

Sellers, W. D., 1965: Physical Climatology, University of Chicago Press, 272 pp.

Simpson, J. J., 1976. The Response of the Upper Ocean to Meteorological Forcing During the NORPAX POLE Experiment, Book of Abstracts, 2nd Joint Oceanographic Assembly, Edinburgh, Scotland, p. 186.

Simpson, J. J. and C. A. Paulson, 1974: Small scale sea surface and near sea surface temperature structure. EOS, 56, 1133.

Simpson, J. J., 1976: The temperature and salinity structure of the upper ocean during the NORPAX POLE experiment, Bull. Am. Meteor. Soc., 57, p. 153.

Simpson, J. J. and C. A. Paulson, 1977a: Mid-Ocean Observations of Atmospheric Radiation. To be submitted.

Simpson, J. J. and C. A. Paulson, 1977b: Upper Ocean Structure: Temporal Variations in the Central North Pacific. To be submitted.

Simpson, J. J. and C. A. Paulson, 1977c: Small Scale Sea Surface Temperature Structure. To be submitted.

Smith, R. C., J. E. Tuler and C. R. Goldman, 1973: Optical properties and color of Lake Tahoe and Crater Lake. Limnol. and Oceanog., 18, 189-199.

Stommel, H. and K. N. Fedorov, 1967: Small scale structure in temperature and salinity near Timor and Mindanao. Tellus XIX, 306-324.

Stommel, H. and K. P. Koziol, 1976: Adjustment of Sea-Surface Temperature to Underlying Advective Fields - An Elementary Model, POLYMOOE NEws, No. 17, 27 October 1976.

Tabata, S., 1958: Heat Budget of the Water in the Vicinity of Triple Island, British Columbia, J. Fish. Res. Bd. Canada, 15(3), 429-451.

Tabata, S., 1964: Insolation in relation to cloud amount and sun's altitude, in Studies on Oceanography, edited by K. Yoshida. Univ. of Tokyo, Tokyo, 202-210.

Tabata, S., N. E. J. Boston and F. M. Boyce, 1965: The relationship between wind speed and summer isothermal surface layer of water at Ocean Station P in the eastern subarctic Pacific Ocean. J. Geophys. Res., 70, 3867-3878.

Tait, R. I. and M. R. Howe, 1971: Thermohaline staircases, Nature, Lond. 231 (5299), 178-179.

Thompson, R.O.R.Y., 1974: Predicting the characteristics of the well-mixed layer. WHIO - 74-82, unpublished manuscript.

Turner, J S., 1969: A note on wind mixing at the seasonal thermocline. Deep Sea Res., 16, 297-300.

Turner, J. S. and E. B. Kraus, 1967: A one-dimensional model of the seasonal thermocline, I. A laboratory experiment and its interpretation. Tellus XIX, 88-97.

Tyler, J. E., 1968: The Secchi disc. Limnol. and Oceanog., 23, 1-6.

Westlake, D. F., 1965: Some problems in the measurement of radiation under water: A review Photochem. and Photobiol., 4, 849-868.

Witting, J., 1971: Effects of plane progressive irrotational waves on thermal boundary layers. J. Fluid Mech., 50, part 2, 321-334.

Wu, Jin, 1971: An estimation of oceanic thermal-sublayer thickness. J. Phys. Oceanogr., 284-286.

Wyrtki, K., 1965: The average annual heat balance of the North Pacific Ocean and its relation to ocean circulation. J. Geophys. Res., 70, 4547-4559.